JAGIELLONIAN UNIVERSITY

FACULTY OF PHYSICS, ASTRONOMY AND APPLIED COMPUTER SCIENCE
MARIAN SMOLUCHOWSKI INSTITUTE OF PHYSICS

Doctoral dissertation

Novel method to search for axion-like particles in storage rings

Swathi Karanth
Belthangady, India

Supervisor:
prof. dr hab. Andrzej Magiera

Auxiliary supervisor:
dr Aleksandra Wrońska

Cracow 2023

Wydział Fizyki, Astronomii i Informatyki Stosowanej
Uniwersytet Jagielloński

Oświadczenie

Ja, niżej podpisana Swathi Karanth (nr indeksu 1142643), doktorantka Wydziału Fizyki, Astronomii i Informatyki Stosowanej Uniwersytetu Jagiellońskiego oświadczam, że przedłożona przeze mnie rozprawa doktorska pt. „Novel method to search for axion-like particles in storage rings„ jest oryginalna i przedstawia wyniki badań wykonanych przeze mnie osobiście, pod kierunkiem prof. dr hab. Andrzeja Magiery i dr Aleksandry Wrońskiej. Pracę napisałam samodzielnie.

Oświadczam, że moja rozprawa doktorska została opracowana zgodnie z Ustawą o prawie autorskim i prawach pokrewnych z dnia 4 lutego 1994 r. (Dziennik Ustaw 1994 nr 24 poz. 83 wraz z późniejszymi zmianami).

Jestem świadoma, że niezgodność niniejszego oświadczenia z prawdą ujawniona w dowolnym czasie, niezależnie od skutków prawnych wynikających z ww. ustawy, może spowodować unieważnienie stopnia nabytego na podstawie tej rozprawy.

Krakow, 15 czerwca 2023 ....

podpis doktorantki

Abstract

Axions or axion-like particles (ALPs) are intriguing hypothetical entities with the potential to solve long-standing mysteries in physics, including the strong CP problem and the nature of dark matter. This work presents a project demonstrating a novel method to search for axion/(ALPs) using a storage ring by exploiting the notion that the local ALP-saturated dark matter field couples to the spin of the nucleons, via either oscillating electric dipole moment, or via the axion-wind effect.

The proof-of-principle experiment was conducted at the Cooler Synchrotron COSY in Jülich, Germany, using an in-plane polarised deuteron beam with momenta near $970\,\mathrm{MeV}/c$. At resonance between the spin-precession frequency, which is related to the momentum of the beam, and the ALP frequency related to its mass, the polarisation was expected to accumulate in the direction perpendicular to the ring plane. Since the axion frequency is unknown, the experiment involved scanning the frequency space for the aforementioned resonance. The scanning process entailed ramping of the beam momentum and, consequently, the spin precession frequency and searching for the change in vertical polarisation that is anticipated as the signal for resonance crossing. To account for the unknown phase between the polarisation precession and the ALP field, four beam bunches with mutually orthogonal polarisation directions were employed. A frequency scan of 1.5–kHz width centred around the spin precession frequency of 121 kHz was performed, accompanied by a methodology test using a radio frequency Wien filter.

Although no resonant signals from ALPs were observed within the experimental sensitivity, the first upper limit on the oscillating electric dipole moment of deuterons $\left|d^d_{\mathrm{AC}}\right| < 6.4\times10^{-23}\,e\,\mathrm{cm}$ is provided at a 90% confidence level. Additionally, the upper limit on the coupling constants of ALPs with deuteron in the mass range of $4.95\,\mathrm{neV}\,c^{-2}$ - $5.02\,\mathrm{neV}\,c^{-2}$ are also derived.

Streszczenie

Aksjony lub cząstki aksjonopodobne (ang. axion-like particles, ALPs) są intrygującymi hipotetycznymi bytami stanowiącymi potencjalne rozwiązanie pewych problemów w fizyce, m.in. zbyt słabego łamania symetrii CP (ang. strong CP problem) i natury ciemnej materii. Niniejsza praca przedstawia projekt demonstrujący nowatorską metodę poszukiwania aksjonów i ALPs przy użyciu pierścienia akumulacyjnego, przy założeniu, że lokalne pole ciemnej materii, pochodzące głównie od ALPs, oddziałuje ze spinem nukleonów poprzez indukowanie oscylującego elektrycznego momentu dipolowego lub efekt tzw. wiatru aksjonowego.

Pierwszy eksperyment demonstrujący metodę został przeprowadzony przy użyciu synchrotronu Cooler Synchrotron COSY w Jülich w Niemczech przy wykorzystaniu wiązki deuteronów spolaryzowanej w płaszczyźnie pierścienia, o pędach bliskich $970\,\mathrm{MeV}/c$. Oczekiwano, że przy rezonansie między częstotliwością precesji spinowej, która jest związana z pędem wiązki, a częstotliwością ALPs związaną z ich masą, polaryzacja wiązki będzie zyskiwać składową w kierunku prostopadłym do płaszczyzny pierścienia. Ponieważ częstotliwość aksjonów nie jest znana, eksperyment polegał na skanowaniu przestrzeni częstotliwości w poszukiwaniu wspomnianego rezonansu. Proces skanowania wiązał się ze zwiększaniem pędu wiązki, a w konsekwencji częstotliwości precesji spinu, i poszukiwaniem zmiany składowej pionowej wektora polaryzacji, która jest oczekiwana jako sygnał przejścia rezonansowego. Aby uwzględnić nieznaną fazę między precesją polaryzacji a polem ALPs, zastosowano cztery wiązki o wzajemnie ortogonalnych kierunkach polaryzacji. Przeprowadzono skanowanie częstotliwości w przedziale o szerokości 1,5 kHz wyśrodkowanym wokół częstotliwości precesji spinu wynoszącej 121 kHz, któremu towarzyszył test metodologiczny z użyciem filtru Wiena o częstotliwości radiowej.

Chociaż nie zaobserwowano sygnałów rezonansowych z ALPs w zakresie czułości eksperymentalnej, wyznaczono pierwsze górne ograniczenie na oscylujący elektryczny moment dipolowy deuteronów $\left|d^{d}_{\mathrm{AC}}\right| < 6.4\times10^{-23}\,e\,\mathrm{cm}$ na poziomie ufności 90%. Dodatkowo podano również górne ograniczenie na stałe sprzężenia ALPs z deuteronami w zakresie mas ALPs $4.95\,\mathrm{neV}\,c^{-2}$ - $5.02\,\mathrm{neV}\,c^{-2}$.

Acknowledgements

Undertaking this Ph.D. project has been a truly life-changing experience for me, and it would not have been possible without the support and guidance of many people. I am deeply grateful to all those who have contributed to this journey.

First and foremost, I would like to express my sincere gratitude to my supervisor, Prof. Dr. hab. Andrzej Magiera, for giving me the opportunity to pursue my Ph.D. and for his guidance throughout the research process, and for opening the door to work in the JEDI collaboration, which allowed me to meet and work with wonderful people. I am immensely thankful to Dr. Aleksandra Wrońska, my co-supervisor, and Dr. Edward Stephenson, my scientific mentor, for their unwavering support and guidance. Their knowledge and mentorship have been invaluable not only in terms of research, but also in navigating the challenges of academic and personal life. I am grateful for the depth of their patience and support over the past years. This PhD journey would have been significantly more challenging without them. I would like to express my sincere gratitude to the members of the JEDI collaboration, without whom this experiment would not have been possible. In particular, I would like to thank Dr. Volker Hejny for sharing his vast experience in all things “experiment”, for help in organising the beam time and for his continuous support throughout the analysis. I would also like to thank Prof. Dr. Jörg Pretz and Dr. Andreas Wirzba for generously sharing their time, knowledge, and expertise with me.

I must acknowledge the unwavering love, support, and encouragement of my parents. Their presence in my life has been a constant source of strength, and I am grateful for their belief in me. I want to thank all my friends for sharing a part of their lives with me and making this journey immensely memorable. To all the people who have been an integral part of my support system at a home away from home, Ola and Ed (once again to both of you), Sejal, Shivani, Arshiya, Divya and Akshay, and to Björn and Lennart for helping me through the final stretch, “Thank you”.

This Ph.D. work was supported by the DSC 2019 grant for young researchers and Ph.D. students of the WFAIS of the Jagiellonian University, the Polish Ministry of Science and Higher Education No: 2019-N17/MNS/000002 and the ERASMUS + TRAINEESHIP programme.

Contents

1 Introduction

Axions are fascinating particles that offer solutions to various mysteries in Nature, ranging from the strong CP–problem in quantum chromodynamics (QCD) to being potential candidates for dark matter (DM) in astrophysics [1].

Our current understanding of the visible Universe relies mainly on the Standard Model (SM) of particle physics, which was developed over the last few decades. Although SM successfully describes the fundamental building blocks of visible matter and the forces that govern their interactions with reasonable accuracy (which has been proved through numerous particle physics experiments), it falls short in explaining the existence of dark matter, which constitutes 85% of the matter in the Universe.

Despite our understanding of how DM affects the Universe on a macroscopic scale, we are yet to determine what DM is made up of. Here, the axions come into play, as hypothetical particles proposed to address the strong CP problem. Although CP symmetry is predicted to be violated in QCD, experimental evidence indicates a significantly smaller magnitude of CP-Violation (CPV) compared to the predicted values [1]. Peccei and Quinn introduced an extension to SM by proposing a global symmetry that aimed to solve the CP invariance in the strong interaction [2, 3]. Subsequently, Weinberg [4] and Wilczek [5] deduced the presence of a new particle, named axion, which acquires a small mass through spontaneous breaking of this symmetry. Axions or Axion-Like Particles (ALPs) - if sufficiently abundant - could also serve as candidates for DM, given their properties, see Refs [1, 6] for recent reviews.

Over the decades, numerous experiments have been proposed and conducted with the goal of searching axions as DM. This thesis focuses on one of these proposed methods, presenting the proof-of-principle experiment to find ALPs using a storage ring. The experiment capitalises on the properties of axions, such as the axion-induced oscillating Electric Dipole Moment (oscillating EDM) and the axion-wind effect, which introduce oscillations of the spin of particles circulating within the ring, with frequency related to the axion mass. The experiment was carried out at the Cooler Synchrotron (COSY) facility in Forschungszentrum Jülich, Germany, and utilised an in-plane (IP) polarised deuteron beam, whose spin undergoes precession in the presence of the magnetic field with a frequency related to the beam momentum. The resonance between the axion-induced oscillation frequency and the spin precession frequency would give manifest as the rotation of polarisation out of the horizontal plane to vertical direction, indicating the presence of axions. Given that the mass and, consequently, the associated frequency of axions is unknown, we search for axions by tuning the spin precession frequency in order to cross the resonance and observe a change in vertical polarisation as the signal [7].

In this thesis, I provide a comprehensive report on the first search for axions/ALPs using the storage ring method. The physics case for axions and ALPs, including an explanation of the strong CP problem and the dark matter problem, is presented in Chapter 2. Additionally, I discuss the interaction of axions and the various techniques used in the detection of axions.

In Chapter 3 , I provide the definitions of spin and polarisation, describe their interaction with the magnetic field in the ring, and examine the effects of axions on them. I also focus on the techniques used for polarisation measurement. Building upon the foundation laid in the previous chapter, I explain the change in polarisation at resonance and describe the expected signal in Chapter 4. Furthermore, I address the experimental challenges and prerequisites for observing the signal.

In Chapter 5, I provide an overview of the COSY research facility and explain the various devices used in this experiment. With the background, methodology, and requirements established, I detail the experimental procedure for the storage ring axion search in Chapter 6. This includes the frequency scan method to find the resonance and the use of radio frequency Wien filter (RF Wien filter) to generate a test signal.

In Chapter 7, I explain the simulations performed to optimise the experimental setup and recalculate the observed signals from both axion and WF scans to the axion couplings. In Chapter 8 I provide the details of the polarisation data analysis, including the determination of signal strength, and the mitigation of systematic effects using the Feldman-Cousins method (FC) method. Additionally, I compare the WF data to the simulations to benchmark the latter.

In Chapter 9, I present the results of this experiment, including the derived upper limits on the oscillating EDM and various coupling constants of axions. Finally, in Chapter 10, I conclude the thesis with a summary, discussion, and outlook for future research in this field.

2 Background and Motivation

In this chapter we briefly discuss the shortcomings of the Standard Model (SM) of particle physics that and the potential of axions and axion-like particles (ALPs) to address two of the most compelling theoretical issues in the field: the strong CP problem and dark matter (DM).

2.1 Physics case for axions and axion-like particles

The SM of particle physics, developed in stages over the latter part of 20^{th} century, has been successful in explaining most of the experiments in particle physics with high precision. While it explains three of the four fundamental forces, electromagnetic, strong and electro-weak interaction, it is inconsistent with general relativity, that explains the gravitational interactions. Additionally, SM does not provide satisfactory explanations for some fundamental physical phenomena, including:

- What is the origin of neutrino mass and hence neutrino oscillations?
- Why is there more matter than antimatter in the universe?
- Why is strong interaction CP invariant?
- What is the nature of DM, and what are the viable candidates for DM?
- What is the cause of the universe's accelerated expansion?

Axions and their ALP counterparts, if present, offer a potential resolution to two of the above pressing questions: the strong CP-problem, and under certain set of conditions, a good candidate for DM. Let us dive into these two items for the physics case for axion.

2.1.1 Strong CP problem

Before explaining the problem itself, an understanding of CPV is required. Charge conjugation C and Parity transformation P symmetries combined with Time reversal T symmetry make up the CPT symmetry, which is assumed to be invariant under all physical phenomena. The individual symmetries are explained below,

- C Charge conjugation – symmetry of physical laws when all particles are replaced with their antiparticle.
- P Parity transformation – the symmetry of the physical laws when the sign of the spatial coordinate is flipped.
- T Time reversal – a theoretical symmetry of physical laws when subjected to time reversal.

CPT symmetry is when a system remains indistinguishable when all three transformations are applied. For instance, if T symmetry is broken, then the combined CP transformation should also be broken, in other words, the system should be CP violating, to hold the CPT invariance. CPV is one of the three necessary conditions for the universe to yield matter-antimatter asymmetry [8].

SM of particle physics through QCD, which describes strong interaction, allows for a CP violating term in the Lagrangian [1].

$$\mathcal{L}_\theta = \theta_\mathrm{Q} \frac{g_s^2}{32\pi^2} G^a_{\mu\nu} \tilde{G}^{a\mu\nu} = \theta_\mathrm{Q} \frac{g_s^2}{32\pi^2} \vec{E}^a \cdot \vec{B}^a, \tag{2.1.1}$$

is the CP violating term in the QCD Lagrangian. Here, θ_Q is a constant parameter, g_s is the QCD coupling constant, G and $\tilde{G}$ are the gluonic field tensor and its dual, $\vec{E}^a$ and $\vec{B}^a$ are the colour electric and colour magnetic fields. Eq. (2.1.1) violates both T and P symmetries, and thus CP symmetry. To elucidate, under the respective transformation:

- $\vec{E}^a$ fields are T even, P odd and C odd. Thus even under CP.
- $\vec{B}^a$ fields are T odd, P even and C odd. Thus, odd under CP.
- Product of $\vec{E}^a$ and $\vec{B}^a$ fields are thus odd under CP. Consequently, the θ_Q term is CP violating.

The most sensitive probe of the CPV, that currently exists, is the neutron Electric Dipole Moment (EDM) d^n. The contribution of Eq. (2.1.1) to d^n, by relation to θ_Q, is given by

$$d^n \sim 10^{-16}\left|\theta_\mathrm{Q}\right| e\,\mathrm{cm}. \tag{2.1.2}$$

The current experimental upper bound on neutron EDM of $|d^n| \leqslant 1.8\times10^{-26}\,e\,\mathrm{cm}$ [9, 10] puts the limit on the theta parameter as $\left|\theta_\mathrm{Q}\right| \leqslant 10^{-10}$. There is no theoretical reason for the small value of θ_Q term in nature. The requirement of 'fine-tuning' our theory to accommodate the very small value of θ_Q is known as the strong CP-problem.

As a solution to this problem, Peccei and Quinn [2, 3] proposed to introduce a dynamic field, and PQ symmetry postulated by them would be spontaneously broken at a high-energy scale f_a . This led to Weinberg [4] and Wilczek [5] independently showing that such a dynamic field and the subsequent symmetry breaking would give rise to a light pseudoscalar particle: named the axion. The coupling between axion and gluons is given by

$$\mathcal{L} = \left(\frac{a}{f_a} - \theta_\mathrm{Q}\right)\frac{g_s^2}{32\pi^2}G^a_{\mu\nu}\tilde{G}^{a\mu\nu}, \tag{2.1.3}$$

where a is the axion field and f_a is the axion decay constant, also called the axion gluon coupling constant. At the minimum of the axion field potential ($a = \theta_\mathrm{Q} f_a$) the θ_Q term vanishes or, one could say, θ_Q is absorbed into the axion field and thus provides a 'non fine-tuned' explanation for the small neutron EDM. Because of their nonzero mass, axions are categorised as Pseudo-Nambu-Goldstone bosons.

In QCD, the axion has a single free parameter, the decay constant f_a from which the mass of the axion m_a can be determined using the relation $m_a \propto 1/f_a$, see [1]. Henceforth, these will be called QCD axions. Subsequently, a new class of pseudoscalar particles called ALPs were proposed. These do not have a predictive relation between their decay constant and mass; also, they do not solve the strong CP problem.

From here onwards,

- QCD axions refer to particles that solve the strong CP problem and have a linear relation between f_a and m_a;
- ALP refer to particles that do not solve strong CP problem and can be present anywhere in parameter space;
- Axions refer to either or both of the above.

2.1.2 Dark matter candidate

Axions are viable DM candidates. The existence of DM has many independent observational proofs. One of the earliest convincing evidence comes from the measurement of the galactic rotation curve [11, 12]; it showed that galaxies rotated at velocities faster than expected based on visible matter alone. The galactic rotation velocity v_{gal} is expected to decrease with the radius r according to Kepler's law $v_{\mathrm{gal}}(r) \propto 1/r^2$, but the observations hint towards a constant v_{gal} up to the visible circumference of the galaxy. This implies the presence of invisible matter in the halo of galaxy dark halo to compensate for the missing mass. For our Galaxy, the local DM density is estimated to be $\rho_{\mathrm{LDM}} = 0.55\,\mathrm{GeV\,cm^{-3}}$ [1]. Further evidence for the existence of DM were also derived from X-ray emission of clusters of galaxies [13] and the anisotropy of Cosmic Microwave Background (CMB) [1].

The theory of axions as dark matter is based on the assumption that the Universe is assumed to be made of ‘cold DM’ [1, 6]. According to this theory, axion DM is hypothesised to have been produced non-thermally during the formation of galaxy through the vacuum misalignment mechanism [14–16]. The misalignment mechanism is the effect that occurs when the initial value of the particle's field is not close to its potential minimum. Under the so called pre-inflationary PQ symmetry breaking scenario [1], the PQ symmetry of the axions is broken pre-inflation or during the inflation period of the Big Bang and these particles would exist now in sufficient concentrations. Axions created through this mechanism can be currently regarded as a coherently oscillating classical scalar field, whose oscillations were established in the early universe, with an axion field amplitude a_0 is given by [1, 17]

$$a(t) = a_0 \cos\left(2\pi \frac{m_a c^2}{\hbar} t + \phi_a\right). \tag{2.1.4}$$

ϕ_a is the local phase of the axion field, which is a random and unknown quantity. The oscillation frequency can be written as

$$f_{\text{osc}} = m_a c^2 / h \tag{2.1.5}$$

Axions are super light, with the mass range predicted from $10^{-7}\,\text{eV/c}^2$ down to $10^{-22}\,\text{eV/c}^2$ [17–19]. By combining this fact with the previously mentioned fact that they interact weakly with ordinary matter, and are stable on the cosmological time scales, axions are well-motivated candidates for dark matter.

Any large-scale interaction of axions with other particles or with themselves would mean that the axion could lose their coherence. But the axion's interactions are extremely suppressed due to the very large scale f_a [20]. Thus, we can say with some certainty that any axion detected now will more or less still oscillate coherently. The formation of clusters from large-scale gravitation effects, such as the formation of galaxies, is the only known process in the universe that could have affected axions (cf. chapter 27 "Dark Matter" of Ref. [1]). These large-scale effects can cause the axion field to virialise and acquire a viral velocity of the galaxy it is in. The virial velocity of our Galaxy is $v_{\text{gal}} \sim 1{\times}10^{-3}\,c$. Thus, the coherent length of the axion, which is no longer infinite, is in the order of the de Broglie wavelength

$$\lambda_{\text{coh}} \sim \frac{1}{m_a v_{\text{gal}}} \sim 200 \left(\frac{m_a}{10\,\mu\text{eV}}\right)^{-1}. \tag{2.1.6}$$

The kinetic energy of the axion limits the coherence time to

$$\tau_{\text{coh}} \sim \frac{1}{m_a {v_{\text{gal}}}^2} \sim \frac{10^{-6}}{m_a}, \tag{2.1.7}$$

which is roughly $1{\times}10^{-6}$ times the period of the axion field.

Emboldened with strong arguments for the existence of axions and with knowledge of some of its properties, in the next section we discuss the various interactions of the axion.

2.2 Interaction of QCD axions and axion-like particles

Axions may interact with known matter through various mechanisms. In this section, description of interactions which are most commonly used (with photon), and interactions which are acquiring prominence and also connected to this thesis (with gluons, EDM operator, nucleon EDM).

2.2.1 Interaction with photons

Axions can be produced in the stellar interiors by the Primakoff conversion of thermal photons in the electrostatic field of electrons and nuclei [21]. To elucidate this in the case of axions, it is the conversion of axions into two photons in the presence of a strong electromagnetic field. Thus is based on axion-photon interaction.

$$\mathcal{L} \ni g_{a\gamma\gamma} a F_{\mu\nu} \tilde{F}_{\mu\nu} = g_{a\gamma\gamma} a \vec{E} \cdot \vec{B} \tag{2.2.1}$$

gives the axion–photon interaction [1]. $F_{\mu\nu}$ is the electromagnetic field strength and $g_{a\gamma\gamma}$ is the coupling constant, $\vec{E}$ and $\vec{B}$ are the electric and magnetic field. Experiments dealing with this interaction and others mentioned here are given in Section 2.3. The storage ring experiment described in this thesis is not sensitive to this coupling.

2.2.2 Interaction with gluons

The direct coupling of axions to gluons, which arises from the Peccei-Quinn formalism, given in Eq. (2.1.2), can generate oscillating EDM in nucleons [17]. Following a similar form as Eq. (2.1.3), the axion-induced oscillating EDM in a nucleon N is given by [17, 22],

$$d^N_{\mathrm{AC}}(t) = S \cdot \kappa_a \frac{e\hbar c}{2mc^2} \frac{C_G}{f_a} a(t) \tag{2.2.2}$$

where, $a(t)$ is axion field and $\frac{C_G}{f_a}$ is the decay constant for the axion in general instead of just QCD axion, S and m are the spin and mass of the nucleon, and κ_a is the chiral suppression factor of the θ_{Q}-term. To account for the difference in the coupling strength between ALPs and QCD axions, the θ_{Q} in Eq. (2.1.2) is replaced by the axion $\theta_a = a(t)/f_a$. Storage ring experiment explained in this thesis makes use of this oscillating EDM to search for ALPs.

2.2.3 Interaction with nucleon EDM

The total EDM of the nucleon d^N is composed of a static part d^N_{DC} and an oscillating part d^N_{AC}. The interaction of the axion with the gluons given by Eq. (2.1.3) induces a coupling of the axion to the operator responsible for generating EDM of the nucleon. This is a model independent coupling and the Lagrangian is given by [1]

$$\mathcal{L}_{aN\gamma} = -\frac{i}{2} g_{aN\gamma}\, a\, \bar{\Psi}_N \sigma_{\mu\nu} \gamma_5 \Psi_N F^{\mu\nu}. \tag{2.2.3}$$

The coupling constant $g_{aN\gamma}$ can be then related to axion-induced oscillating EDM as [1, Eq. 90.38]

$$d^N(t) = g_{aN\gamma} \sqrt{2\rho_{\mathrm{LDM}}} \cos\left(2\pi f_{\mathrm{osc}} t\right)/m_a. \tag{2.2.4}$$

Here, f_{osc} is the axion oscillation frequency and m_a is the axion mass. Storage ring experiments explained in this thesis can determine the size of this coupling.

2.2.4 Interaction with nucleons

The last interaction we discuss is the Weinberg's [4] gradient interaction of axion with fermions f,

$$\mathcal{L}_{aff} = \frac{C_f}{2f_a} \bar{\Psi}_f \gamma^\mu \gamma_5 \Psi_f \partial_\mu a(t), \tag{2.2.5}$$

where, $\bar{\psi}_f$ is an arbitrary fermion field and C_f is a model dependent coefficient, and f can stand for the nucleon N. Note the axion field $a(t)$ here appears a derivative term. According to [22, 23], this Lagrangian can be reinterpreted as the interaction of the spin of the fermion with an oscillating "pseudomagnetic" field. This pseudomagnetic field is generated by the gradient of the axion field, which is directed along the galactic rotation velocity v_{gal} [18].

Storage ring experiments are most sensitive to this coupling.

2.3 Detection of QCD axions and axion-like particles

The existing experimental searches for axions can be divided into three groups. Experiments in which the production and detection of axions happen in laboratories. Experiments in which axions constitute the DM. Experiments that detect the axions emitted by the sun on Earth. The information in this subsection is gathered thanks to the references [1, 21, 24].

2.3.1 Purely lab experiments

Light shining through wall (LSW)

A simplified version of the experimental setup for the light shining through wall experiment [25] contains two regions, both with vertical B-field, the production region on the left and the reconversion region on the right, separated by a wall.

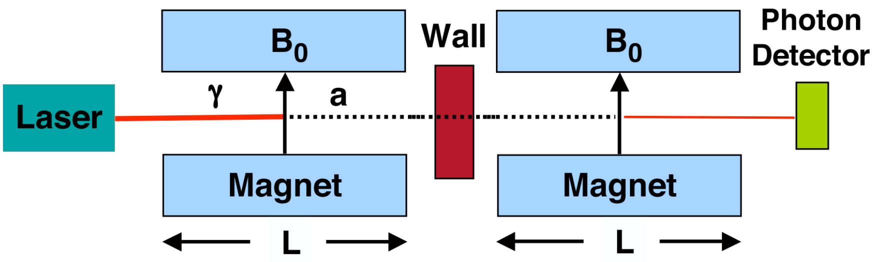

Figure 2.1: Schematics for light shining through the wall experiment with the production region on the left and the reconversion region to the right of the wall. Figure from [26]

The light from a laser is injected into the production region from the left side. In the presence of B-field, the photons can be converted into axions by Primakoff effect. These axions can then travel through the wall, while the light cannot. On the other side of the wall, the axions are converted back to photons in the reconversion region and detected by a sensor attached at the right most end.

References [26, 27] provide an improved detection scheme based on resonant photon regeneration. Experiments in the recent past have been using this technique. ALPS [28] at DESY, CROWS [29] and OSQAR [30] at CERN are experiments that have already provided upper limit on $g_{a\gamma\gamma}$ using this technique. ALPSII [31], STAXI [32] are upcoming experiments which are in development. JURA experiment in a concept at the CERN.

Polarisation experiments

The use of lasers provides another method to detect axions. In the presence of the B-field, the photon-photon interaction can cause dichroism and birefringence of the laser beam whose E-field component is parallel to the B-field [33, 34]. The perpendicular component remains untouched. Dichroism, which is the depletion of polarisation, is caused by the photon to axion conversion. Birefringence is the delaying of phase, caused in this case by photon to axion and back to photon conversion. PVLAS [35], BMV collaboration [36] are conducting experiments using this technique with the primary goal to measure vacuum magnetic birefringence and dichroism.

Long range macroscopic forces

Experiments looking at new macroscopic forces, in theory, could be sensitive to axion effects. The ALP field from macroscopic bodies (from fermionic coupling) could be detected as a from gravity at distances $\sim 1/m_a$. These constraints can be obtained from precision measurements of Newtons $1/r^2$ law and searches for violation of the equivalence principle. Torsion balance experiments, Casimir force measurement are some experiments from which the constraint on $g_{aN\gamma}$.

Reference [37] proposes the use of NMR technique to detect the effect of macroscopic objects on axions and development of experiments based on this method is being done by the ARIADNE collaboration [38].

2.3.2 Detection of solar axions

Helioscopes

Solar axions are produced in the hot and dense solar core. It is mainly produced by the Primakoff conversion of plasma photons in the Coulomb field of charged particles. The expected solar axion flux at earth is expected to peak $\approx 4.5\,\text{keV}$ and decrease exponentially with an increase in energy.

The mainly used detection technique –Helioscopes– was first presented by P. Sikivie [39]. The experimental setup has a long powerful magnet with an X-ray detector attached at the end is aligned towards the sun. The idea was that solar axions can be converted back into photons in the presence of a strong electromagnetic field. If the background field is static, reconverted photons are expected to have the same energy as incoming solar axions. An excess of x-ray flux is expected to be detected over the background. This conversion can be further optimised by filling the entire detector volume with a buffer gas, as proposed in [40].

The most recent concluded helioscope experiment is the CERN Axion Solar Telescope (CAST) [41]. The next-generation helioscope, Internation Axion Observatory (IAXO) [42], which is in the design stage, will be equipped with a new pathfinder system to track the Sun along with the bigger and better detectors.

Primakoff-Bragg conversion in crystalline detector

An extension of Primakoff conversion, in this case the axion is converted to photon in the presence of atomic electromagnetic field inside materials. This conversion can be enhanced if the momentum of incoming particles matches one of the Bragg angles [43, 44]. Using this technique, solar axions can be searched in crystalline detectors [45, 46]. This technique first applied to experiments with small Ge detectors such as SOLAX [47] and COSME [48]. Many other experiments use this technique as a by-product.

Non-Primakoff conversion

Here we look at the solar axion interaction other than axion-photon and via coupling with electron or nucleons. Ionisation detectors can detect solar axions through axioelectric effect g_ae. Large liquid xenon detectors like, XMASS [49], XENON [49], PANDAX-II [50], LUX [51] have performed this search as a by-product of their primary experiment, detection of Weakly interacting massive particles (WIMPs).

2.3.3 Detection of dark matter axions

Most DM axion searches in the laboratory depend on the fact that dark matter, at least the ones we measure on earth coming from the galactic halo, is comprised fully of axions. The absence of a signal provides us an upper limit of the axion coupling under this assumption; the upper limit is a product of $g_a\sqrt{\bar{\rho}_a}$, where g_a is any axion coupling and $\bar{\rho}_a$ is the fraction of axion mass density ρ_a that makes up the local DM density ρ_{LDM} $\bar{\rho}_a = \rho/\rho_{\mathrm{LDM}}$. If $\rho_a \leqslant \rho_{\mathrm{LDM}}$ then we are less sensitive. For purposes of all the experiments mentioned in the thesis, the local axion density is assumed to be the same as local DM density $\bar{\rho}_a = 1$.

As discussed in section Dark matter candidate (2.1.2), DM axions can be considered as a spatially constant field oscillating with an angular frequency $\omega_a = m_ac^2/\hbar$ related to axion mass m_a in Eq. (2.1.4). Many experiments exploit this frequency to search for DM axions.

Haloscopes

Haloscopes, similar to the previously mentioned helioscopes, are the most common way to search for DM axion. This method, also first proposed by P. Sikivie [39], makes use of the inverse Primakoff conversion of axion into photons in a magnetic field $g_{a\gamma\gamma}$ in a resonant microwave cavity with a high Q factor. Within the cavities, this conversion can be enhanced when the frequency of the cavity matches with the unknown axion mass related frequency. The schematic is shown in Fig. 2.2.

Movable rods are introduced inside the cavities, allowing to tune the frequency in search for the resonance. In each scan step or frequency point, the power is extracted from the cavity to a radio-frequency (RF) detector. The expected signal is a narrow peak in the power graph at a frequency corresponding to the mass of axion m_a.

ADMX [52] has been leading the experimental effort in Haloscopes. The collaboration has pioneered not only in the relevant technology but also the sensitivity of the experiment reaches some theoretical models for axions, such as the KSVZ [53, 54] and DFSZ [55, 56]

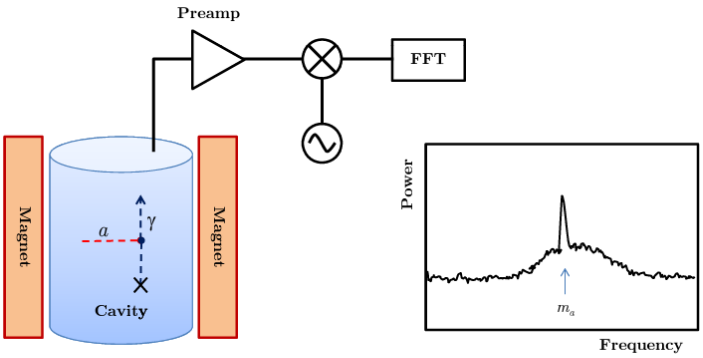

Figure 2.2: Schematic explaining the basic setup for haloscopes. Figure from [24]

The HAYSTAC collaboration [57] has reported that by using squeezed photon state allowed to push the system noise level below the ”standard quantum limits” [58]. The ORGAN [59] experiment was designed to search for relatively high mass axions. Another experiment probing high masses is the QUAX experiment [60]. Both the projects have published the initial results. At CAPP under the project name CULTASK various efforts are done towards search of axions DM, including the reuse of CAST magnets as cavities CASP-CAPP. Similarly, CAST-RADES also uses one of the CAST magnets to search for DM axions.

Other concepts

One drawback of the conventional haloscope is the requirement of the large volume of the cavity as the frequency increases. The concept hinges on large volume large-V and large Q factor large-Q. This gets increasingly challenging to achieve. Innovative ideas have been proposed to circumvent this hurdle.

Dish antennas completely avoid the resonant enhancement technique and compensate with huge amounts of volume, i.e., a huge-V and no-Q experiment. The concept is that photons are emitted by a reflective (or refractive) surface which are immersed in a magnetic field due to the background DM field [61]. This leads to a broadband measurement that is a large range of frequency with a single measurement.

Dielectric haloscopes evolved from the dish antenna concept and have several dielectric slabs stacked inside a magnetic field to reasonably enhance the photon signal in addition to the reflective surface. While not a resonator like a conventional halcoscope, the power emitted will be boosted by a factor proportional to the square of the number of disks. This concept is proposed to be implemented at the MADMAX experiment [62].

Low frequency resonators with LC circuits [63] technique uses a pick-up coil inside a large magnet to detect tiny oscillating electric current induced by DM axions at lower axion masses $m_a < \mu\text{eV}$. An externally attached cooled LC circuit acts as a resonance amplifier and precision magnetometry is required to detect these small oscillations. Some experiment using this technique are ABRACADABRA [64], SHAFT [65], ADMX-SLIC [66] and BASE [67].

ALPHA collaboration plans to use plasma resonators where resonant conversion are achieved by matching axion mass to a plasma frequency [68]. Plasma frequencies are unrelated to the physical size of the device, unlike traditional haloscopes, giving a huge advantage in terms of the size of the device.

Another alternate to the microwave cavity technique is demonstrated in the ORPHEUS detector [69] using a Fabry-Perot resonator and individually adjustable current carrying wire panes.

Spin precession experiment

All the techniques for DM search mentioned until now are primarily based on axion-photon coupling and these constitute the majority of the experimental landscape. Recently, more searches are proposed based on the DM axion-induced oscillating EDM and the axion-wind effect. Both these effects induce oscillations to the spin of the particle at a frequency f_{osc} related to m_a. The particles in the presence of a magnetic field obtain a spin precession frequency f_{spin}. When $f_{\text{osc}} \approx f_{\text{spin}}$ the torque induced by the axion would cause the spin to move away from the initial direction given by the external magnetic field.

The CASPEr experiment [19] aims at searching QCD axion and ALPs using the nuclear magnetic resonance (NMR) technique. The CASPEr-Electric experiment with help of the torque produced by oscillating EDM and the Casper-Wind experiment with the help of the torque produced by the axion-wind would be able to detect axions.

Storage rings experiments of the ilk described in this thesis also implement the spin precessions to search for axion like particles.

2.3.4 Storage ring experiment

Storage rings are closed accelerators in which particle beams are stored or circulated, at a set momentum, for the duration required by the experiment. It also allows for small variation of the momentum without destroying the beam.

COSY is one such storage ring used in this experiment to search ALPs using horizontally polarised beams. Due to the ring's vertical magnetic field, such beams will precess at the frequency given by $f_{\text{spin}} = G\gamma f_{\text{rev}}$, where G is the magnetic anomaly and f_{rev} is the revolution frequency of the particle beam in the ring. The torque produced by axion-wind will cause the spin of the particles to rotate about the axis parallel to the beam direction and torque due to oscillating EDM will cause the spin to rotate about the axis perpendicular to beam direction away from the ring plane with an oscillation frequency of f_{osc} in both cases.

At similar condition to the other spin precession experiments mentioned above, when $f_{\text{osc}} \approx f_{\text{spin}}$, the beam polarisation will rise out of the horizontal plane and gain a vertical component. This helps us observe axions.

The use of storage rings offers a new platform to search for axions by observing the beam polarisation and looking for effects of axions on the spin of a particle.

3 Spin and polarisation

The spin of a particle plays a crucial role in storage ring searches for axions. This chapter will delve into the concept of spin of a particle and polarisation of a particle beam, and their behaviour in the presence of ALP and various instruments in the storage ring. Additionally, we will look into the theory behind polarisation measurement.

3.1 Spin and polarisation

The spin of a particle, denoted by $\vec{S}$, represents its intrinsic angular momentum. The spin quantum number s characterises the magnitude of spin $\left|\vec{S}\right| = \hbar\sqrt{s(s+1)}$. s can take on values of $0, \frac{1}{2}, 1, \frac{3}{2}$ and so on. Particles with half integer spin, such as protons, neutrons $s = \frac{1}{2}$ are called fermions, while particles with integer spin, such as deuterons, $s = 1$ are called bosons.

The spin of a particle can have $2s + 1$ different projections or magnetic states relative to an arbitrary quantisation axis. These states are determined by the quantum number m, which can have the values in the range $m \in [-s, s-1, \ldots, s+1, s]$. For a spin-$\frac{1}{2}$ particle, the possible configurations are $m = \frac{1}{2}, -\frac{1}{2}$. For a spin-1 particle, the configurations are $m = 1, 0, -1$. Figure 3.1 offers a visual representation of these spin configurations.

(a) Spin-1/2 (b) Spin-1

Figure 3.1: Spin configuration for $s = \frac{1}{2}$ and $s = 1$ particle.

3.1.1 Polarisation

In a particle ensemble, such as a particle beam, the average spin of the individual particles is referred to as the polarisation of the ensemble. When all possible spin states are present in equal weightage, the ensemble is described as an unpolarised state, i.e., the polarisation value is zero. In a polarised ensemble, one of the spin states is more populated than the others, resulting in the polarisation of the beam.

For a beam of spin-$\frac{1}{2}$ particles, there are two possible spin states, as mentioned earlier. The fractional population of particles in $m = +\frac{1}{2}$ state is denoted as N^+ and N^- is the fractional population of particles in $m = -\frac{1}{2}$ state, such that the total population is $N^+ + N^- = 1$. The vector polarisation P_V is defined as the difference in populations in the two states and expressed as:

$$P_V = N^+ - N^- \tag{3.1.1}$$

and can range from -1 to +1. A value of $P_V = 1 \text{ or } -1$ indicates complete vector polarisation, where all particles are in the same spin state or aligned along the same quantisation axis. It is essential to specify both the magnitude and direction of polarisation when describing a vector polarisation. The direction is determined by the choice of quantisation axis. For example, if we chose z axis as the polarisation axis and polarisation along this direction $P_z = 1$, then the polarisation along other axes will be zero $P_x, P_y = 0$. For a partially polarised beam, the sum in quadrature of the polarisation along the two different axes cannot exceed unity.

Deuteron polarisation

Let us examine the polarisation of deuteron, which is a spin-1 particle. It has three spin states denoted by $m = 1, 0, -1$ as shown in Fig. 3.1b, and these states have a fractional population of N^+, N^0, N^-, respectively, where $N^+ + N^0 + N^- = 1$. An equal distribution of particle spins among these magnetic states is referred to as the unpolarised state, where the spins are not preferentially aligned along a particular direction, as given by,

$$N^+ = N^0 = N^- = \frac{1}{3}. \tag{3.1.2}$$

The vector polarisation P_V for a deuteron, defined as the difference between the population of $m = +1 \text{ and } -1$ states, is given by:

$$P_V = N^+ - N^-. \tag{3.1.3}$$

Let us consider particles in the $m = 0$ spin state. Although their projection onto the quantisation axis is zero, indicating zero vector polarisation, they are still aligned in the direction perpendicular to the quantisation axis. This alignment is referred to as tensor polarisation and is expressed as,

$$P_T = N^+ + N^- - 2N^0 = 1 - 3N^0. \tag{3.1.4}$$

Here, P_T can have values ranging from -2 to 1.

In experiments aimed at searching for axions in a storage ring, the primary focus is on vector polarisation because the effects of axions are observed on vector polarisation rather than tensor polarisation. For example, the effect of oscillating EDM manifests through the cross product of vectors $(c\vec{\beta} \times \vec{B})$, which is a vector (to be discussed later in the chapter), and do not impact the tensor polarisation. Therefore, tensor polarisation is not considered crucial in this experiment. Additionally, the presence of tensor polarisation can introduce systematics in the measurement, which may result from geometrical imperfections in detector construction or misalignment of the beam. While it is theoretically possible to differentiate these effects, it can be challenging to identify in practice. Therefore, to minimise potential systematic errors, all data in the experiment were obtained using a pure vector-polarised beam. To achieve a purely vector-polarised state with no tensor component ($P_T = 0$), the fractional population

N^0 must have a value of 1/3, see Eq. (3.1.4). Considering the sum of the fractional population is one, the maximum achievable vector polarisation is ±66.66% of the maximum, resulting in

$$-\frac{2}{3} \leqslant P_V \leqslant \frac{2}{3}. \tag{3.1.5}$$

3.2 Theory behind measurement of polarisation

A polarimeter is a device to measure the beam polarisation. It relies on the spin-spin interaction or spin-orbital interaction between the polarised beam particles and either polarised target nuclei in the case of the former interaction or unpolarised target nuclei in the case of the latter. One commonly employed approach for determining the beam polarisation is through the measurement of scattering rates from a target. By observing the rates of reactions induced by deuterons on a target and their subsequent scattering to a detector, we can ascertain the polarisation of the deuteron beam, provided that the reaction's analysing powers (or sensitivities to polarisation) are sufficiently large.

We follow the Madison Convention [70] when describing the coordinate system at the target. In this convention, the incoming particle's momentum $\vec{p}_{\text{inc}}$ is along the z axis, the y axis is defined by the cross-product of $\vec{p}_{\text{inc}} \times \vec{p}_{\text{out}}$, and x axis completes the right-handed coordinate system. Here, $\vec{p}_{\text{out}}$ is the outgoing momenta. Figure 3.2 provides a visual representation of the polarisation direction in this coordinate system. The orientation of the polarisation is determined by the polar angle β, which is the angle between the polarisation direction and the beam direction, and the azimuthal angle ϕ, which is the angle between y axis and the projection of P_V onto the xy plane. The scattering angle of the outgoing particle is given by θ. The angles denoted here are different from the standard spherical coordinates to keep with the convention.

The direction of scattering is influenced by the spin-orbit interaction (similar to L-S coupling in atoms), which is given by $((\vec{r} \times \vec{p}) \cdot \vec{S})$ between the nucleons of the incoming particle and the target. The information presented here is derived from [71]. Figure 3.3 shows two incoming nucleons with spin up incident on a target at a distance $\vec{r}$. For the incident nucleon 1, the cross product $(\vec{r} \times \vec{p})$ points downward or into the paper.

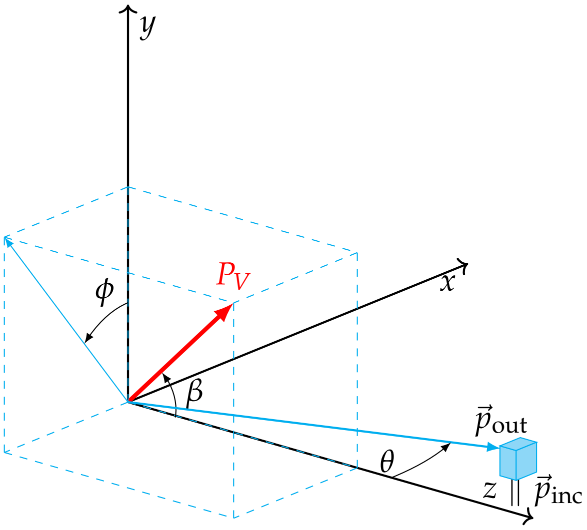

Figure 3.2: Schematic showing the beam coordinates at the target. z axis is chosen along the beam direction, y axis is vertical, and x axis completes the right-handed coordinate system. The red arrow depicts the vector polarisation, the direction of which is given by the angles ϕ and β. The cyan arrow in the xz-plane shows the scattering to the left by an angle θ towards a detector shown in the blue box.

Since the spin is pointing up, the resulting scalar product is negative, leading to a repulsive force between the target and incident nucleon 1, which is scattered to the left. In the case of incident nucleon 2, the cross product points up, and with the spin also pointing up, the scalar product is positive, leading to an attractive interaction and the incident nucleon 2 is pulled towards the target nucleon and thus also scattered to the left. By the similar reasoning, it can be deduced that the spin-down nucleons will scatter to the right.

The angle ϕ in Fig. 3.2 is chosen such that a spin-up particle scatters to the left or in the $+x$ direction when $\phi = 0°$. This follows that the right, up, and down scattering correspond to $\phi = 180°$, $270°$, and $90°$, respectively.

The cross-section of interaction of a pure vector-polarised deuteron beam ($P_T = 0$) and an unpolarised target, such as carbon, as taken from ref. [72], can be expressed as follows,

$$\sigma_{pol} = \sigma_{unpol}\left(1 + \frac{3}{2}A_y P_y\right). \tag{3.2.1}$$

Here, σ_{unpol} is the cross-section for an unpolarised beam, A_y is the analysing power of reaction and P_y is the vertical component (along y axis) of the vector polari-

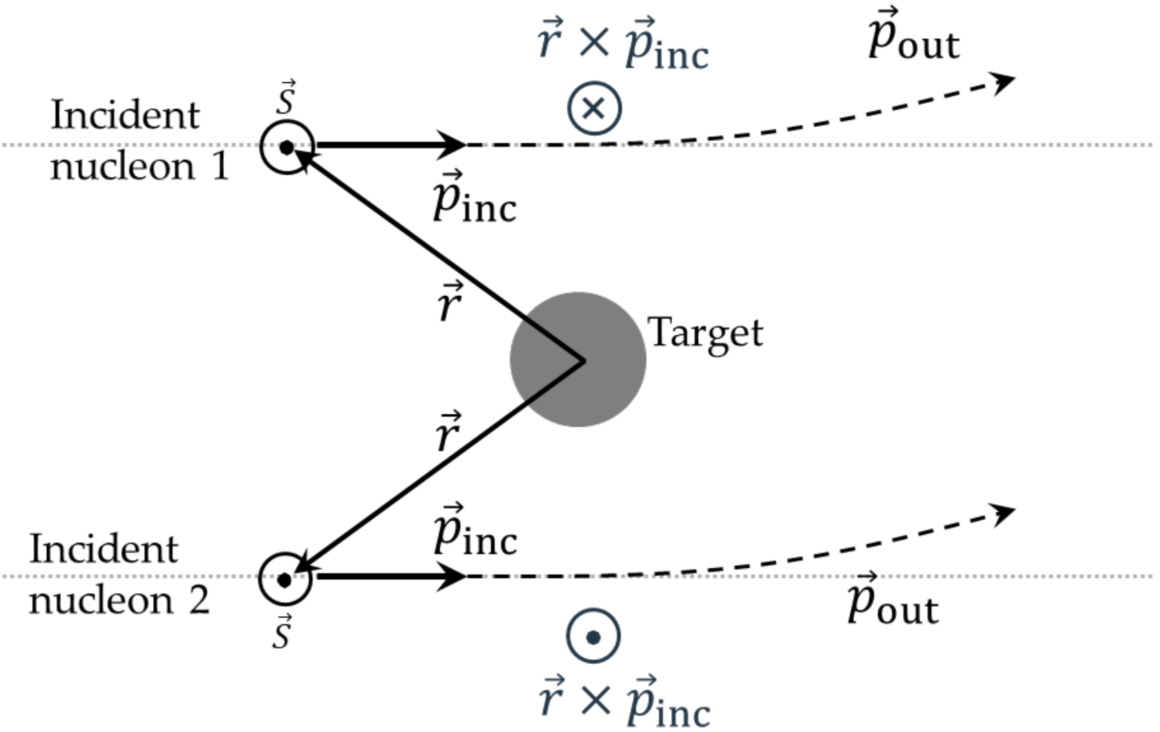

Figure 3.3: Figure adopted from [71] showing the top-down view of incoming nucleons with spins pointing up (or out of the paper) scattering from a target nucleon.

sation of the deuteron beam P_V. The relationship between them is given by $P_y = P_V \sin(\beta)\cos(\phi)$. Terms denoting tensor polarisation are not included in Eq. (3.2.1) as the tensor components are not considered.

The cross-section for a vertically polarised beam (P_y) is maximised when the product $\sin(\beta)\cos(\phi)$ is 1 or -1. Let us assume that P_V is positive. Then the rate at the left detector is highest, when compared to unpolarised beam, when $\sin(\beta)\cos(\phi) \approx 1$. Simultaneously, the rates at the right detector on the opposite side ($-x$) will be at a minimum. If L and R are the rates at the left and right detectors, respectively, the asymmetry in these two rates (assuming that the detector geometry and efficiencies are identical) can be written as,

$$A_{\text{LR}} = \frac{L-R}{L+R} = \frac{3}{2} A_y P_y. \tag{3.2.2}$$

Thus, this asymmetry provides a measure of the vertical polarisation. The analysing power, which is the property of the reaction, is derived from experiments and can be obtained from literature.

Similarly, the asymmetry corresponding to the horizontal polarisation can be written as,

$$A_{\mathrm{DU}} = \frac{D - U}{D + U} = \frac{3}{2} A_y P_x. \tag{3.2.3}$$

Here, D and U are the rates at the down and up detectors, and P_x is the polarisation in the horizontal plane. Next, we will look at the behaviour of particle spin in a storage ring.

3.3 Spin dynamics in a storage ring

Storage rings utilise magnetic or electric field, or a combination of both, to manipulate trajectories of the particles. These fields have a significant influence on the spin of the particles, making it crucial to understand the evolution of particle spin in an accelerator.

Spin precession for particle at rest

First let us start with a particle at rest with magnetic moment $\vec{\mu}$. In an external magnetic field $\vec{B}$ the spin $\vec{S}$ will experience a torque causing it to precess around the magnetic field as follows,

$$\frac{\mathrm{d}\vec{S}}{\mathrm{d}t} = \vec{\mu} \times \vec{B}. \tag{3.3.1}$$

The magnetic moment is related to spin,

$$\vec{\mu} = g \frac{q}{2m} \vec{S}, \tag{3.3.2}$$

where q and m are the charge and mass of the particle, respectively. The gyromagnetic ratio g relates to the magnetic anomaly $G = (g - 2)/2$, and the value for deuteron is $G = -0.142\,987\,542\,4$. By inserting the value of $\vec{\mu}$ in Eq. (3.3.1) we get the equation of spin motion as,

$$\frac{\mathrm{d}\vec{S}}{\mathrm{d}t} = \vec{S} \times \vec{\Omega}. \tag{3.3.3}$$

Here, the angular velocity is given by,

$$\vec{\Omega} = \frac{gq}{2m} \vec{B}, \tag{3.3.4}$$

and aligns with the magnetic field.

3.3.1 Spin precession of relativistic particles

In a storage ring, the particles are moving at relativistic speeds in electric and magnetic fields which guide, focus and accelerate the particles through the ring. Let us consider a particle, with Magnetic Dipole Moment (MDM) and a non-zero Electric Dipole Moment, in this external electric $\vec{E}$ and magnetic field $\vec{B}$. The spin motion in the particle's rest frame can be written as,

$$\frac{\mathrm{d}\vec{S}}{\mathrm{d}t} = \vec{\mu} \times \vec{B}^{*} + \vec{d} \times \vec{E}^{*}, \tag{3.3.5}$$

where, $\vec{d}$ is the Electric Dipole Moment of the particle as mentioned in Chapter 2 and can be related to the dimensionless quantity electric dipole factor η in the similar as $\vec{\mu}$ is related to g

$$\vec{d} = \eta \frac{q\hbar}{2mc} \vec{S}, \tag{3.3.6}$$

with $\vec{d}$ always aligning with the spin direction. The superscript $*$ on $\vec{B}^{*}$ and $\vec{E}^{*}$ denotes fields in particle reference frame. By expressing the $*$ fields in terms of laboratory frame fields with the help of Lorentz transformation, we can derive the time evolution of spin in a storage ring, known as Thomas-Bargmann–Michel–Telegdi (T-BMT) equation [73, 74].

$$\frac{\mathrm{d}\vec{S}}{\mathrm{d}t} = (\vec{\Omega}_{\mathrm{MDM}} + \vec{\Omega}_{\mathrm{EDM}}) \times \vec{S}, \tag{3.3.7}$$

The angular velocity terms $\vec{\Omega}_{\mathrm{MDM}}$ and $\vec{\Omega}_{\mathrm{EDM}}$ arise from the rotations due to MDM and EDM, respectively, and are defined as follows:

$$\vec{\Omega}_{\mathrm{MDM}} = -\frac{q}{m}\left[\left(G + \frac{1}{\gamma}\right)\vec{B} - \frac{\gamma G}{\gamma + 1}\vec{\beta}\left(\vec{\beta} \cdot \vec{B}\right) - \left(G + \frac{1}{\gamma + 1}\right)\frac{\vec{\beta} \times \vec{E}}{c}\right], \tag{3.3.7a}$$

$$\vec{\Omega}_{\mathrm{EDM}} = -\frac{\eta q}{2mc}\left[\vec{E} - \frac{\gamma}{\gamma + 1}\vec{\beta}\left(\vec{\beta} \cdot \vec{E}\right) + c\vec{\beta} \times \vec{B}\right]. \tag{3.3.7b}$$

In these equations, $\vec{\beta}$ is the beam velocity vector in units of c, γ is the Lorentz factor of a particle with mass m and charge q, and $\vec{B}$ and $\vec{E}$ are the external magnetic and electric fields, respectively. Since the COSY ring is purely magnetic with $\vec{B}$ aligned along the vertical direction, we can simplify the T-BMT equation by setting $\vec{E} = 0$, $\vec{\beta} \cdot \vec{B} = 0$.

Furthermore, by choosing a comoving frame of reference that moves with the momentum, it is convenient to express the spin orientation relative to the particle momentum [75]. To achieve this, let us first consider the motion of a charged particle in a purely magnetic field $\vec{B} \perp \vec{p}$ described by the Lorentz force,

$$\frac{\mathrm{d}\vec{p}}{\mathrm{d}t} = \vec{F} = q\left(c\vec{\beta} \times \vec{B}\right) = \vec{\Omega}_{\text{rev}} \times \vec{p}, \tag{3.3.8}$$

where, $\vec{\Omega}_{\text{rev}}$ is the angular velocity of the particle moving under the influence of the magnetic field, and can be expressed as,

$$\vec{\Omega}_{\text{rev}} = -\frac{q}{\gamma m}\vec{B}. \tag{3.3.9}$$

The spin precession relative to the momentum precession can be obtained by the term $\vec{\Omega}_{\text{MDM}} - \vec{\Omega}_{\text{rev}}$. Additionally, as discussed in Chapter 2, another term that can introduce spin rotation is the axion-wind, which can be described by the angular velocity $\vec{\Omega}_{\text{wind}}$ as given in [23, 76]. Incorporating these effects into Eq. (3.3.7), we obtain the subtracted, axion-wind extended T-BMT equation for a purely magnetic ring as follows:

$$\frac{\mathrm{d}\vec{S}}{\mathrm{d}t} = (\vec{\Omega}_{\text{MDM}} - \vec{\Omega}_{\text{rev}} + \vec{\Omega}_{\text{EDM}} + \vec{\Omega}_{\text{wind}}) \times \vec{S}. \tag{3.3.10}$$

This equation describes the spin motion relative to momentum in a purely magnetic ring, where,

$$\vec{\Omega}_{\text{MDM}} - \vec{\Omega}_{\text{rev}} = -\frac{q}{m}G\vec{B}, \tag{3.3.10a}$$

$$\vec{\Omega}_{\text{EDM}} = -\frac{1}{S\hbar}d(t)c\vec{\beta} \times \vec{B}, \tag{3.3.10b}$$

$$\vec{\Omega}_{\text{wind}} = -\frac{1}{S\hbar}\frac{C_N}{2f_a}(\hbar\delta_0 a(t))\vec{\beta}, \tag{3.3.10c}$$

where $d(t) = d_{\text{stat}} + d_{\text{osc}}(t)$ is the EDM of the particle, including the static term d_{stat} and the oscillating term d_{osc}, $a(t)$ is the ALP field, and C_N is the coupling constant. The oscillating ALP field generates the oscillating term in $d(t)$, and the time derivative term $\delta_0 a(t)$ contains the oscillating contribution within $\vec{\Omega}_{\text{wind}}$. Both of these ALP induced effects result in a vertical build-up of beam polarisation out of the ring plane under resonance conditions. Figure 3.4 provides a visual representation of the rotation vectors in the particle rest frame.

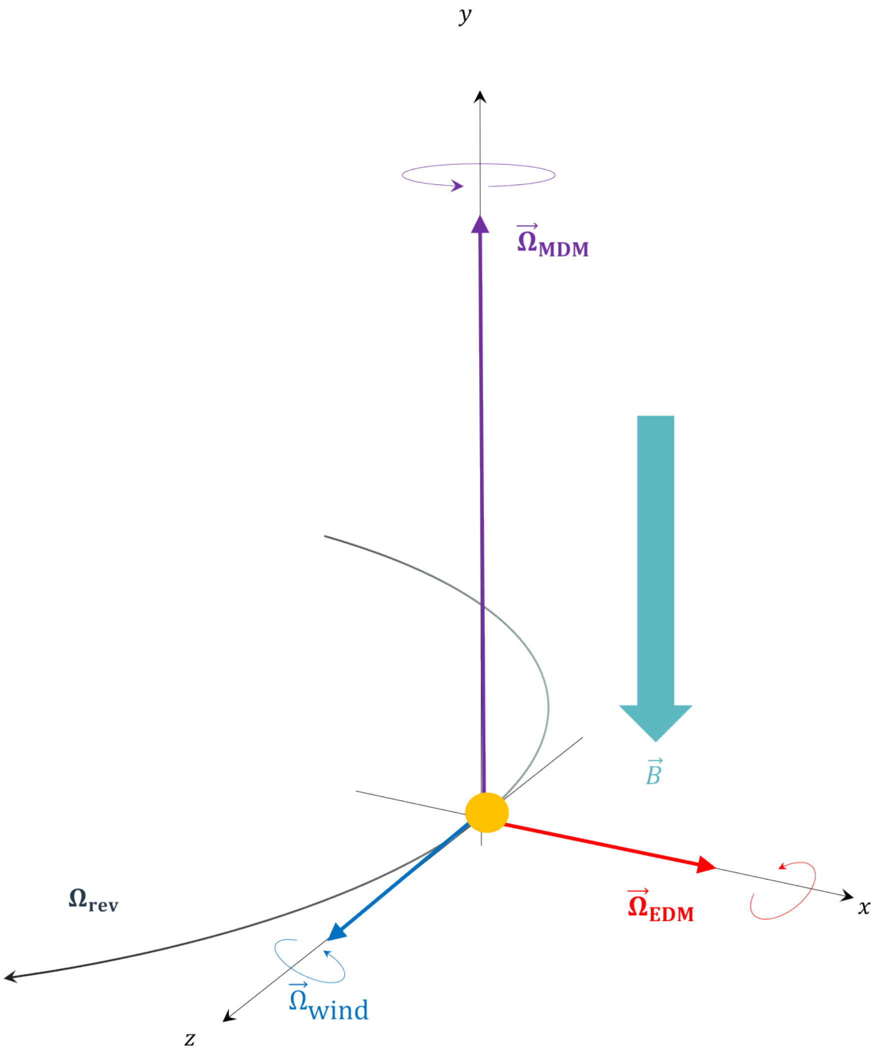

Figure 3.4: The particle in its rest-frame coordinates (co-moving coordinates) as referenced in black, with the magnetic field directed in the $-y$ direction, and the beam momentum in the $+z$ direction. The coloured arrows depict the various angular velocities the particle would experience in a storage ring in the presence of ALPs as given in Eq. (3.3.10).

4 How to search for axion like particles?

The search for ALPs in a storage ring relies on the resonance between the spin precession frequency of the particle beam f_{spin} and the frequency of ALP induced oscillations f_{osc}. This approach is similar to other spin-precession-based experiments to search for axions. The axion-induced frequency f_{osc} is directly linked to the axion mass as, mentioned in Chapter 2, through the equation $f_{\text{osc}} = m_a c^2/h$, where m_a represents the axion mass. Expanding upon the spin dynamics discussed in the previous section for a horizontally polarised beam with non-zero EDM, we examine the changes in polarisation that occur at resonance between f_{spin} (related to $\vec{\Omega}_{\text{MDM}}$ given in Eq. (3.3.10a)), and f_{osc} (related to both $\vec{\Omega}_{\text{EDM}}$ and $\vec{\Omega}_{\text{wind}}$ defined in Eqs. (3.3.10b) and (3.3.10c), respectively).

4.1 Resonance and polarisation build-up

In a storage ring, when a horizontally polarised beam is subjected to a vertical magnetic field, it undergoes precession due to the magnetic anomaly G. This precession results in a spin precession frequency given by $f_{\text{spin}} = |G\gamma| f_{\text{rev}}$. Here, f_{rev} is the revolution frequency of the beam around the ring and γ is the Lorentz factor.

Consider a particle within this beam whose spin is aligned with its momentum, and the direction of the beam is aligned with the z axis. The applied magnetic field $\vec{B}$ in the laboratory frame undergoes Lorentz transformation into the particle rest-frame, resulting in a magnetic field $\vec{B}^*$ and electric field $\vec{E}^*$, the latter pointing towards the centre of the ring. The superscript $*$ indicates that the fields are in the reference frame of the particles. Figure 4.1a provides a visual depiction of these vectors, along with spin and EDM.

Assuming that this particle possesses a non-zero oscillating EDM, the EDM vector aligns with the spin and experiences a torque from the electric field $\vec{E}^*$. When the spin and the momentum are parallel, the torque causes the spin to rotate upward Fig. 4.1b, whereas for an antiparallel orientation, the spin rotates downward Fig. 4.1c. As the spin precesses about the vertical axis, EDM also rotates along with it. This precession leads to spin and momentum being parallel for half of the precession and antiparallel for the other half.

In the presence of axion-induced oscillations, the EDM undergoes oscillation with a frequency f_{osc}, causing the reversal in its direction to become opposite to the spin. Consequently, for half of the time period $(0.5 \times 1/f_{\text{osc}})$, EDM aligns parallel to the spin, while during the other half it aligns antiparallel, as shown in. When the spin precession frequency f_{spin} and the ALP induced oscillations f_{osc} are in resonance, the spin, momentum, and EDM are all parallel to each other for half an oscillation Fig. 4.1b. However, during the other half, the spin becomes antiparallel to the momentum, and EDM. In this case, due to the change in direction of EDM, the direction of the torque due to $\vec{E}^*$ also changes, causing the spin to rotate upward Fig. 4.1d. Consequently, over time, the spin will move out of the horizontal plane into the vertical direction.

To observe the build-up of vertical polarisation, it is necessary to set the machine at the resonance frequency. However, since the oscillation frequency is related to the unknown ALP mass m_a, we need to probe the frequency space to find the resonance between f_{spin} and f_{osc}. This is achieved by slowly varying f_{spin} in search of resonance, although still fast enough to ensure that the entire scanning process does not exceed the coherence time of the axions Chapter 2. The expected signal when crossing the resonance is a change in vertical polarisation to a non-zero value. Further details of the experiment are provided in Chapter 6.

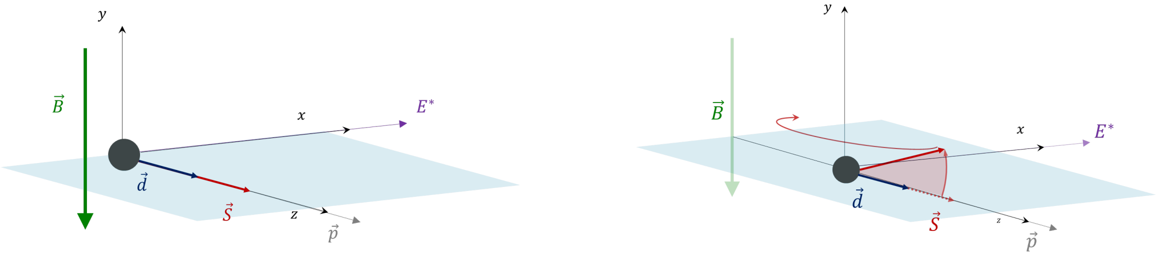

(a) $\vec{S} \upuparrows p$ and $\vec{S} \upuparrows \vec{d}$ (b) $f_{\text{spin}} = 2\pi G\gamma\ f_{\text{rev}}$

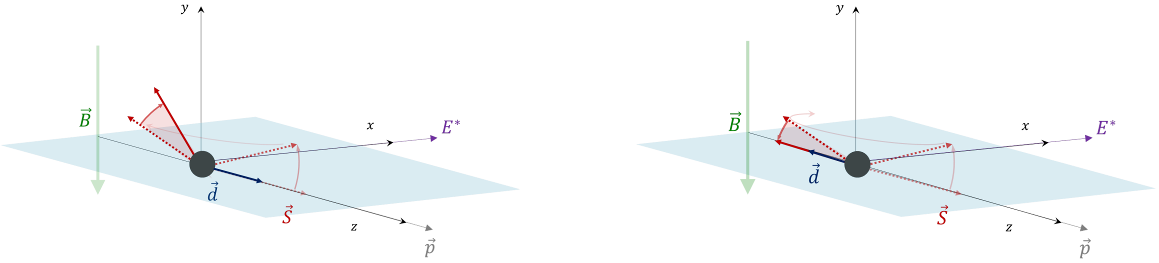

(c) $\vec{S} \upuparrows p$ and $\vec{S} \upuparrows \vec{d}$ (d) $\vec{S} \upuparrows p$ and $\vec{S} \updownarrows \vec{d}$

Figure 4.1: (4.1a) Illustration of a particle in a storage ring with momentum p, in a vertical applied magnetic field $\vec{B}$, experiencing a particle reference frame electric field $\vec{E}*$. (4.1b) When the spin and momentum are parallel, the torque on the EDM kicks the spin to out of horizontal plane. Simultaneously, as the particle traverses the ring, the spin precesses about the vertical axis, resulting in the spin becoming antiparallel to the momentum. (4.1c) When the spin and momentum are antiparallel, the torque causes the spin to rotate downward. This represents a scenario when there is no resonance. (4.1d) The ALP induced f_{osc} leads to oscillations in the EDM. At resonance between f_{spin} and f_{osc}, the EDM and momentum align, being antiparallel to spin. As a result, the torque changes its direction and further pushes the spin upward. As the particle completes multiple revolutions in the ring at resonance, the vertical polarisation will gradually accumulate, resulting in a build up.

4.2 Method

The search for ALPs in a storage ring involves several key steps, beginning with the production of a polarised beam. The beam is injected into the storage ring where it undergoes initial preparation, after which the beam is accelerated to the desired momentum p (the start momentum). Once the momentum is known, it is possible to determine the spin precession frequency of the horizontally polarised beam. A polarimeter placed at the internal target position is used for continuous monitoring of the beam polarisation, which allows us to look for a change in polarisation.

The next step involves searching for a resonance between the spin precession frequency f_{spin} and the axion-induced oscillation frequency f_{osc}. This is done by gradually increasing the spin precession frequency in small steps while maintaining a constant orbit length. In practice, the ramping of spin precession frequency is done by changing the beam momentum, as $f_{\mathrm{rev}} \propto \gamma$. As the resonance is crossed, we expect to observe a change in vertical polarisation, also called a "jump" in polarisation. The magnitude of this change in polarisation will be proportional to the coupling constants of the various axion interactions mentioned in Chapter 2. However, it is important to note that the observed jump cannot be considered as an absolute value, as the jump size can be modulated by the phase of the axion field mentioned in Eq. (2.1.4).

An illustration of the model calculation showing the variation in jump size due to different phases is shown in Fig. 4.2, details on the simulation are provided in Chapter 7. The blue and red curves depict the vertical polarisation component, obtained from the model calculation for two ALP phases, zero and $\pi/2$. In this particular scenario, a substantial jump in polarisation is seen for the former case, whereas a smaller, negative jump is observed for the latter. Since this phase is random for each measurement, and cannot be determined prior to the experiment, this dependence can hinder the sensitivity of the experiment.

In addition to the challenges posed by the modulation of the jump size due to axion phase, another factor that can affect the sensitivity of the experiment is beam depolarisation. Consequently, it is crucial to address both of these challenges prior to conducting the experiment. The following section provides an explanation of the approaches to overcome these challenges.

4.3 Prerequisites

When conducting experiments aimed at measuring minute quantities, any factors that modify the signal pose a huge problem. Since the measurement of the expected signal depends on the polarisation of the beam, it is essential to preserve the beam polarisa-

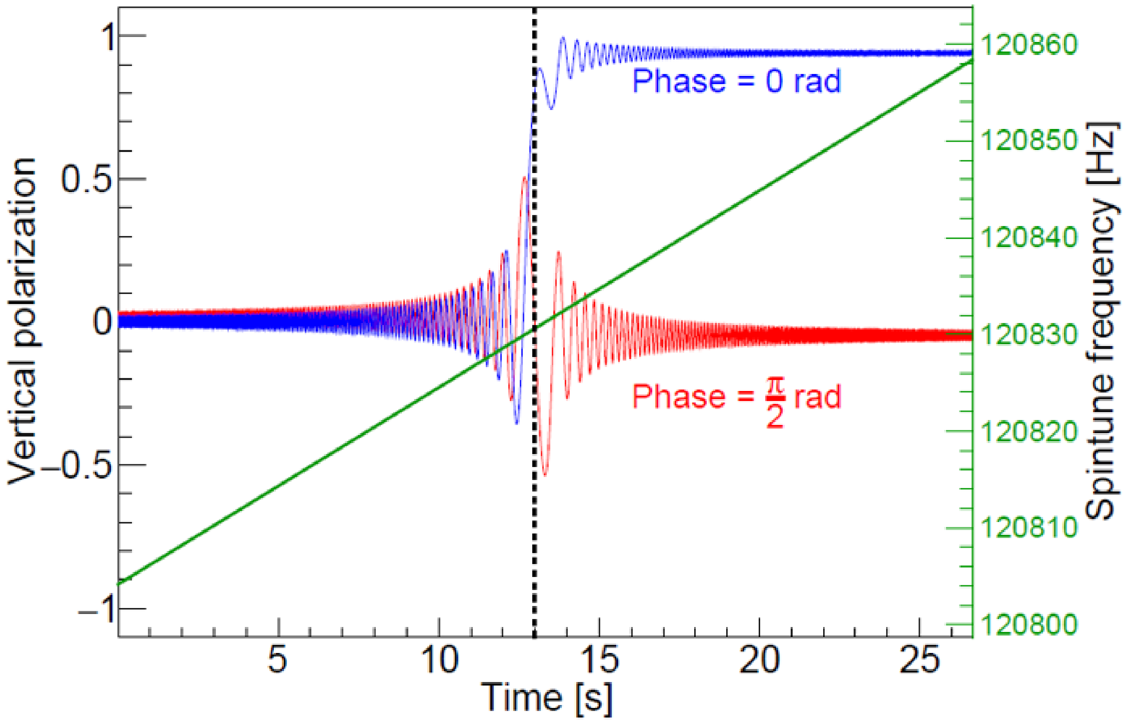

Figure 4.2: Graph depicting the model calculation of vertical polarisation during a scan for the possible resonance between spin precession and the ALP frequency. The changing spin precession frequency is represented by the green line, while the blue and red curves show the vertical polarisation for two different ALP phases over time. Following the resonance crossing at 13 s, the polarisation curves acquire new vertical polarisation values depending on the initial conditions.

tion for the duration of the measurement process. Additionally, we must address the phase dependence of the signal. Let us examine these aspects individually.

4.3.1 Long spin coherence time

We expect to observe a change in polarisation from the horizontal plane to the vertical direction as an indication of a resonance, and thus the presence of axions. To maximise the potential polarisation jump, it is crucial to possess a large beam polarisation in the horizontal plane. This polarisation, referred to as the in-plane polarisation (IPP), is the measure of alignment of the spin of all particles in a single direction in the horizontal plane. As the beam undergoes depolarisation, the experimental sensitivity to detect axions diminishes correspondingly. The duration for which the beam remains polarised is called spin coherence time, and we want to ensure the spin coherence time (SCT) is at least as long as the measurement duration. SCT is usually calculated as the time required for the polarisation to decrease to half its initial value. The process of obtaining long SCT, as explained in this section, is based on [77].

The depolarisation of an IP polarised beam is primarily caused by the momentum spread Δp. We know that, in a magnetic field, the IP polarised beam undergoes precession in the plane with a spin precession frequency f_{spin}. The number of spin precessions per revolution of the particle in the storage ring is called spin tune ν, and can be used to explain how a change in momentum affects the IPP. By using the angular velocity vectors from Eqs. (3.3.9) and (3.3.10a) we obtain,

$$\nu = \frac{(-q/m)G}{-q/(\gamma m)} = G\gamma. \tag{4.3.1}$$

The relationship between a change in spin tune and momentum can be expressed as,

$$\frac{\Delta\nu}{\nu} = \frac{\Delta\gamma}{\gamma} \propto \frac{\Delta p}{p} \propto \frac{\Delta l_{\text{circ}}}{l_{\text{circ}}}, \tag{4.3.2}$$

where l_{circ} is the orbit circumference. It is evident from Eq. (4.3.2) that any deviation in momentum away from the central value p causes a change in spin tune. Overtime, this would lead to a spread in spin tune in a particle beam.

If we consider a case of no variation in spin tune, i.e., $\Delta\nu \approx 0$, the spins of the particles will precess at the same rate, resulting in all particles having the same spin orientation within the xz plane, thereby preventing depolarisation. Conversely, if there is a non-zero spread in spin tune $\Delta\nu \neq 0$, the particle spins will precess at different rates, causing loss of polarisation after multiple revolutions in the ring, as visually depicted in Fig. 4.3.

Bunching with RF cavity

The primary contribution to the spin tune spread comes from the large spread of momentum distribution $\frac{\Delta p}{p}$ in a coasting beam, i.e., a beam of particles that are not bunched together. This first-order effect can be mitigated by using a radio frequency

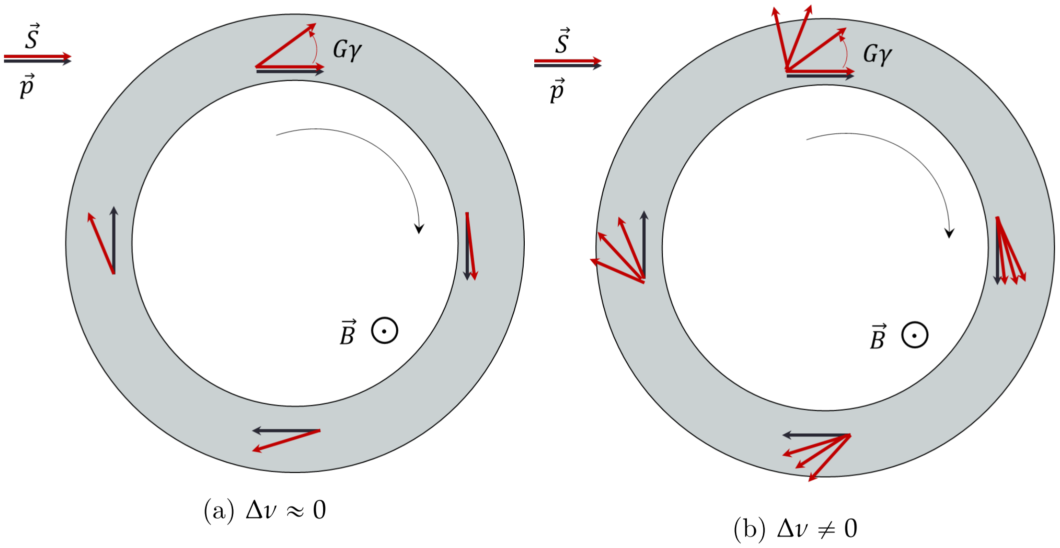

(a) $\Delta\nu \approx 0$

(b) $\Delta\nu \neq 0$

Figure 4.3: Top-down view of a ring with the magnetic field pointing into the figure and beam moving in the clockwise direction. The particles starting at the top of the ring have their spin and momentum vectors parallel. As the particle revolves around the ring, we observe that the spin lags behind the momentum, resulting in a rotation angle of $G\gamma$ rad after one revolution. If $\Delta\nu \approx 0$ then all spins rotate at the same frequency and the in plane polarisation is preserved. However, when $\Delta\nu \neq 0$, the individual spins rotate at different frequencies, leading to different spin orientations over multiple turns and resulting in depolarisation. Figure adopted from [78].

cavity (RF cavity) which applies an oscillating field, causing the particles to bunch together [79]. Particles that arrive with the expected momentum or on time will see zero potential. Particles arriving early or later experience fields which decelerate or accelerate them, respectively.

Sextupole field correction

Betatron oscillations present another factor that changes the spin tune of particles. These are transverse oscillations about the orbit resulting in an increase in path length. To compensate for the increased length, a particles within a bunch must travel faster to still remain bunched, thus changing the spin tune. These second-order contributions are corrected for with the aid of sextupole fields [80], which adjust the length of the betatron oscillation orbit, ensuring that all particles have the same orbit length and thus minimising the spin tune spread [81, 82].

Phase space reduction with electron cooling

In addition to the RF cavity and the sextupole fields, the SCT can be increased by incorporating an electron cooler [83]. Electron cooling, which was first described in [84], is a process aimed at reducing the size, divergence, and energy spread of a charged-particle beam while preserving its intensity. The process involves injecting a dense electron beam along the charged particle beam with the same average velocity. In the rest frame of the electrons, the deuterons passing through the electron beam at different angles and velocities resembles the motion of particles in a hot gas. Through Coulomb interaction, the deuterons exchange energy with the electrons, eventually reaching thermal equilibrium. As a result, the motion of deuterons in the electron rest-frame is damped, leading to a narrower distribution of deuteron velocity components. Consequently, the “cooled” deuteron beam has a reduced transverse motion. This process can increase SCT as we have shown in [85].

Figure 4.4 presents a replicated version of the plot from [85, Figure 4, 5], where the data points correspond to the normalised horizontal polarisation measured at four different time points during a single beam store. A curve was fit to the measurements to facilitate the determination of the SCT. The left plot Fig. 4.4a represents measurements conducted with a pre-cooled beam, while the right plot Fig. 4.4b represents measurements conducted with continuous cooling. The study concluded, as illustrated in Fig. 4.4, that continuous cooling resulted in an improvement in the SCT. However, despite this finding, the storage ring axion search experiment was conducted with a pre-cooled beam due to the systematic effect of electron cooling on spin precession.

4.3.2 The ALP phase problem

As discussed in Section 2.1.2, axions, as candidates of dark matter, can be treated as a scalar field. The axion field is expressed in Eq. (2.1.4), which can be modified as

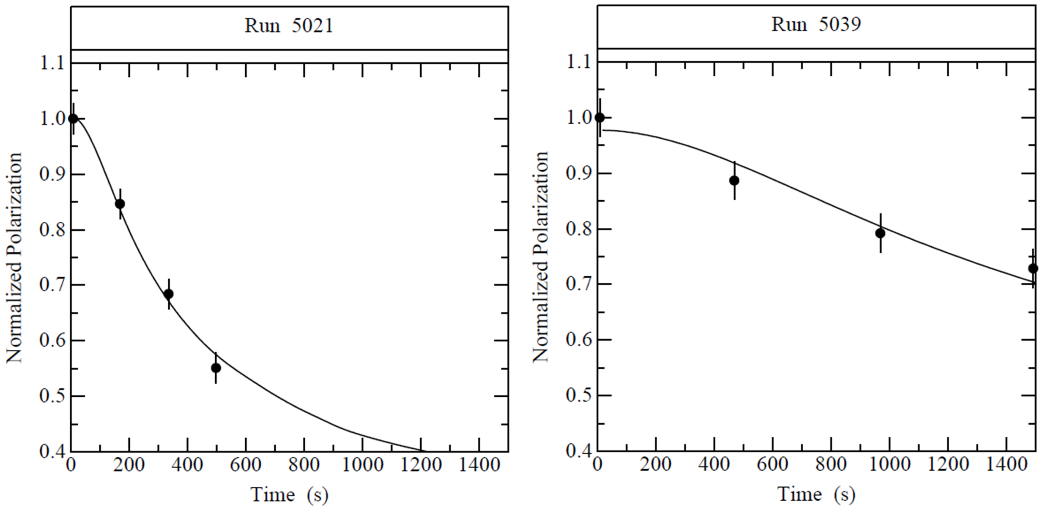

(a) Pre-electron cooling. (b) Full electron cooling.

Figure 4.4: The two plots, taken from [85], depict the normalised horizontal polarisation as a function of time along for two different cases. The data in the left plot corresponds to measurements conducted with electron pre-cooling, while the data in the right corresponds to measurements conducted with continuous electron cooling for the duration of the measurement. The fitted curve was used to estimate the SCT.

follows:

$$a(t) = a_0 \cos\left(\frac{f_{\text{osc}}}{h}(t - t_0) + \phi_a(t_0)\right). \tag{4.3.3}$$

Here, t_0 is introduced to denote the starting time of a measurement and correlate time-wise the properties of the axion field with the state of momenta and spins of the beam particles. The axion phase $\phi_a(t_0)$ now corresponds to the phase between rotating IPP and oscillating EDM. The values of $\phi_a(t_0)$ varies from one measurement to another, resulting in modulation of the signal by a random value each measurement, which would follow a sinusoidal curve. Consequently, depending on the axion phase, the signal can be attenuated or completely absent (Fig. 4.2), neither of which are desirable.

To address the axion phase problem, one possible solution is to observe the signal using two beams having perpendicular in-plane polarisation. These two beams will have a relative phase of $\pi/2$. This configuration enables the experiment to be sensitive to all phases at any given time, ensuring that no ALP signal is missed.

As long as the polarisation directions are perpendicular in the laboratory frame, it is sufficient to have two simultaneous beams to perform axion searches. However, in the actual measurements, we used four simultaneous beams, which were practically achieved by dividing the beam into four separate groups of particles called “bunches” during the bunching process. This choice, while enabling for perpendicular polarisation directions, also provides with opposite polarisations, which is helpful in suppressing systematics. Model calculations performed to study this are provided in Chapter 7. Additionally, selecting four bunches results in tighter grouping of particles within each bunch, potentially aiding in minimising depolarisation effects.

5 Beam preparation and polarimetry

5.1 Cooler Synchrotron COSY

The JEDI collaboration [86] has been conducting research and development of technology towards building a dedicated ring for the search of static EDM of charged particles at the Cooler Synchrotron facility [87] located at Forschungszentrum Jülich, Germany.

COSY is capable of accelerating and storing both polarised and unpolarised proton and deuteron beams in a momentum range 0.3 GeV/c - 3.7 GeV/c. In this experiment to search for ALPs, we utilised a polarised deuteron beam with a nominal momentum p of 0.97 GeV/c, corresponding to an energy of 236 MeV. The COSY facility, seen in Fig. 5.1, comprises an ion source (not shown in Fig. 5.1), the pre-accelerator Jülich Isochronous Cyclotron (JULIC) which accelerates the beam to injection energy, the Low Energy Polarimeter (LEP) to measure beam polarisation pre-injection, the injection beamline, and the COSY storage ring.

Within COSY, several apparatuses are present, including three families of sextupole magnets, an electron cooler, a radio frequency solenoid, a radio frequency Wien filter, and the forward detector from the WASA facility serving as a polarimeter. Let us trace the path of the deuteron beams from the source, through the beam pipes, to the detector.

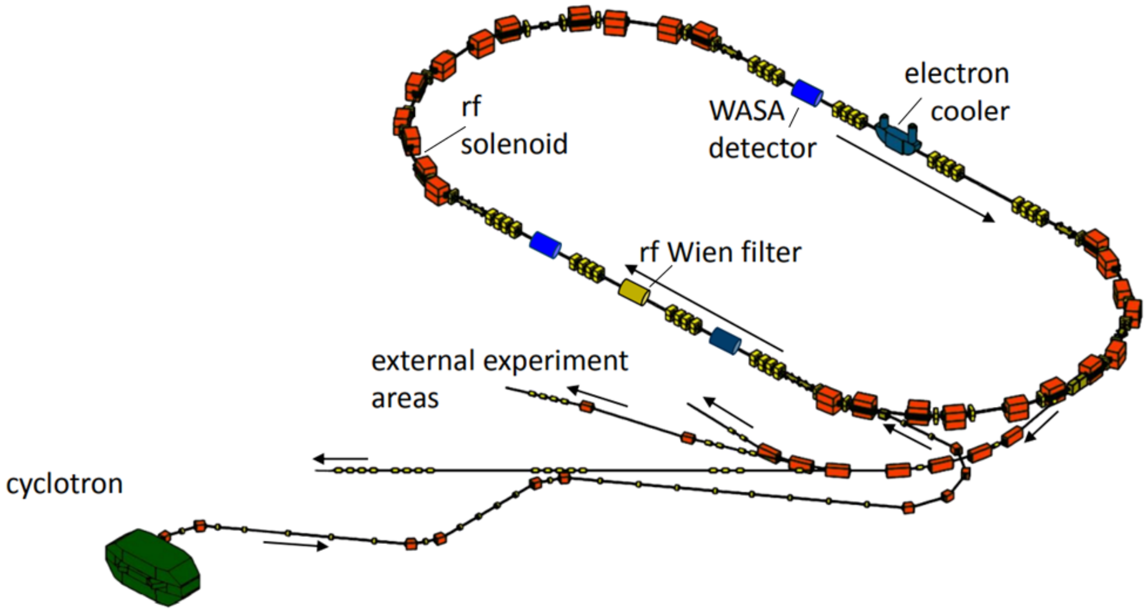

Figure 5.1: Schematic representation of COSY. Starting with the JULIC cyclotron on the left, the injection beam-line connecting it to the COSY ring, extraction beam-line. COSY ring houses the bending dipole magnets, the focusing quadrupole magnets, sextupole magnets, electron-cooler, Wide Angle Shower Apparatus (WASA) operated as a polarimeter, RF Wien filter, radio frequency solenoid (RF solenoid).

5.1.1 Beam production and injection to COSY

The polarised ion source [88] in COSY can produce negatively charged hydrogen H^- and deuterons D^-. In this thesis, we will focus on D^- beam which possesses vector polarisation as explained in Section 3.1. The vertically polarised D^- ion beam from the source is injected into the JULIC cyclotron, where the beam is accelerated to injection energy of 75.6 MeV. Subsequently, the beam is directed into the injection beam line where the LEP is located. The LEP [89] monitors the polarisation of the beam generated at the source. Following the injection beam line, the D^- is strip-injected into COSY. Strip injection involves hitting the D^- beam into a stripping foil which removes the electrons, thereby resulting in the filling of COSY with deuteron ion beams.

5.1.2 Beam development and spin manipulation

The COSY ring has a race-track shape, with a circumference of 183.6 m. The ring comprises two arc sections, each having a radius of 16.5 m and consisting of bending magnets—the dipoles, and three families of sextupole magnets. The RF solenoid is also installed in one of the arcs. The two straight sections connecting the arcs have a length of 40 m and contain quadrupoles responsible for beam focusing and de-focusing. Other important installations in the straight sections are an electron cooler (e-cooler), the WASA detector, and the RF Wien filter.

RF cavity

The RF cavity located in the centre of a straight section, generates a longitudinal oscillating voltage which accelerates the deuteron beam. The initial momentum p of 970 MeV/c corresponds to the revolution frequency f_{rev} of 750 602.6 Hz. By utilising the ability of the RF cavity to operate at various harmonics, the frequency of the cavity was set to the fourth harmonic of the revolution frequency. Consequently, the deuteron beam, instead of being grouped together as a single bunch, is split into four bunches. These bunches, containing approximately equal numbers of particles, and evenly spaced within the ring, will result in mutually perpendicular in-plane polarisation directions. This arrangement will effectively address the phase problem, which will be explained through simulations in Chapter 7.

RF solenoid

The RF solenoid is one of the spin manipulation devices available at COSY. An image of RF solenoid installed in one of the arcs is shown in Fig. 5.2. It is 57.5 cm-long and consists of a 25-turn air-core copper coil with an average diameter of 21 cm [90].

The RF solenoid generates a sinusoidal magnetic field aligned with the beam direction. The vertical polarisation of the deuteron beam undergoes rotation about the solenoidal magnetic field. Furthermore, when the polarisation possesses a horizontal component, it undergoes precession about the vertical magnetic field. The combination of these two rotations results in oscillation of the polarisation, and the oscillation amplitude will depend on the rotations frequencies [91].

When the RF solenoid frequency is in resonance with the spin precession frequency $f_{\text{sol}} = (k \pm G\gamma) f_{\text{rev}},\ k \in \mathbb{Z}$, the polarisation of the beam undergoes oscillations with the maximum amplitude. This phenomenon is employed in the experiment to flip the polarisation to a horizontal plane. Model calculations demonstrating this effect are explained in Chapter 7.

Figure 5.2: RF solenoid installed in the ring.

RF Wien filter

RF Wien filter is another spin manipulation device, installed in the straights of the ring [92]. The device was specifically developed to facilitate the measurement of the static EDM of deuterons at COSY. The design model of RF Wien filter is shown in Fig. 5.3. The orthogonal electric and magnetic fields are homogeneous throughout the length of the WF and fall sharply at the ends. Along with various support structures, it also contains a Beam Position Monitor (BPM) and a belt drive which allows rotating the RF Wien filter up to 90°. It produces sinusoidal electric and magnetic fields that are perpendicular to each other and to the beam momentum. The precision of the RF Wien filter is such that under proper working conditions the fields affect only the spin of the particles, and not their orbit or momentum. The RF Wien filter can be operated in two modes: MDM mode and EDM mode. In the MDM mode, the magnetic field is in the vertical direction and its effects on spin are similar to that of Magnetic Dipole Moment. The MDM-mode is rotated 90° from the EDM-mode. In the EDM-mode, the magnetic field of the RF Wien filter is in the horizontal plane, its effect on the spin is close to that of oscillating EDM. There is a major difference between the effects of oscillating EDM and RF Wien filter; the latter acts at only one point in the ring, while the effect of oscillating EDM is present everywhere in the ring.

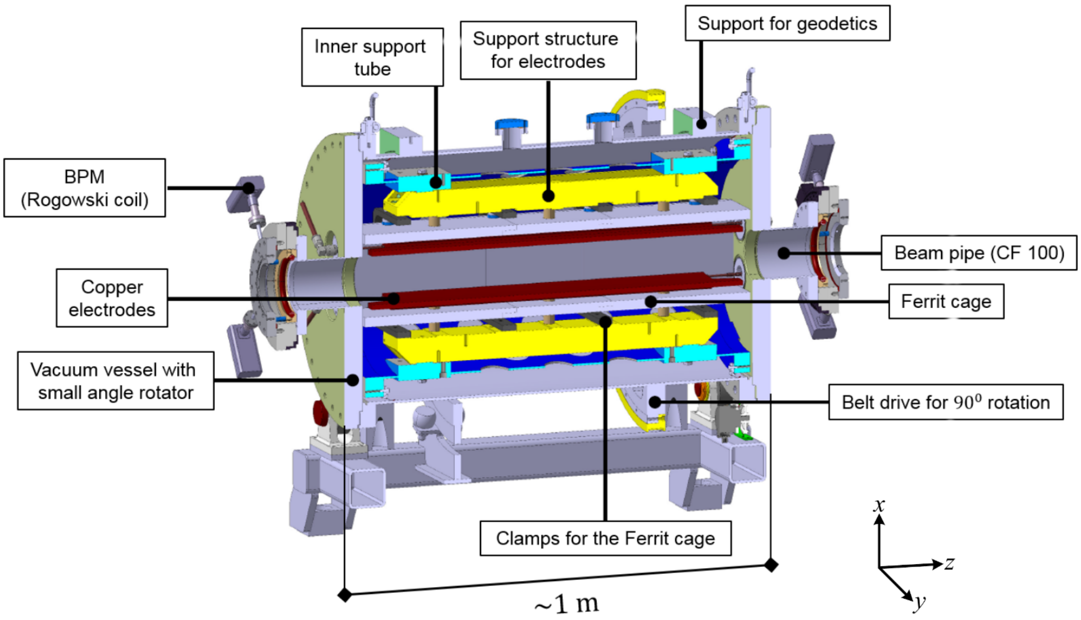

Figure 5.3: Design model of RF Wien filter taken from [92]. The parallel copper plates lie along the beam axis.

Nevertheless, the RF Wien filter could be used to create a test signal and confirm our model calculation.

5.2 WASA polarimeter

The COSY ring is equipped with the forward angle Wide Angle Shower Apparatus detector. Figure 5.4 shows the various elements in the detector. The particles scatter from the carbon target in the forward direction and exit the vacuum through a stainless-steel window. Then they pass through two plastic scintillator window counters, straw tubes, trigger hodoscope, and five layers of plastic scintillator calorimeter detectors or range hodoscope. Except the straw tubes, all layers are divided into pie-shaped segments and are read out using photomultiplier tubes.

The carbon target with the thickness of 2 cm is inserted such that the edge of the target is aligned with the centre of the detector. In order to accommodate this, a local adjustment was made to lower the beam path by approximately 3 mm as it passed the

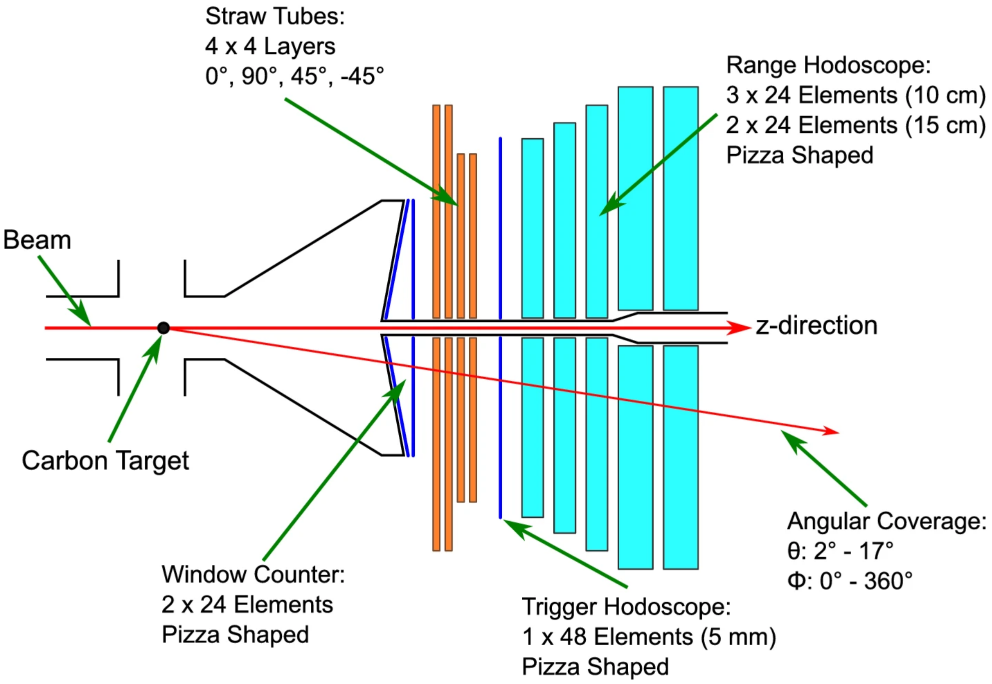

Figure 5.4: Cross-sectional diagram showing the layout of the WASA Forward Detector, taken from [93]. The red arrow gives the beam direction.

carbon target. During the data acquisition, an RF noise generator (called Schneider box) is used to apply heating to the beam. The frequency of the noise generator is set to one of the harmonics of vertical tune. This heating in the vertical direction, causes the particles in the outer part of the beam to rise and hit the front face of the target as illustrated in Fig. 5.5. These particles undergo scattered and are detected in the WASA forward detector. The analysing powers of elastic scattering are given in [93]. The observed detector rates are dominated by elastic scattered deuterons.

Although there are several layers in the WASA detector, for the purposes of polarimeter measurement, only the plastic scintillators are used. This simplifies the analysis scheme and enables the online analysis during the experiment, while being fully sufficient for later analysis purposes as well. The detector segments can be divided into four quadrants in its azimuthal angle, named Left, Up, Right, and Down. The left-right and down-up asymmetry calculated from the rates of these quadrants are used to measure the vertical and horizontal polarisation, respectively (explained in Section 3.2).

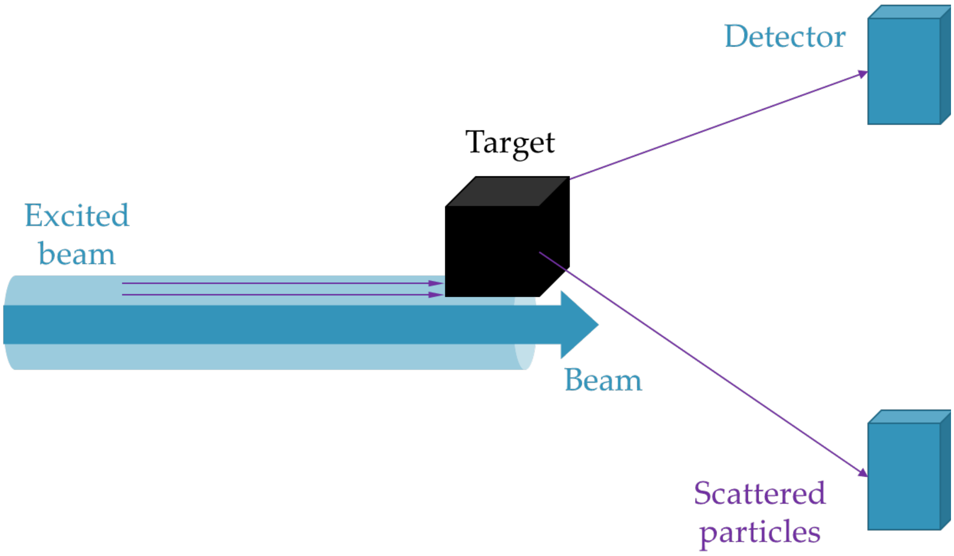

Figure 5.5: Illustration depicting the excitation process of the beam. The beam is represented by a thick blue arrow, and the light blue cylinder represents the excited beam region. The trajectories of two particles within the beam are shown by purple arrows that strike the front face of the target (black cube) and then scatter to the detectors (blue boxes). Please note that the diagram is not drawn to scale.

6 Experiment

Building upon the information presented in the previous chapters, this chapter explains the experimental procedure applied to search for ALPs at the COSY synchrotron. This poof-of-principle experiment took place in the spring of 2019 [94, 95] using a polarised deuteron beam and consisted of a two-step process: an initial one-time setup at the beginning of the beam time to establish the operation point of the experiment, followed by the actual experiment to search for Axion-Like Particles.

To facilitate understanding, the following terms are explained within the context of the experiment.

Cycle

A cycle refers to one complete storage of the particles in the ring, encompassing a particular set of machine instructions dictated by the timing page. A cycle starts from the injection of particles into the ring, while at the end, any remaining particles are dumped, and preparations for the next cycle start. During each cycle, the particles can be in either a polarised state or an unpolarised state. Cycles are numbered from 1 to $\mathcal{N}$ and Fig. 6.1 is an example of detector rates as a function of time in a cycle.

Run

A run is a collection of cycles—characterised by the same beam parameters—that is executed without any break between cycles. The number of cycles in a run varies depending on the specific purpose, ranging from 5 to 10 cycles, the reason for it will be explained later in the chapter. In certain cases, specific cycles within a run may be discarded later if for some reason certain things, such as the Data Acquisition (DAQ), did not operate as intended. A run, usually consisting of multiple polarised cycles, also includes an unpolarised cycle as a measure of the polarisation baseline.

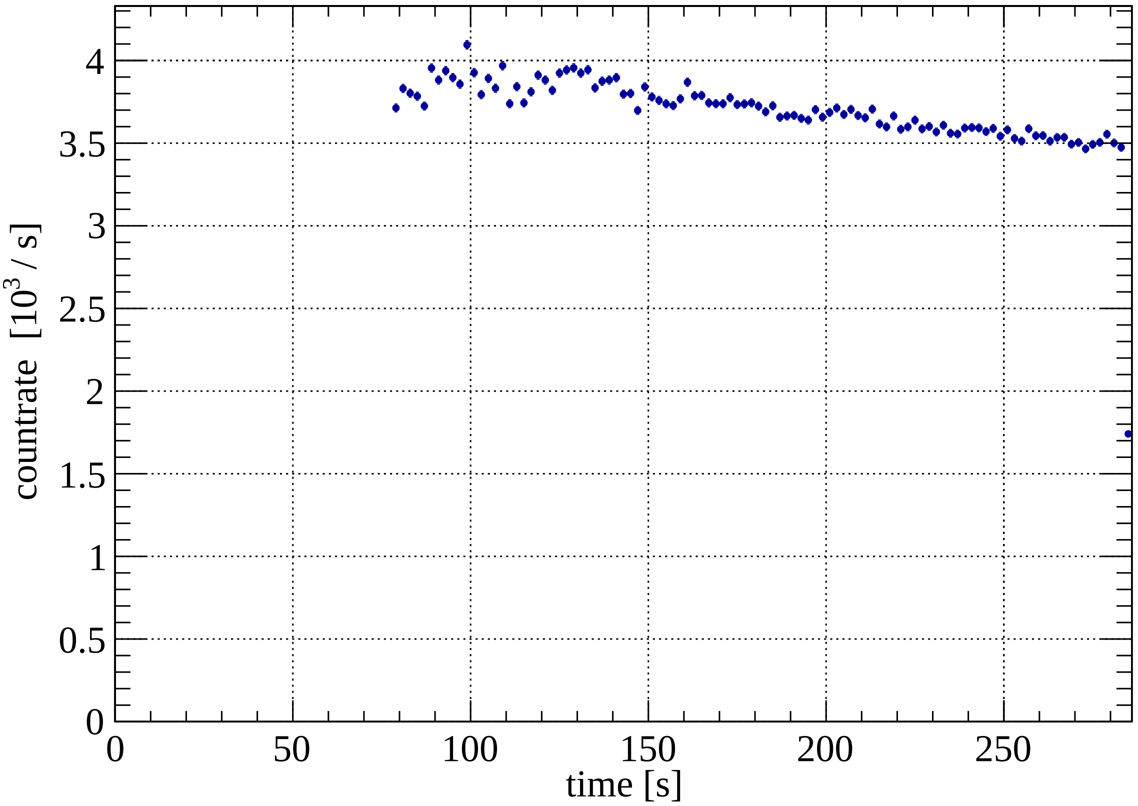

Figure 6.1: The figure shows the 'Up' detector rates for a single cycle in the experiment.

6.1 The one-time setup

The following steps were executed at the start of the beam time to obtain the necessary machine operating conditions. These steps were not repeated unless there were significant changes to the machine settings, which occurred infrequently. The machine settings were optimised for good beam intensity, to obtain high efficiency of injection into the beam pipe, and to determine the optimal beam path or orbit through the ring. This reference orbit served as a benchmark to calculate orbit deviations during the experiment. Data from BPMs distributed around the ring were monitored with the goal of minimising the root mean square (RMS) of these deviations.

Our aim was to have approximately 10^9 deuterons in the ring at the start of each cycle. However, this value varied throughout the experiment by up to a factor of two as a result of fluctuations in the source and the machine operation. An insufficient number of particles would pose challenges to measurements, such as an increase in both the statistical uncertainty in the polarisation measurement and the uncertainties in BPMs readings. The latter would result in inaccurate orbit measurements, while the former would reduce the sensitivity of the experiment.

6.1.1 RF solenoid resonance frequency and spin flip

As mentioned in previous chapters, the polarised deuteron beam from the source is vertically polarised. To rotate this polarisation to the horizontal plane, we utilised the RF solenoid at resonance. While the resonance frequency can be calculated using the formula $f_{\mathrm{sol}} = (1 + G\gamma)f_{\mathrm{rev}}$, where G is the magnetic anomaly, f_{rev} is the nominal revolution frequency, and γ is the Lorentz factor, it is prudent to experimentally determine the resonance frequency due to potential deviations in the experimental conditions from our assumed values of f_{rev} and γ. To obtain the precise resonance frequency of the RF solenoid, a variable-frequency Froissart-Stora scan [96] was performed, followed by a series of fixed-frequency scans. The Froissart-Stora scan involved changing the solenoid frequency f_{sol} across the expected resonance and looking for the flip in polarisation direction of the vertically polarised beam. The Froissart-Stora formula

$$P_f = P_i \left[2e^{-\dfrac{\pi \epsilon_{\mathrm{sol}}^2}{2|\alpha|}} - 1 \right], \tag{6.1.1}$$

describes this change in polarisation when the solenoid frequency crosses the resonance. Here, P_i and P_f are the polarisation before and after the resonance crossing, respectively. The resonance strength is denoted by ϵ_{sol}, and α is the rate at which the resonance is crossed. By identifying the frequency associated with the change in polarisation sign, we obtain the initial estimate of the resonance.

Subsequently, at a fixed f_{sol}, the frequency and amplitude of the polarisation oscillations produced by the solenoid were calculated. This process was repeated at different f_{sol} with 0.1 Hz change between each measurement. The frequency corresponding to the highest amplitude was chosen as the solenoid operating frequency $f_{\mathrm{sol}} = 629\,755.3\,\mathrm{Hz}$.

Once the resonance frequency was determined, the duration for which the RF solenoid was turned on was varied to achieve a half flip of the polarisation, resulting in zero vertical polarisation. This was confirmed by comparing the LR-asymmetry A_{LR} value with that of the previously measured unpolarised cycle as a reference.

6.1.2 Long spin coherence time using sextupole scans

Long spin coherence time is an essential aspect of this experiment, and a crucial step towards achieving this is to cancel the effects of betatron oscillations by adjusting the sextupole fields, as explained in Chapter 4. The ring has three families of sextupole magnets that are strategically located in the arcs. These sextupole magnets, namely MXS, MXL and MXG, are located at positions in the ring with large Courant-Snyder parameters β_x and $beta_y$, and large horizontal dispersion, respectively [82]. Here, β_x and β_y are the horizontal and vertical beta functions, which are related to the transverse size of the beam.

The process involved optimising the sextupole field values to find the optimal sextupole field setting that yields long SCT. Since the horizontal and vertical tunes are not strongly coupled to each other [82], the settings of MXL can be varied independently of MXS and MXG. Initially, with a constant value of MXL field, the values of MXS and MXG fields were linearly varied, and the SCT was calculated for each setting from the online data. This analysis was later performed offline and the method to calculate SCT from the asymmetry data will be explained in Chapter 8. Once the maximum SCT was found from the scans of MXS and MXG fields, with these fields fixed, the scan of MXL fields was done to determine the conditions for achieving long SCT. For each setting, a run consisted of four cycles, and the SCT was determined by taking the average of all the cycles. Once the values of the three sextupole magnets were known and set, the machine was prepared for the frequency scans aimed at searching axions.

6.2 Frequency scans

The frequency scans were designed to search for the resonance that indicates the presence of axion. During these scans, each cycle involved scanning a specific range of frequencies. The timing of specific operations within a cycle, for different run types, is given in the Table 6.1. Axion scans will be explained in this section, while the RF Wien filter scans and calibration will be explained in Section 6.3. A cycle with specific operations and frequency range was repeated multiple times, constituting a run. Typically, a run contained between 7 and 10 cycles, 8 being the prominent number. Each cycle consisted of a preparatory phase, the frequency ramp phase, and two flat tops.

6.2.1 Beam preparation

Once the vertically polarised deuteron beam, was injected into the COSY ring, it was accelerated to the starting momentum of 970 MeV, corresponding to a revolution frequency of $f_{\text{rev}} = 750\,602.6\,\text{Hz}$. To facilitate the scanning process without encountering phase-related issues, the beam was divided into four distinct equidistant bunches labelled B0, B1, B2, and B3. Subsequently, the electron cooler was turned on for 71 s and the beam was cooled to reduce the phase space, as discussed in Chapter 4. This cooling process leads to a decrease in the spread of transverse momentum. Figure 6.2 represents the experimental data showing the beam intensity as a function of time and the position along the COSY ring. The presence of four bunches is clearly visible. The position along the ring is represented in terms of the particle revolution phase. This is calculated based on the time delay of the detected event from the start time of the current turn n, $\phi_{\text{COSY}} \equiv (t_{ev} - t_n) f_{\text{rev}} \pmod{2\pi}$.

After the e-cooler was turned off, a series of subsequent steps were carried out in quick succession. This involved moving the carbon target such that the edge was at

Table 6.1: Timing for various COSY operations during the beam cycle for various run types

Operation in the cycle	Axion scans	WF scans	WF calibration
		Time (s)	
Injection	0.0	0.0	0.0
Acceleration on	0.153	0.153	0.153
Acceleration off	0.674	0.674	0.674
E-cooling on	4 – 75	4 – 75	4 – 75
Carbon target moved in	75	75	75
White noise extraction on	77	77	77
WASA flag (DAQ on)	78	78	78
RF solenoid on (rotate p_y)	83 – 86	83 – 86	–
RF Wien filter on	–	88	88
Quick ramp to start of scan	90.0 – 90.1	90.0 – 90.1	–
Constant frequency hold	90.1 – 120.1	90.1 – 120.1	–
Ramp to search for ALP	120.1 – 255.1	120.1 – 255.1	–
Constant frequency hold	255.1 – 285.1	255.1 – 285.1	–
RF Wien filter off	–	285	285
COSY RF stop	287	287	287
End of data taking	288	288	288

the centre of the detector, enabling the white noise to extract the beam onto the target, and activating the WASA DAQ. In Fig. 6.1, the count rates are plotted after 78 s, indicating that the DAQ was not switched on prior to that time. The last step in this stage involved using the RF solenoid for 3 s with the frequency of $f_{\text{sol}} = 629\,755.3\,\text{Hz}$ to flip the vertical polarisation to the horizontal plane.

Once the polarisation of each bunch was individually rotated to the horizontal plane, the bunches acquire a spin precession frequency, which can be calculated as the difference of f_{rev} and f_{sol}, $f_{\text{spin}} = 120\,847.3\,\text{Hz}$. In Fig. 6.3, the phases of each bunch's polarisation are shown as calculated at the detector. The analysis to obtain these individual bunch phases will be explained in Chapter 8 . Since the bunches arrive at the detector (located at a fixed point in the ring) one after the other, by the time bunch B3 arrives at the detector, the polarisation of previous bunches (B2, B1, and

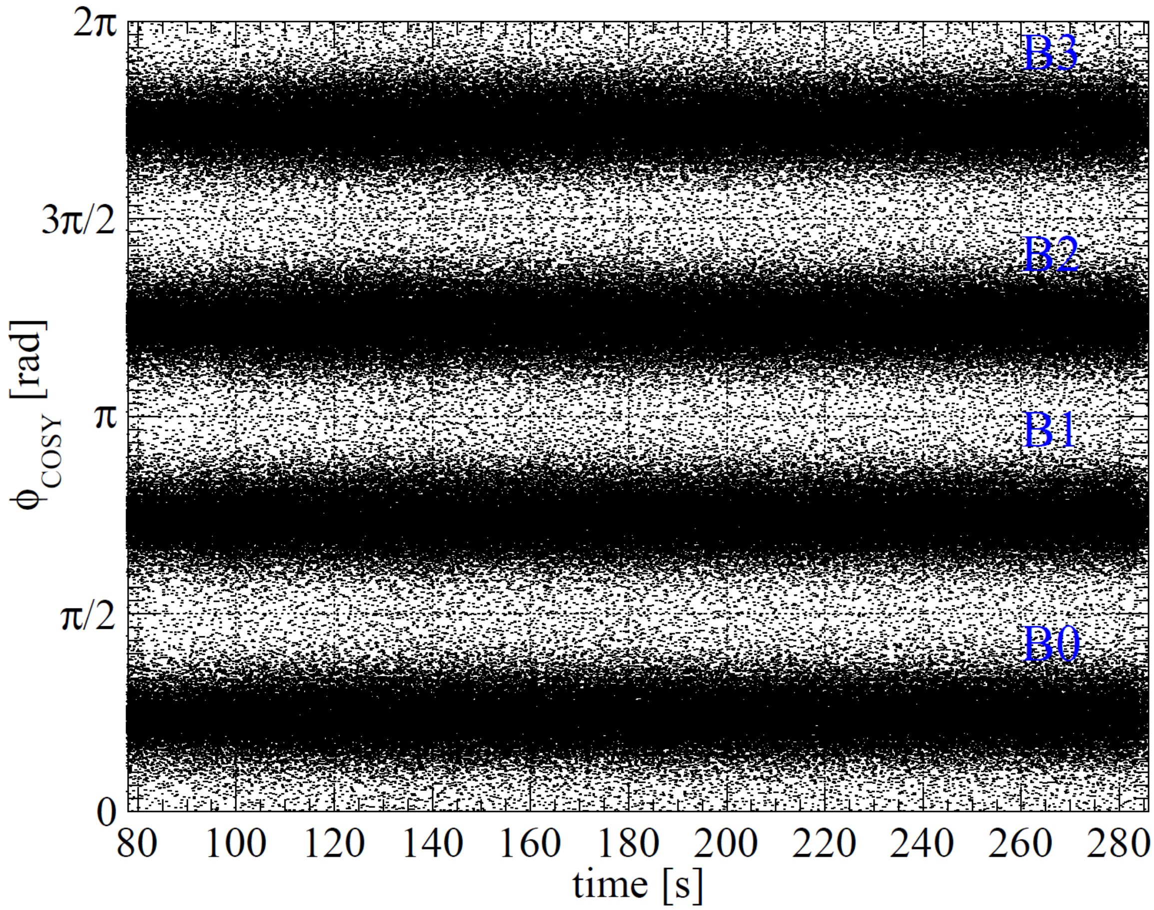

Figure 6.2: A two-dimensional plot showing the deuteron beam intensity along the COSY ring from $0 - 2\pi$ rad in the y axis and time in cycle in x axis. The density of points in the plot corresponds to the beam intensity, where darker regions indicate higher intensity. The separation of the beam into four bunches is clearly visible.

B0) would have recessed into the horizontal plane with the frequency f_{spin}. Hence, the values presented in Fig. 6.3 are not $\pi/2$ apart, as mentioned in Chapter 4. Model calculations (shown in Section 7.2) demonstrate that the phases marked in red, with values 1.32 rad, 1.32 rad, 1.32 rad and 2.32 rad, are equivalent to a phase difference of $\pi/2$ between the particles' polarisation at any given moment.

After the completion of the beam preparation stage, we are left with four bunches with reduced phase space and possessing long SCT, with individual polarisations rotated to the horizontal plane such that polarisations are perpendicular to each other in the particle rest frame. From the precise knowledge of the f_{rev} and f_{sol}, whose frequency

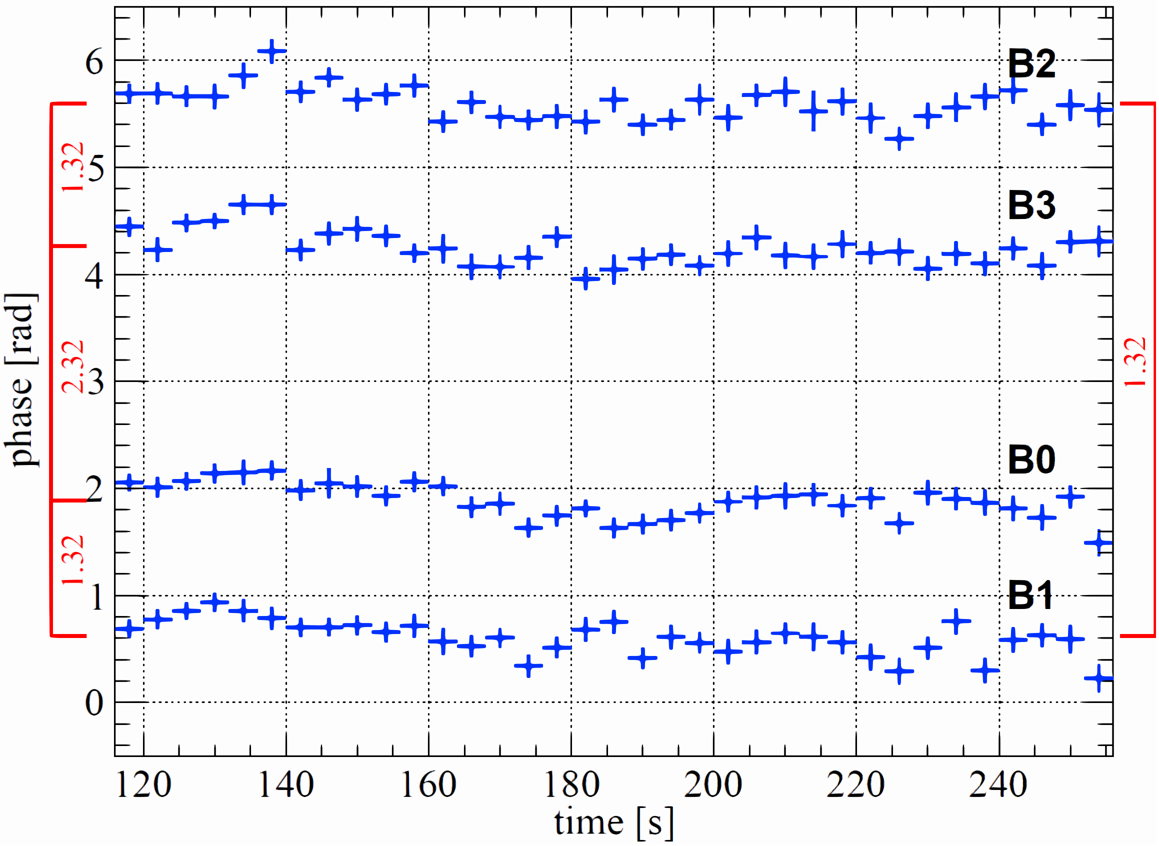

Figure 6.3: : The plot displays the phase calculated for each bunch based on the experimental data. The relative phase between the bunches is provided in red. These values match the values obtained from the model calculations of four bunches with polarisations $\pi/2$ apart at any given time, arriving at the detector (which is in a fixed space) at different times. Hence, confirming the actual polarisation distribution.

generators are stable up to several mHz, we can derive the kinematic parameters before the frequency ramps. The beam parameters are given in Table 6.2.

6.2.2 Frequency ramps for ALP scans

The next stage in the cycle was the frequency ramp, which is the key part of the experiment. The frequency scans were structured as given in Fig. 6.4, with each black line denoting a scan. After the polarisation was rotated to the horizontal plane (indicated by the red block in the figure), a quick initial ramp of 0.1 s duration was performed to reach the start frequency of the scan. This step had to be preceded by the rotation

Table 6.2: Beam parameters

Parameter	Symbol	Value
Revolution frequency	f_{rev}	750 602.6 Hz
Spin resonance frequency for solenoid	f_{sol}	629 755.3 Hz
Spin tune frequency	f_{spin}	120 847.3 Hz
Lorentz factor	γ	1.126
Beam velocity	β	$0.460\,c$
Momentum	p	970 MeV/c
Orbit circumference	l_{circ}	183.57 m
Number of deuterons per cycle (at start)	N_d	$\approx 10^9$

to the horizontal plane in order to avoid the time-consuming procedure of finding the RF solenoid resonance frequency f_{sol} for every set of scans anew. Finding the precise f_{sol} would take up more time than the scanning of a set of frequencies.

In each cycle, the frequency was linearly ramped for 135 s between the initial frequency $f_{\text{rev},0}$ and the final frequency $f_{\text{rev},f}$. Any expected jump in polarisation as a result of resonance crossing was expected to appear during the scan. To increase the statistics of a polarisation measurement before and after the scan, the ramp was sandwiched between two constant frequency blocks of $30 -$ s duration. The frequency of the preceding block was maintained at $f_{\text{rev},0}$, and the succeeding one at $f_{\text{rev},f}$.

Precautions were taken to prevent changes in the beam orbit during the momentum ramps. This was critical as even small changes to the orbit could significantly impact the SCT. Alongside the standard practise of minimising the RMS deviation of the orbit from the reference, the total deviation of all the BPM measurements from the reference orbit was also monitored, and the total deviation was maintained within 1 mm.

In the COSY ring, the ramps were performed by providing the value of momentum for each step of the scan, as the ramp control software only accepted momentum as

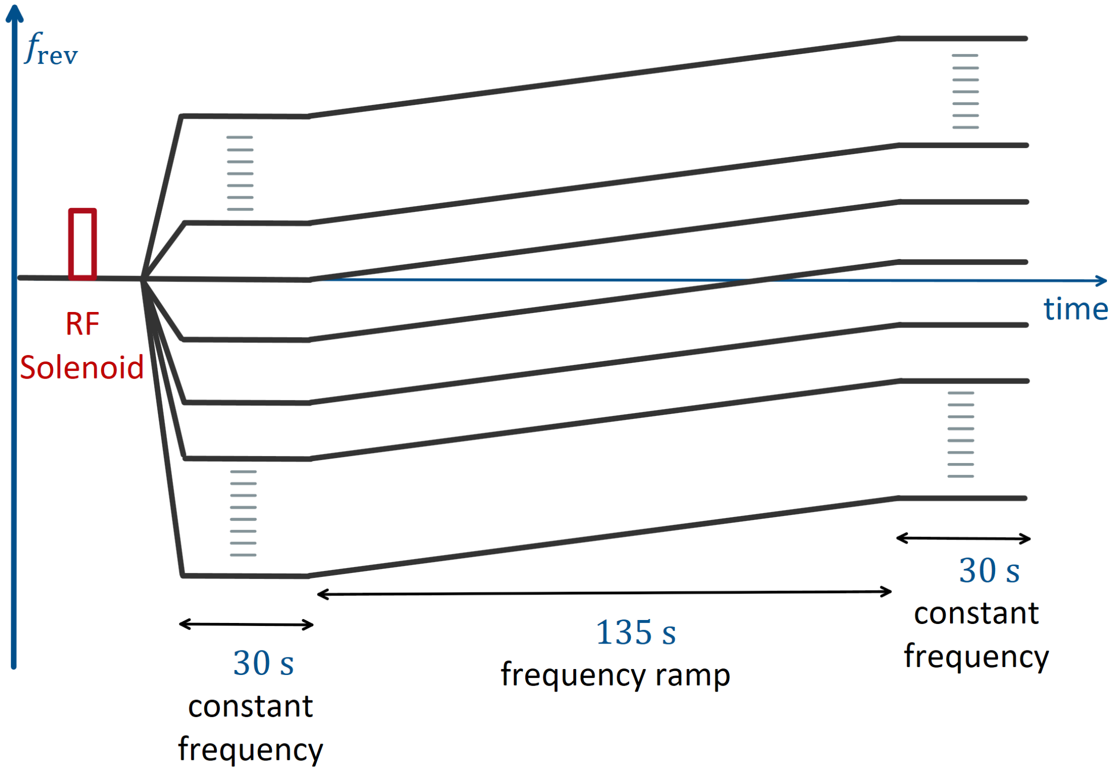

Figure 6.4: Figure representing the structure of scans (not to scale). The red block depicting the RF solenoid marks the completion of the beam preparation in a cycle. The black lines denote the revolution frequency of the beam through the cycle. The initial ramp, with high slope, shifts the frequency to the start of the scan. Each frequency scan, depicted by the low sloped parallel lines, was sandwiched between two flat regions with constant frequencies. The signal due to resonance was expected to appear during the frequency scan

input values. The initial and final momentum for each scan was calculated using,

$$p_0 = 970(1 + 1.173 \times 10^{-4} n)\ \mathrm{MeV}/c, \tag{6.2.1}$$

$$p_f = p_0 + \Delta p \tag{6.2.2}$$

Here n is the scan number and can be either positive or negative integer. The deuterons' momentum was moved away from 970 MeV/c —required p for RF solenoid operation— as given by Eq. (6.2.1). Δp is the total change in momentum over the 135 s of the duration of the scan. The Δp value was entered into the COSY control system. The experiment was performed at two different ramp rates given in Table 6.3. The corresponding rates for f_{spin} and f_{rev} are also given.

Table 6.3: Change in beam parameters during the ramp

Δp [MeV/c]	Δf_{rev} [Hz]	$\Delta \dot{f}_{\text{rev}}$ [Hz/s]	Δf_{spin} [Hz]	$\Delta \dot{f}_{\text{spin}}$ [Hz/s]
0.138	81.0	0.600	16.8	0.124
0.112	66.15	0.490	13.5	0.100

If the resonance is present at the beginning or end of the scan, it is possible that only part of the total resonance width is present within the scan range. As a result, the resonance width will only be partially covered, effectively diminishing the signal. To address this issue, it was initially planned to incorporate an overlap in the frequency ranges covered by the subsequent scans. For the faster ramps (top row Table 6.3), there was an overlap of 2.6 Hz in spin precession frequency. Unfortunately, for the slower scans (bottom row), an oversight during the experiment resulted in the start momentum being calculated with the same parameters as for the fast ramps. This resulted in the absence of desired overlap in slower scans.

The experiment consisted of 85 faster ramp scans with n varying from -42 to 42, and 18 slow ramp scans, with n ranging from -60 to -43. The list of runs, and their corresponding frequency ranges are given in Appendix A. Typically, each run consisted of 10 cycles, with every fifth cycle being unpolarised, to monitor the complete rotation of the polarisation into the horizontal plane. The outcome of the analysis from those remaining cycles were combined, and the process is explained in the analysis chapter. In total, there were 103 runs which covered a frequency range of 119.997 kHz - 121.457 kHz, corresponding to the axion mass range of 4.95 neV c^{-2} - 5.02 neV c^{-2}.

6.3 RF Wien filter tests

The RF Wien filter present in COSY provided us the opportunity to test the method that was used to search for axions. Despite the major differences in the effect of RF Wien filter and axions on deuteron spin, as mentioned previously (in Section 5.1.2), we could examine the ability of our machine to detect resonance crossing by observing vertical polarisation jumps caused by RF Wien filter. For this purpose, the RF Wien filter was operated in the EDM-mode, wherein the magnetic field was in the horizontal plane, resulting in the rotation of polarisation about the x axis.

Initial setup and calibration

The RF Wien filter was operated at the resonance frequency of $(1 - G\gamma)f_{\text{rev}}$. To account for slight variations that could occur in the experimental conditions, as in the case of RF solenoid, we must experimentally determine the resonance frequency. For this purpose, the RF Wien filter frequency was varied in small steps, similar to the procedure to find the resonance frequency of the RF solenoid. The procedure was done with the RF solenoid turned off and utilising the vertically polarised beam to induce oscillations in the polarisation. At each step, the amplitude and the frequency of the polarisation oscillation were calculated, and the of RF Wien filter the frequency corresponding to the maximum amplitude was selected as the resonance frequency. The resonance frequency of the RF Wien filter was found to be $f_{\text{WF}} = 871\,450.039(2)\,\text{Hz}$.

The calibration of the magnetic field strength of the RF Wien filter was done by observing the driven oscillations of the vertically polarised beam at different power settings of WF. These cycles followed the same initial steps as outlined in Table 6.1 up to the activation of the WASA DAQ at 78 s. In this case, however, instead of the RF solenoid the RF Wien filter was turned on at 88 s. The vertical polarisation, at resonance, experienced continuous driven oscillations until the RF Wien filter was turned off at 285 s.

We used four different power levels for the calibration of RF Wien filter: -18, -12, -6 and 0 dB of the maximum power. An in increase in power by 6 dB will increase the actual power by a factor of four. This in turn leads the amplitude of the magnetic field to increase by a factor two, since the power is proportional to the square of amplitude. Since the rotation of polarisation is proportional to the magnetic field strength (from T-BMT equation), we expect the frequency of the driven oscillations increase by a factor of two as the power setting is increased by 6 dB.

The corresponding left–right asymmetry A_{LR} data between 81 s - 287 s are shown in Fig. 6.5. A_{LR}, which is proportional to the vertical polarisation, is separated into 1-second time bins and is averaged for the four bunches. These driven oscillations can be reproduced using the function

$$A_{\mathrm{LR}}(t) = Ae^{-\frac{(t-t_0)}{\tau}} \cos\left(2\pi f_{\mathrm{drv}}(t-t_0)+\phi\right)+k, \tag{6.3.1}$$

where $A_{\mathrm{LR}}(t)$ describes the shape of the data, A is the amplitude, τ is the decay constant, f_{drv} is the driven oscillation frequency, ϕ is the phase, and k is the zero offset of the asymmetry data. The damping of the oscillations is due to the depolarisation of the beam over time. In an ideal case of infinite SCT, the decay constant would be $\tau = 0$. The driven oscillation frequency values obtained from fitting Eq. (6.3.1) to data from measurements at different RF Wien filter power settings are given in Table 6.4. The last column shows the ratio between the frequencies of the current row with the previous row and matches the expected value of two within a small percentage of deviation. The slight variation can be attributed to the properties of the control system of the RF Wien filter. The driven oscillation frequency f_{drv} of the WF serves as a measure of its strength and was utilised as an input parameter to simulations, as explained in the next chapter.

Table 6.4: Driven oscillation frequencies. The third column contains the ratio of the current row frequency to the one of the preceding row.

Power (dB)	Frequency (Hz)	Ratio
-18	0.013084(19)	
-12	0.026326(21)	2.0122(33)
-6	0.052816(25)	2.0062(19)
0	0.110848(345)	2.0988(66)

The RF Wien filter tests

After calibrating the strength of RF Wien filter, the experiment proceeded with the power level of RF Wien filter set to 0 dB. The structure of an RF Wien filter scan cycle was similar to that of an axion scan cycle given in Table 6.1, with the additional steps of switching the RF Wien filter on and off at 88 s and 285 s, respectively. We performed these scans with two different ramp rates, corresponding to the total momentum

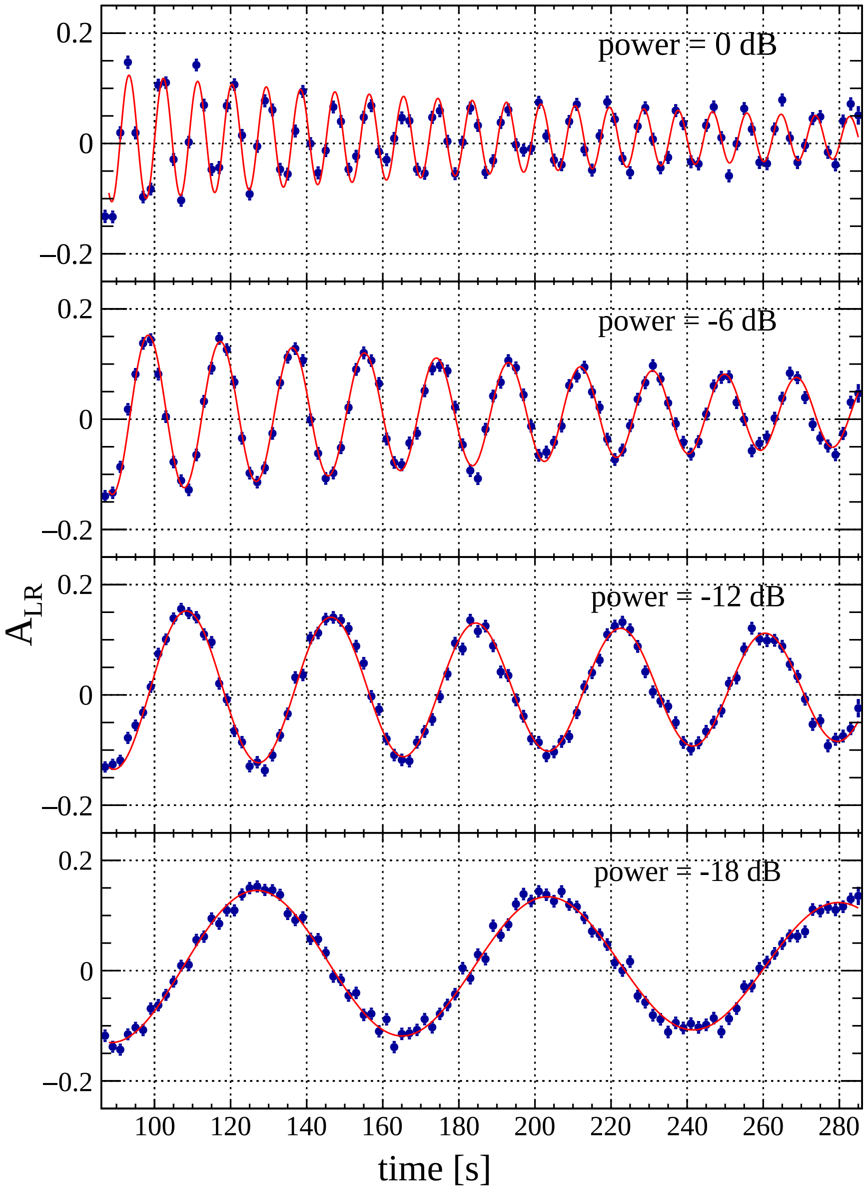

Figure 6.5: The plots show the measurements of the oscillating left-right asymmetry which is proportional to the vertical polarisation, generated by the continuous operation of the RF Wien filter at various power levels (noted in figure). The horizontal axis is the time in cycle. The RF Wien filter was on continuously from 88 s to 285 s. Data from all four bunches were combined to obtain a single asymmetry measurement.

change of 0.056 MeV/c and 0.112 MeV/c, in both positive and negative directions. In total, there were 12 runs, three for each combination of settings. The list of runs is given in Table A.2 of Appendix A.

The arbitrary phase between the in-plane polarisation and the RF Wien filter oscillations for each cycle results in random magnitude and the sign of the polarisation jump would. Additionally, these phases are also unknown and random from one measurement to the other. Thus, to extract the maximum possible jump, we rely on the fact that the measured jumps in fact sample a sinusoidal curve. The maximum possible jump relates to the strength of the WF. Further details will be given while explaining the simulations and data analysis.

7 Simulations

This chapter provides an overview of the simulations used to verify our assumptions, explain our experimental choices, and calibrate the experimental data, particularly the polarisation jump, with respect to physical phenomena such as the oscillating EDM and ALP. We employed the ”no-lattice” model, a simple spin tracking simulation, to confirm our assumptions about the IPP direction of the four bunches and calibrate the experiment’s sensitivity to signals from axions and RF Wien filter.

7.1 No-lattice model

Among the various spin tracking simulations available of varying degrees of complexity, the ”no-lattice” model[1] is one of the simpler spin tracking models, the basics of which are explained in [91, 97]. The no-lattice is a reference to the lack of explicit inclusion of any individual magnetic field element in the calculations. Instead, the spin tracking is achieved by effective rotation matrices. For example, in case of COSY there are 24 dipole magnets (12 in each of two arcs) in the ring, which bend the particle into a closed orbit. As the beam makes a single turn in the ring at constant frequency, the cumulative effect of these bending magnets on its polarisation can be summarised by a single rotation matrix about the y axis, perpendicular to the horizontal plane. In this model, the rotation due to bending magnets is considered to happen continuously around the whole ring. On the other hand, devices such as the RF solenoid and the

---

[1] The no-lattice model was first developed by E. J. Stephenson and has been modified by S.K. for the purposes of this thesis.

RF Wien filter, which operate at a single spot in the ring, are considered point-like or zero-width. The rotation due to these devices is applied sequentially to the dipole rotation for each turn. In the case of ramping frequency, each turn was divided into smaller slices and the dipole rotations were calculated multiple times to accommodate the changing frequency.

The no-lattice model follows the same co-moving reference frame as discussed in Chapter 3 for spin dynamics. The beam direction is along z axis, y axis is vertically upwards, and x axis is outwards on the ring plane. Now, consider a basic case with only MDM, and without EDM or scanning. The spin precession per turn about the y axis inside the dipole magnets is given by the rotation vector $\vec{\theta} = -2\pi G\gamma\hat{e_y}(= \theta\hat{e_y})$. Here, $G = -0.142\,987\,542\,4$ is the deuteron magnetic anomaly, and the relativistic factor $\gamma = 1.125\,975$ is calculated using the experimental frequency values $f_{\mathrm{sol}}/f_{\mathrm{rev}} - 1 = G\gamma$ for the nominal beam momentum of 970 MeV/c. The rotation of the deuteron IPP as it moves through the bending magnet can be described using the rotation of the polarisation vector $\vec{P}$ by,

$$\vec{P'} = \begin{bmatrix} \cos\theta & 0 & \sin\theta \\ 0 & 1 & 0 \\ -\sin\theta & 0 & \cos\theta \end{bmatrix} \vec{P}. \tag{7.1.1}$$

The polarisation direction after the rotation is given by $\vec{P'}$. Considering that in the case of ramping, the rotation angle θ depends on γ , the θ term was calculated incrementally within each turn. Rotation matrices can be written for all the different rotations the deuteron polarisation undergoes in the ring as given by the angular velocity equations in Section 3.3, to perform simulations.

7.2 Orientation of in-plane polarisation directions

In preceding chapters (4 to 6), it has been emphasised that using four bunches (labelled as Bi where $i = 1,\ 2,\ 3, 4$) in the storage ring enables us to be sensitive to all axion phases. To address the axion phase problem, simultaneous measurements with at least two mutually perpendicular polarisation beams are required. We chose to use four bunches to introduce redundancy and increase the sensitivity of the experiment.

This section explains how the use of four bunches and the RF solenoid leads to the desired orientation of the IPP directions using model calculations.

Let us consider four vertically polarised bunches in the ring, revolving at $f_{\mathrm{rev}} = 750\,602.5\,\mathrm{Hz}$. As each bunch passes through the RF solenoid, its polarisation gets a small kick and rotates by an angle ψ_{sol} every turn, in addition to the rotation in the horizontal plane given by Eq. (7.1.1). If the frequency of the RF solenoid is in resonance with the spin precession frequency, the cumulative effect of these rotations over multiple turns leads to driven oscillations of the polarisation about the z axis. In the experiment, we have chosen a $1 + G\gamma$ harmonic, corresponding to $f_{\mathrm{sol}} = 629\,755.3\,\mathrm{Hz}$.

The frequency of the vertical polarisation oscillation f_{drv} due to the solenoid serves as a measure of the strength of the solenoid $4\pi\epsilon_{\mathrm{sol}}$, where $\epsilon_{\mathrm{sol}} = f_{\mathrm{drv}}/f_{\mathrm{rev}}$. The rotation angle of the polarisation caused by this effect given by,

$$\psi_{\mathrm{sol}} = 4\pi\epsilon_{\mathrm{sol}} \cos\left[2\pi f_{\mathrm{sol}} t + \phi\right]. \tag{7.2.1}$$

Here, f_{sol} is the frequency of the solenoid, and the phase ϕ will be explained later. Additionally, ψ_{sol} can also be expressed in terms of turn number n. The accumulated rotation due to solenoid after n turns is expressed as,

$$\psi_{\mathrm{sol}} = 4\pi\epsilon_{\mathrm{sol}} \cos\left[2\pi(1 + G\gamma)n + \phi\right]. \tag{7.2.2}$$

The initial polarisation of the vertically polarised beam is given by $\vec{P} = \begin{bmatrix} 0 \\ 1 \\ 0 \end{bmatrix}$. After each turn in the ring, the polarisation undergoes the following rotation,

$$\vec{P'} = \begin{bmatrix} \cos\psi_{\mathrm{sol}} & -\sin\psi_{\mathrm{sol}} & 0 \\ \sin\psi_{\mathrm{sol}} & \cos\psi_{\mathrm{sol}} & 0 \\ 0 & 0 & 1 \end{bmatrix} \begin{bmatrix} \cos\theta & 0 & \sin\theta \\ 0 & 1 & 0 \\ -\sin\theta & 0 & \cos\theta \end{bmatrix} \vec{P}, \tag{7.2.3}$$

where $\vec{P'}$ is the polarisation after one turn in the ring. The rotation consists of two components: θ rotation about the y axis due to the MDM, and ψ_{sol} rotation about the z axis due to the RF solenoid. These rotations are treated separately, since the length of the RF solenoid is significantly shorter compared to the circumference of the ring. For each turn, the rotations given in Eq. (7.2.3) are performed based on the polarisation value from the previous turn. The θ rotation angle remains the same for every turn, whereas the rotation due to the RF solenoid accumulates every turn by $4\pi\epsilon_{\text{sol}}(\cos[2\pi n(1+G\gamma)])$.

To simulate the individual IPP direction, these calculations were repeated for every bunch. Each bunch arrives at the RF solenoid one after the other, with a time delay of $T_{\text{turn}}/4$ where $T_{\text{turn}} = 1/f_{\text{rev}}$ is the time for one turn in the ring. This time delay is denoted by the addition of the initial phase ϕ_{sol} to the solenoid rotation angle ψ_{sol}. This phase delay can be generalised as $\phi_{\text{sol}} = k\pi/2(1+G\gamma)$ where $k = 1,\ 2,\ 3, 4)$ is the bunch number.

The simulation involved numerical calculations to sum up all the rotations. In this model, the solenoid strength was set to $4\pi\epsilon_{\text{sol}} = 1.5708\times10^{-6}$, and the calculations were stopped when the vertical polarisation was almost zero, which occurred after 2×10^{6} turns in the simulations.

The orientation of the IPP can be expressed with the help of x and z polarisation components and is presented in Table 7.1. The second and third column give the polarisation component P_x and P_z for each bunch Bi after 2×10^{6} turns. The fourth column is the angle the polarisation makes with the z axis in the horizontal plane. It is calculated using the two-argument variant of the arctangent function applied to the values in the previous two columns.

Table 7.1: Model calculation of bunch polarisation directions as measured at a fixed point in the ring, e.g., at the polarimeter.

Bunch	P_x	P_z	Angle [rad]	Angle B(i-1)-B(i)
B0	-0.639562	0.768740	-0.693928	
B1	-0.904313	-0.426870	-2.011825	1.317897
B2	0.187022	-0.982356	-3.328722	1.317897
B3	0.997903	-0.064724	-4.647619	1.317897
B0 (again)				2.329493

The last column is the angle between the two adjacent bunches as measured when they arrive at a certain position, e.g., at the polarimeter. It is worth noting that this phase is different between B3 and B0, allowing us to identify the first bunch. We can compare this phase pattern with the experimental data obtained from the WASA polarimeter, as shown in Fig. 6.3. The experimental phase differences in Fig. 6.3 are shown in red colour, and the numbers match closely with the final column in Table 7.1. This demonstrates that the process of using the RF solenoid to rotate the polarisation into the horizontal plane matches with our model predictions.

Now let us consider a specific time, e.g., when bunch B3 is rotated into the horizontal plane. At this point, the bunches B2, B1, and B0 would have already been in the horizontal plane for $T_{\text{turn}}/4, T_{\text{turn}}/2,$ and $3T_{\text{turn}}/4$ s, respectively. These bunches would have experienced the rotation due to the MDM about the vertical axis, causing their polarisation to rotate by $\pi/4$, $\pi/2$, and $3\pi/4$. By applying these rotations to P_x and P_z from Table 7.1 we obtain the values in Table 7.2.

Table 7.2: Model calculation of bunch spin directions as measured at a fixed point in time, i.e., when the bunch B3 is completely rotated into the horizontal plane.

Bunch	P_x	P_z
B0	0.064724	0.997903
B1	-0.997903	0.064724
B2	-0.064724	-0.997903
B3 (no change)	0.997903	-0.064724

By utilising the P_x and P_z values from Table 7.2, we can evaluate the polarisation directions of each bunch, which are found to point in the $z, -x, -z,$ and x directions for the bunches B0-B3, respectively. In the rest frame of the bunches, each bunch exhibits a polarisation direction that is perpendicular to its neighbouring bunches. This configuration ensures that the particle rest frame electric field $\vec{E}^*$ and the polarisation of the adjacent bunches are oriented parallel or perpendicular to each other. Additionally, the electric field and polarisation of opposite bunches are pointing 180° apart. Figure 7.1 illustrates the orientation of the polarisation with respect to the particle rest frame electric field from a top-down perspective. Because the EDM is always aligned with the particle's spin, the former inherits the latter's relative direction with respect to the electric field. The torque exerted by the $\vec{E}^*$ on the EDM is maximum when the $\vec{E}^*$ and EDM are perpendicular to each other. As a result, this arrangement of polarisation ensures that the experiment can detect changes in vertical polarisation for all phases of axions. This prevents the possibility of missing any axions due to phase mismatch, effectively removing the dependence of the axion phase on the measurement.

Another advantage of this polarisation orientation pattern of the four bunches is its ability to mitigate systematic errors arising from the polarimeter. The presence of opposite signs of polarisation between the opposite bunches effectively eliminates any inherent offset in the polarisation measurement within the polarimeter.

The calculations presented here assume a circular ring and the beam moving in the clockwise direction while looking from above. However, the COSY ring has a racetrack shape comprising two arcs and two straight sections of equal length. Consequently, at any given time, two bunches will be located in the opposite arcs with rotating polarisation, while the polarisation of the other two bunches in the straight sections will remain stationary. As a result, rather than a smooth rotation in the horizontal plane, the polarisation follows a rotate, no-rotate, rotate, no-rotate pattern akin to a zigzag. As the bunches traverse their respective quarters in their rest frame, the polarisation of the bunches in the arc will rotate by half the spin precession rotation angle, $\theta/2 \approx 28.8°$. This leads to an oscillation of the angle between the subsequent bunches' polarisation, ranging between 90° and 61.2°, instead of a constant 90°. Hence, while calculating the sensitivity, we calculate the average of the cosine function between the extreme of the deviations from 90, i.e., between 0° and 28.8°. This causes the signal to be reduced by $\kappa = 4.2\%$. The results of this experiment are corrected to account for this effect.

7.3 Sensitivity calibration for axion scans

The ALP signal manifests as a vertical polarisation change when the spin precession frequency crosses its resonance with either the axion-induced EDM oscillation frequency or due to axion wind. A calibration is required to convert the asymmetry values registered by the polarimeter into the EDM strength and further into other axion coupling constants. Equation (7.1.1) provides the rotation of the horizontal polarisation due to the deuteron magnetic anomaly, where θ represents the rotation angle. In order to calculate the effect of EDM, an additional continuous rotation,

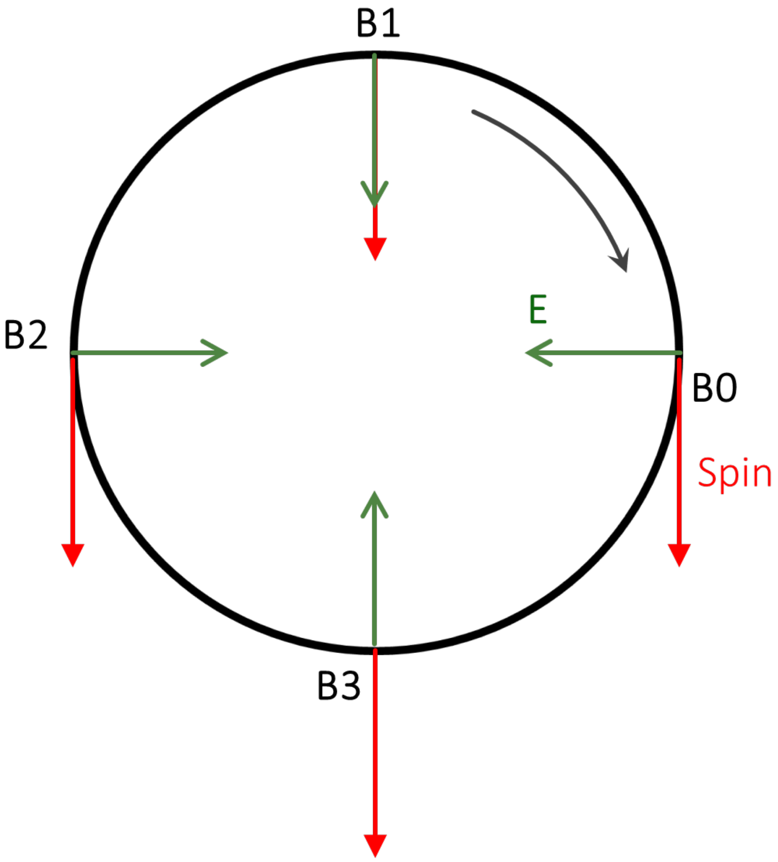

Figure 7.1: Top-down illustration showing four bunches in the ring at a fixed time, direction of individual particle rest frame electric field, and individual spin directions. The spin directions are drawn as calculated in Table 7.2.

denoted by,

$$\vec{\psi} = 2\pi \frac{\vec{\Omega}_{\text{EDM}}}{|\vec{\Omega}_{\text{rev}}|} = \psi \hat{e_x},$$

was introduced in the no-lattice model. Since both these rotations are continuous, we have to combine these rotations instead of individual rotation matrices, as was the case with the RF solenoid (shown in Section 7.2) or the RF Wien filter (Section 7.4). The resultant rotation will be about the axis represented by the rotation vector,

$$\vec{\chi} = \vec{\theta} + \vec{\psi}. \tag{7.3.1}$$

Figure 7.2, with the help of co-moving coordinate system, provides a visual representation of these rotation vectors. The effect of EDM had to be exaggerated to be visible. The angle between the resultant vector $\vec{\chi}$ and $\vec{\theta}$ is given by

$$\xi = \arctan\left(\frac{\psi}{\theta}\right). \tag{7.3.2}$$

To perform a combined MDM and EDM rotation, the reference frame must first be tilted by an angle ξ about the z axis. A single turn around the ring can be represented using the following rotation.

$$\vec{P}' = \begin{bmatrix} \cos\xi & -\sin\xi & 0 \\ \sin\xi & \cos\xi & 0 \\ 0 & 0 & 1 \end{bmatrix} \begin{bmatrix} \cos\chi & 0 & \sin\chi \\ 0 & 1 & 0 \\ -\sin\chi & 0 & \cos\chi \end{bmatrix} \begin{bmatrix} \cos\xi & \sin\xi & 0 \\ -\sin\xi & \cos\xi & 0 \\ 0 & 0 & 1 \end{bmatrix} \vec{P}. \tag{7.3.3}$$

Here, $\vec{P}$ represents the initial polarisation and $\vec{P}'$ the polarisation after one complete rotation. The first and third square matrices account for the coordinate system transformation, while the middle matrix represents the primary rotation.

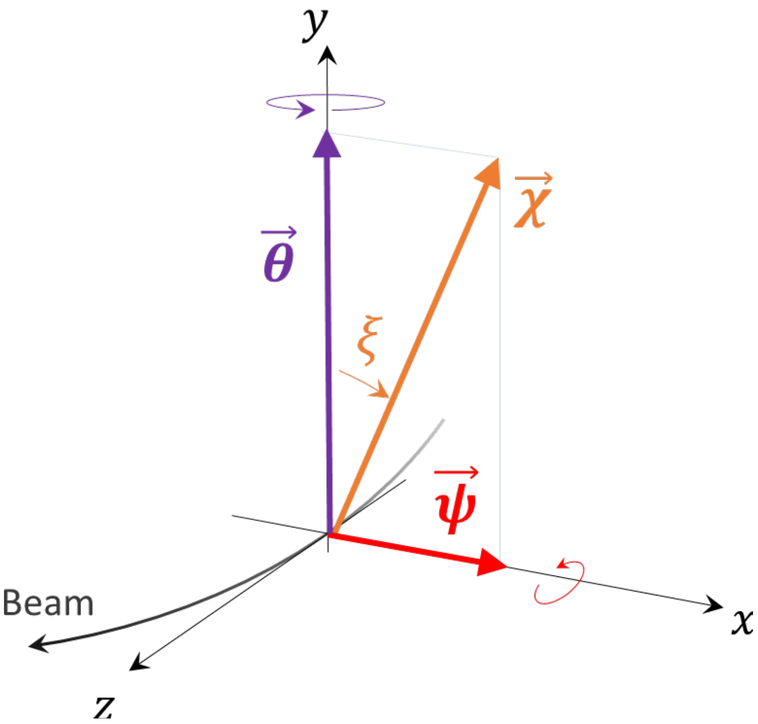

Figure 7.2: The co-moving particle reference frame with the various rotation vectors indicated. The rotation due to the MDM is denoted by $\vec{\theta}$ and is by and large the biggest rotation. $\vec{\chi}$ is the total rotation due to MDM and EDM (denoted by $\vec{\psi}$). The angle ξ between $\vec{\theta}$ and $\vec{\chi}$ is the angle through which the frame of reference is rotated to accommodate continuous rotations due to EDM and MDM (see text). The size of $\vec{\psi}$ is exaggerated to make it visible in the diagram.

In order to detect resonance in the presence of an axion, in the experiment the spin precession frequency (f_{spin}) was ramped up. As mentioned before, to account for the resulting variation in γ over a single turn, the rotation in Eq. (7.3.3) was split into $J = 15$ steps (slices), with the rotation angle θ reduced by the factor J for each slice. The number of slices was chosen such that calculations converged with a precision of 0.01%. The simulations were centred at the nominal revolution frequency of the deuteron, f_{rev}=750 602.6 Hz, and the applied ramp rate was $\dot{f}_{\text{rev}} = 1\,\text{Hz/s}$ over a total scanning range of 100 Hz.

Throughout the scan, the circumference of the orbit remained constant. For each of the J rotations, the revolution frequency and the Lorentz factor γ were calculated. If $j = 1, ..., J$ is the repetition number, then for the j^{th} iteration in the n^{th} turn, the time and the revolution frequency is calculated as follows,

$$t = \frac{n + j/J}{f_{\text{rev},j-1}} ,$$

$$f_{\text{rev},j} = f_{\text{rev},j-1} + t \times \dot{f}_{\text{rev}} ,$$

where, $f_{\text{rev},j-1}$ is the revolution frequency at the end of the previous iteration. The Lorentz factor for the j^{th} iteration can be calculated as,

$$\gamma_j = \left[1 - \left(\frac{f_{\text{rev},j}\ l_{\text{circ}}}{c}\right)^2\right]^{-\frac{1}{2}} .$$

Here, l_{circ} represents the orbit circumference and c is the velocity of light. Finally, the rotation angle θ for the j^{th} iteration is calculated as

$$\theta_j = -\frac{2\pi G\gamma_j}{J}. \tag{7.3.4}$$

The total rotation angle due to EDM, ψ is given by,

$$\psi = \psi_{\text{AC}} \cos\left[2\pi f_{\text{osc}}(t - t_0) + \phi_a(t_0)\right], \tag{7.3.5}$$

where, ψ_{AC} is the amplitude of the oscillating EDM rotation, f_{osc} is the axion-induced oscillation frequency, and t_0 is the start time of the calculation. The θ_j and ψ from Eqs. (7.3.4) and (7.3.5) are used to calculate the resultant rotation vector χ in Eq. (7.3.1) and then fed in to the rotation matrix Eq. (7.3.3). The vertical polarisation change as the resonance is crossed can vary between positive and negative limits depending on the initial phase. The maximum jump can be calculated by adding in quadrature the polarisation jumps from the simulations at two orthogonal phases, namely $\phi_a(t_0) = 0$ and $\pi/2$.

The simulation was repeated with different EDM strengths, using a f_{rev} scan rate of 1 Hz/s, and the resulting polarisation jumps are shown in Fig. 7.3a, with oscillating EDM strength on the x axis. We observe a linear dependence that is valid for

$\Delta P_y << 1$, where one is the maximum possible polarisation jump, However, as the curve approaches the peak, it deviates from linearity, and for larger values of ψ_{AC}, the curve rolls over. Since all of our experimental values are close to zero, we focus on the linear region for calibration. Figure 7.3b shows the plot zoomed into this region, where the ΔP_y are closer to zero, and the polarisation jumps show a linear behaviour. This range of polarisation values corresponds to the expected amplitudes in the experiment.

Furthermore, some data points were repeated at different scan rates, revealing that in the linear region, the polarisation jump scales with the reciprocal of the square root of the scan rate. This relationship will assist in using the calibration curve in Fig. 7.3b to calibrate the polarisation jumps obtained from experiments conducted at different ramp rates $\dot{f}_{\mathrm{rev}} = 0.6\,\mathrm{Hz/s}$ and $0.49\,\mathrm{Hz/s}$ (fast and slow scans), given in Table 6.3.

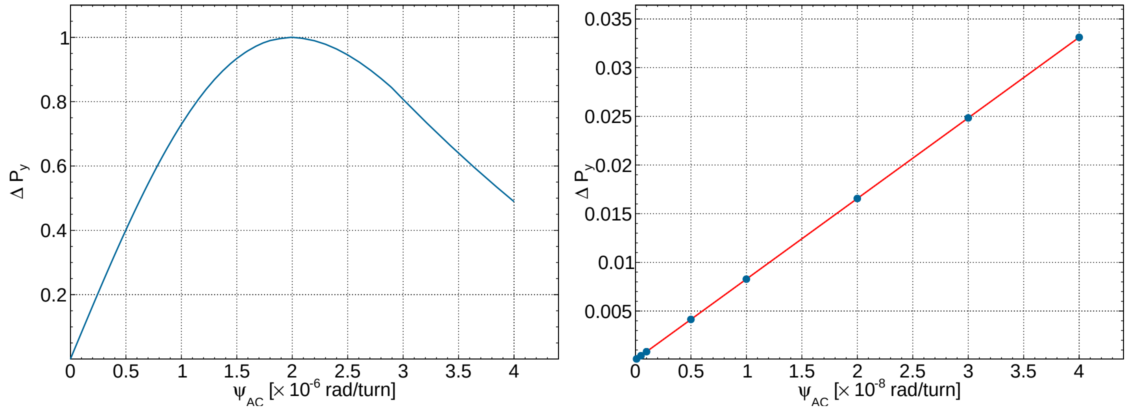

(a) (b)

Figure 7.3: (7.3a) Simulated polarisation jump amplitude as a function of the EDM strength ψ_{AC}. These simulations are suitable for calibration, primarily in the lower left region of the graph. (7.3b) A zoomed-in view of the linear part of the simulated calibration. Please note the different ranges of the axes. The blue points in the plot represent the simulated data, while the red line represents the linear fit. This is utilised to calibrate the polarisation jumps observed in the experiment.

An example with typical values used in the calculation can help illustrate the process. For this purpose, we chose an oscillating EDM strength of $\psi_{\mathrm{AC}} = 8\times10^{-9}\,\mathrm{rad/turn}$ and a scan rate of $\dot{f}_{\mathrm{rev}} = 1\,\mathrm{Hz/s}$.

Using simulations from two orthogonal phases, the maximum jump was calculated as $\Delta P_y = 0.0066$ (see, Fig. 7.3b, normalized to a beam polarisation of one. To scale the ratio of EDM strength to polarisation to the experimental ramp rates, we introduce a scaling factor $k = \sqrt{\dot{f}_{\text{rev}|\text{exp}}/\dot{f}_{\text{rev}|\text{calib.}}} = 0.775$ for the faster scan rate and $k = 0.700$ for the slower scan rate. Using these factors, the relationship between ψ_{AC} and ΔP_y for the fast and slow scans is calculated to be 9.40×10^{-7} rad/turn and 8.48×10^{-7} rad/turn, respectively.

A jump in vertical polarisation is the expected signal for the resonant search of axions in the storage ring. The calibration described in this section aims to connect this observable to the physical quantity. In Chapter 3, the rotation of the spin due to oscillating EDM and axion-wind was given by the equation Eq. (3.3.10). For now, let us ignore the axion-wind term (will be explained at the end of the section), and assume that the effect of axion is solely the induction of oscillations in the EDM which leads to the rotation of spin. The oscillating EDM can be expressed as,

$$d_{\text{osc}}(t) = d_{\text{AC}} \cos[2\pi f_{\text{osc}}(t - t_0) + \phi_a(t_0)], \tag{7.3.6}$$

where, d_{AC} is the strength of the oscillating EDM. From Eq. (3.3.10b), the rotation due to d_{osc} can be written as,

$$\vec{\Omega}_{\text{AC}} = -\frac{1}{S\hbar}\frac{d_{\text{AC}}}{a_0} a(t) c\vec{\beta} \times \vec{B} \tag{7.3.7}$$

In this expression, S —which equals one for a deuteron—represents the spin and $a = a_0 \cos[\omega_a(t - t_0) + \phi_a(t_0)]$ is the axion field with an amplitude of a_0. Using the relation between angular revolution velocity and magnetic field Eq. (3.3.9) $\vec{B} = (-m_a\gamma/q)\vec{\Omega}_{\text{rev}}$, Eq. (7.3.7) can be modified as,

$$\vec{\Omega}_{\text{AC}} = d_{\text{AC}}\frac{c\gamma m}{q\hbar} \cos\left[\omega_a(t - t_0) \;\; + \phi_a(t_0)\right]\vec{\beta} \times \vec{\Omega}_{\text{rev}}. \tag{7.3.8}$$

In terms of amplitude of oscillating EDM rotation amplitude $\psi_{\text{AC}} = 2\pi\vec{\Omega}_{\text{AC}}/\left|\vec{\Omega}_{\text{rev}}\right|$, we can calculate the amplitude of the oscillating EDM as,

$$|d_{\text{AC}}| = \frac{1}{2\pi}\;\frac{\hbar q}{\beta\gamma m_a c}\;\frac{k}{1-\kappa}\;\psi_{\text{AC}}. \tag{7.3.9}$$

Here, $k = \sqrt{\dot{f}_{\text{rev}|\text{exp}}/\dot{f}_{\text{rev}|\text{calib.}}}$ is the scaling factor between different ramp rates and $1 - \kappa = 0.958$ is the correction factor which accounts for the assumption of a circular ring instead of a ring with alternating straight and curved sections, as present in COSY. To simplify the connection with the COSY parameters, the factor $q/(\beta\gamma m_a c) = q/p$ can be replaced with the magnetic rigidity of the ring $B\rho$. The amplitude of oscillating EDM, in the usual EDM units of $e\,$cm, and in terms of the previously mentioned ratio of ψ and ΔP_y, can be expressed as,

$$|d_{\mathrm{AC}}| = \frac{1}{2\pi}\,\frac{\hbar}{B\rho}\,\frac{k}{1-\kappa}\left|\frac{\psi_{\mathrm{AC}}}{\Delta P_y}\right|_{\mathrm{calib.}} A\ . \tag{7.3.10}$$

Here, A is the true value of the maximum jump size obtained from the experiment, the details on how it was obtained will be explained in the next chapter. The second fraction evaluates to $\hbar/B\rho = 3.26{\times}10^{-35}\,\mathrm{Js/Tm} = 2.03{\times}10^{-14}\,e\,\mathrm{cm}$, and the rest of the expression is dimensionless. Except for A, all the coefficients on the right-hand side can be combined into a single parameter λ, whose value is 316 for fast scans and 286 for slow scans. This provides a straightforward way to connect the experimental data to oscillating EDM. For the typically observed experimental values of A, the value of d_{AC} falls below $10^{-22}\,e\,$cm.

The calculations conducted thus far have primarily focused on the polarisation rotation around the longitudinal axis resulting from the resonance between f_{spin} and oscillating EDM. It is also assumed that the vertical polarisation signal can be entirely attributed to the oscillating EDM. However, it is worth noting that the resonance-induced polarisation rotation can also be caused by the axion-wind effect, which causes a rotation of polarisation along the radial axis. Experimentally, it is not possible to distinguish between these two rotations, occurring around perpendicular axes, as both result in a shift in vertical polarisation when the resonance condition is met. These rotations have a phase difference of $\pi/2$, allowing for their amplitudes to be coherently combined.

Assuming solely the axion-wind effect, the only change to the calculation is to replace the matrix for rotation about the z axis with the matrix for rotation about the x axis. The same calculations have been repeated for radial rotations, yielding results comparable to those discussed here.

7.4 Calibration of polarisation jumps for RF Wien filter

In this section, we describe simulations of the RF Wien filter that are built upon the previous sections in this chapter. The simulations aim to establish confidence in simulations of the axion scan sensitivity by comparing the results obtained from RF Wien filter experiments with those obtained from the simulations.

Contrary to ALPS, the RF Wien filter does not have a continuous effect on the beam particles, the length of which considerably smaller than the ring. Thus, we can consider the rotations due to RF Wien filter (ψ_{WF}) and MDM (θ) separately. Since the simulations for WF calibration involve frequency ramps, the rotations were calculated for each $1/J^{\mathrm{th}}$ slice of the full turn, as explained in Section 7.3.

The RF Wien filter generates rotation of the polarisation about the radial axis and creates driven oscillations when the f_{WF} is in resonance with f_{spin}. An example of the driven oscillations from the experiment was shown in Fig. 6.5. From Table 6.4, we can determine the driven oscillation frequency and calculate the strength of the RF Wien filter $4\pi\epsilon_{\mathrm{WF}}$, where $\epsilon_{\mathrm{WF}} = f_{\mathrm{drv|WF}}/f_{\mathrm{rev}}$. For a power of 0 dB, inserting the value of driven oscillation frequency taken from Table 6.4, we obtain

$$\epsilon_{\mathrm{WF}} = \frac{f_{\mathrm{drv|WF}}}{f_{\mathrm{rev}}} = \frac{0.110848}{750602.6} = 1.4768\times10^{-7} \,. \tag{7.4.1}$$

The total rotation of the polarisation due to WF is given by

$$\psi_{\mathrm{WF}} = 4\pi\epsilon_{\mathrm{WF}} \cos\left[2\pi f_{\mathrm{WF}}(t-t_0) + \phi_{\mathrm{WF}}\right] , \tag{7.4.2}$$

where ϕ_{WF} is the RF Wien filter phase with polarisation rotation, and f_{WF} is the WF frequency, which is set at $(1 - G\gamma)$ harmonic.

To enable proper comparison with experiments, the simulations were conducted at two different ramp speeds, $\dot{f}_{\mathrm{rev}} = 0.49$ Hz/s and 0.24 Hz/s, which match the experimental rates. Each set of simulations was repeated 100 times, with different phases between 0 and 2π. Since the experimental phases are random and unknown, covering the whole phase space helps to compare with experimental results. The ramps are structured similarly to the previous section but centred at the $f_{\mathrm{WF}} = 871\,450.039\,\mathrm{Hz}$. The rotation matrix is given by

$$\vec{P'} = \begin{bmatrix} 1 & 0 & 0 \\ 0 & \cos\psi_{\mathrm{WF}} & -\sin\psi_{\mathrm{WF}} \\ 0 & \sin\psi_{\mathrm{WF}} & \cos\psi_{\mathrm{WF}} \end{bmatrix} \begin{bmatrix} \cos\theta_j & 0 & \sin\theta_j \\ 0 & 1 & 0 \\ -\sin\theta_j & 0 & \cos\theta_j \end{bmatrix} \vec{P}\,, \tag{7.4.3}$$

where, θ_j is the polarisation rotation for j^{th} slice of the turn. The jump values obtained from the simulation are presented as a function of phase ϕ_{WF} in Fig. 7.4. The sinusoidal fit yields maximum jump values of 0.75 and 0.93 for the two ramp rates 0.49 Hz/s and 0.24 Hz/s, respectively, under the assumption that polarisation is normalised to one. It should be noted that these values do not match the scaling factor for ramp rates mentioned in the previous section. since the WF jumps are large and thus beyond the region where the linear calibration (scaling) was valid.

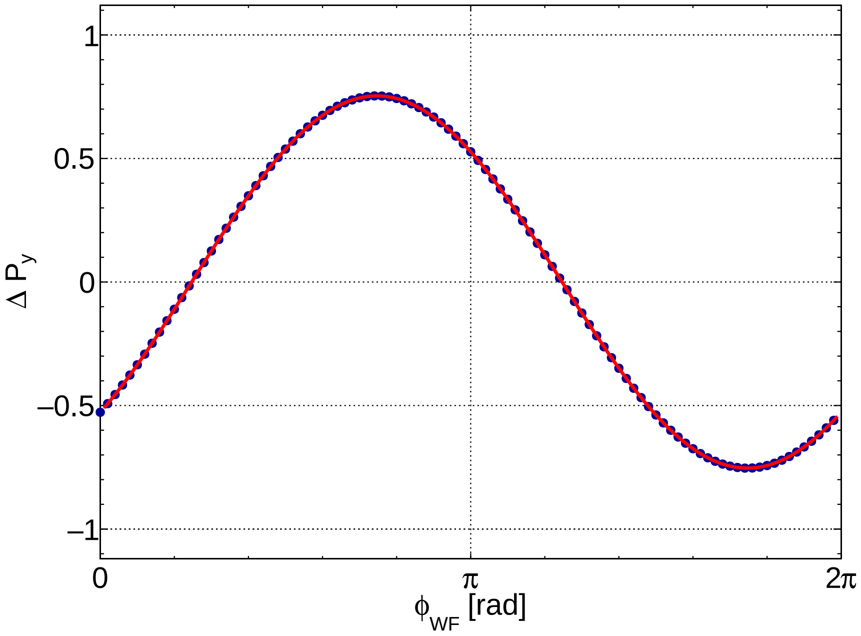

(a) Simulation for $\dot{f}_{\text{rev}} = 0.49\,\text{Hz/s}$. The corresponding amplitude is 0.75.

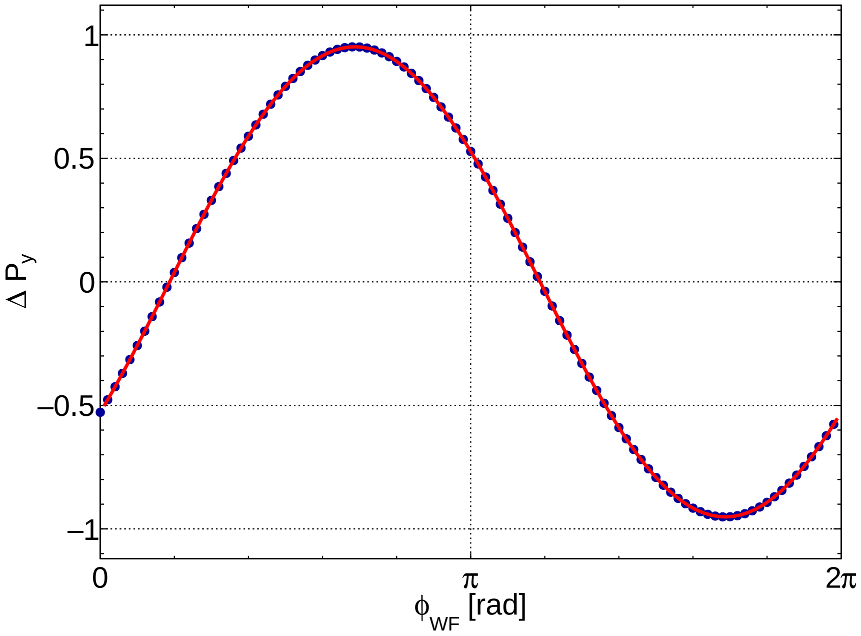

(b) Simulation for $\dot{f}_{\text{rev}} = 0.24\,\text{Hz/s}$. The corresponding amplitude is 0.93.

Figure 7.4: Simulation results for different values of the phase ϕ_{WF} and the corresponding polarisation jumps at two different ramp rates mentioned in the respective captions. The red line represents a sinusoidal fit to the data, which gives a maximum jump value.

8 Data analysis

The primary objective of this work was to analyse the polarisation data from the described experiment, and search for a polarisation jump, which can be related to the oscillating EDM or axion-wind, and consequently to various axion couplings. The first step in achieving this was to convert the raw detector data into a tree structure provided by the ROOT software framework developed at CERN. ROOT is a freely available software framework under the LGPL/GPL licence, and documentation is available at [98].

Subsequently, the tree structure was analysed to generate various histogram plots which can be further analysed. This semi-raw experimental data is available in the Jülich DATA repository [99]. A software programme was developed by the author, building upon the previous versions available in the collaboration. This programme is capable of calculating the in-plane polarisation asymmetry A_{IP} while considering the scanning of frequency and computing polarisation jumps from the vertical asymmetry A_{LR} data.

The second part of the analysis aimed to eliminate the systematics from the jump values by building on the foundation of the Feldman-Cousins method [100].

8.1 Calculation of In-plane polarisation

This section will focus on the method to extract IP asymmetry information from the WASA detector data, as described in Refs. [85, 101, 102].

The deuteron beam polarisation in the horizontal plane has a precession frequency of about 121 kHz, and at a typical detector rate of $\approx 4000\,\mathrm{s}^{-1}$ (see Fig. 6.1), only one event per 30 spin oscillations was registered. Therefore, we must unfold the down-up asymmetry A_{DU}, as described below, and map the events in a time bin into a single spin precession period. An example of this mapping is shown in Fig. 8.1. The data was sorted into 2 s time bins and each of such data subsets was analysed independently. After choosing a central value of spin tune $\nu = |G\gamma|$, the advance in the polarisation angle α at each time bin was calculated using the equation,

$$\alpha = \omega t = 2\pi\nu f_{\mathrm{rev}}(t - t_0)\ , \tag{8.1.1}$$

where t was the time measured from the start of the time bin t_0, and the spin tune ν and the revolution frequency f_{rev} were assumed to be constant.

Next, the events in each time bin were distributed into 12 angular bins, ranging from 0 rad to 2π rad, based on α modulo 2π. For each angular bin, the down-up asymmetry A_{DU} was calculated. A sinusoidal curve was fit to A_{DU} and the amplitude of this curve provided the value of the in-plane polarisation asymmetry A_{IP}. Examples of these angular distributions and their sine fits are shown in Fig. 8.1. The phase of the sine curve ϕ_ν indicated how well the spin tune value we assumed matches the actual value. If ϕ_ν remains relatively constant as a function of time, it was a considered good estimate of spin-tune value. Large phase variations indicate that the spin-tune value

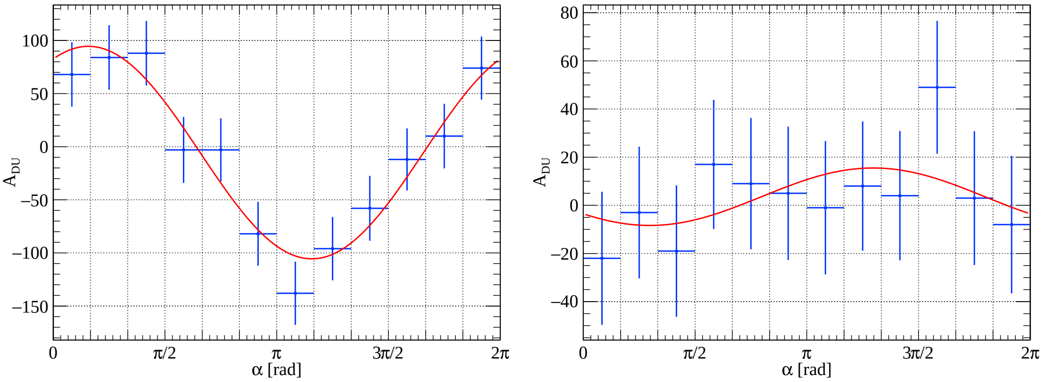

(a) Large IPP. (b) Small IPP.

Figure 8.1: Plot of Down-Up asymmetry data as a function of the horizontal directional bins for a single time bin. The red curve is the sinusoidal fit whose amplitude gives the magnitude of IPP.

needs to be adjusted. This was done based on the slope of the phase curve until the phase variations disappeared. An illustration of phase histories corresponding to a correct and incorrect spin tune ansatz are shown in the Fig. 8.2.

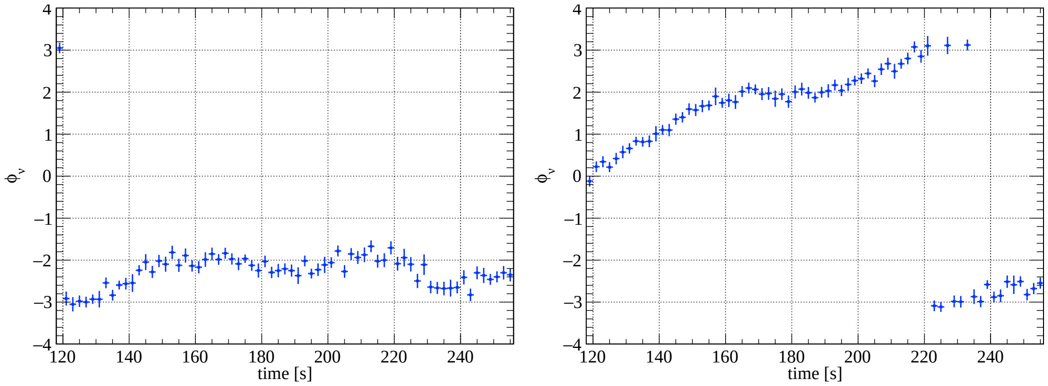

Figure 8.2: Example plots of ϕ_ν as a function of time. This phase was calculated from the sinusoidal fit to the A_{DU} of each time bin. A good estimate of spin tune results in a phase history with small variation (left). Sloped phase histories (right) indicate that the assumed spin tune does not match the real value and needs to be adjusted.

In-plane polarisation in case of a scan

During a scan, the momentum was linearly increased between two time points t_1 and t_2. This led to an increase of both the spin tune and revolution frequency. The angular velocity in this case can be calculated as,

$$\omega(t) = \begin{cases} 2\pi\nu_0 f_{\mathrm{rev},0} & \text{for } t_0 < t < t_1, \\ 2\pi[\nu_0 + \dot{\nu}(t - t_1)][f_{\mathrm{rev},0} + \dot{f}_{\mathrm{rev}}(t - t_1)] & \text{for } t_1 < t < t_2, \\ 2\pi\nu_f f_{\mathrm{rev},f} & \text{for } t > t_2, \end{cases} \tag{8.1.2}$$

and the polarisation angle can be obtained by integrating $\omega(t)$ over time,

$$\alpha(t) = \int_{t_0}^{t} \omega(t')\ \mathrm{d}t' . \tag{8.1.3}$$

Here, the subscripts 0 and f correspond to the initial and final values, respectively, and the dotted symbols denote time derivatives. Once $\alpha(t)$ was determined, the calculation of the in-plane polarisation asymmetry A_{IP} follows the same steps as in the constant frequency case.

The A_{IP} was utilised in the analysis in two cases. Firstly, to calculate the SCT of the beam. Secondly, to normalise the jumps obtained from the analysis of the A_{LR} data. This renormalisation step aided in the comparison of the experimental results with the simulations.

8.1.1 Spin coherence time

An example of the IP asymmetry A_{IP} derived from the analysis described earlier is shown in Fig. 8.3. The spin coherence time of the beam, which represents the time required for the polarisation to decrease to half its initial value, can be calculated from the A_{IP} plot. As highlighted in Chapter 4 while discussing the experimental prerequisites, it was essential to calculate SCT for understanding the polarisation characteristics of the beam, and it also served as a check of the measurement quality. To obtain SCT of the beam, the A_{IP} data was fit with a straight line, the fit result is shown with the red line in Fig. 8.3. The SCT from the fit function was calculated using the slope Λ and the intercept A_{IP0},

$$\tau_{\mathsf{sct}} = -\frac{A_{\mathrm{IP0}}}{2\Lambda}, \tag{8.1.4}$$

where, A_{IP0} is the initial IP asymmetry soon after the spin flip using solenoid. The slope of the fit Λ is always negative, denoting the decrease in polarisation with time and the SCT calculated as the time for the initial asymmetry to fall to half of the initial value; in this example $\tau_{\mathsf{sct}} = 630(190)\,\mathrm{s}$.

8.2 In search of vertical polarisation jump

In the experiment, polarisation data were registered, and the expected signal of axion, which is a change in vertical polarisation away from zero, would be observed in the left-right asymmetry A_{LR} data. During the analysis, these asymmetries were calculated in 2 s time bins, and at this level of binning, any jump related to the resonance would be seen as instantaneous. The left-right asymmetry $A_{\mathrm{LR}}(t)$ for a time bin t is described

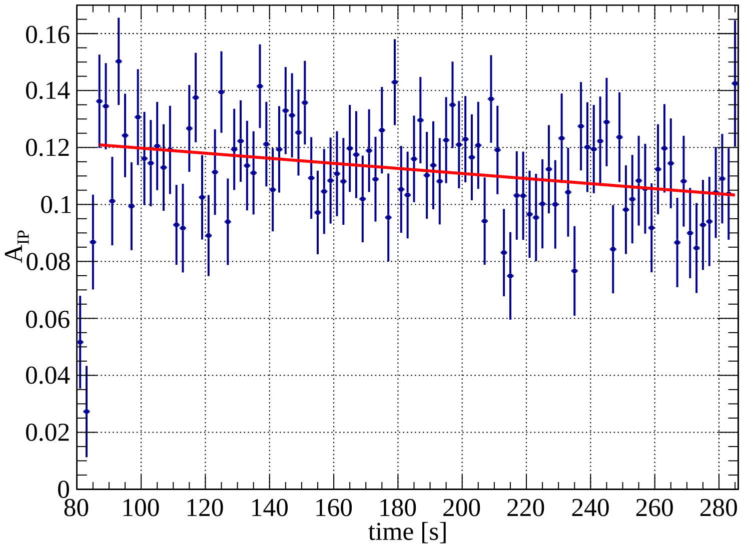

Figure 8.3: In-plane asymmetry A_{IP} from the start of solenoid operation to the end of the cycle. The rotation of beam polarisation from vertical to horizontal can be seen in the first few bins. The red line depicts the linear fit used to calculate the SCT.

by the step function:

$$A_{\mathrm{LR}}(t) = \begin{cases} A_{\mathrm{LR},0} & \text{if } t < t_{\mathrm{step}}, \\ A_{\mathrm{LR},0} + \Delta A_{\mathrm{LR}} & \text{if } t \geqslant t_{\mathrm{step}}. \end{cases} \tag{8.2.1}$$

Here, $A_{\mathrm{LR},0}$ is the left-right asymmetry before the jump, including the first flat region before the scan and ΔA_{LR} is the size of the jump in the asymmetry. , which occurs at the time bin t_{step}. The value of t_{step} is a fixed parameter for the individual fit process.

In the example RF Wien filter data shown in Fig. 8.4, the occurrence of resonance crossing (when the IPP rotation frequency matches the WF frequency) can be easily identified by the significant jump in A_{LR}. The initial asymmetry before the jump is represented by A_{LR}, and the jump in asymmetry is denoted by ΔA_{LR}. By fixing the time of resonance crossing t_{step} at 187 s, the experimental data was accurately described by the step function Eq. (8.2.1), as indicated by the black curve.

On the other hand, for axion scans, the jump sizes were not significant, and it would not be apparent when resonance crossing occurred, if at all. Therefore, in these cases, the step function fits Eq. (8.2.1) were repeated for each time bin between 120 s - 256 s as the fixed t_{step} value, and the jump size was recorded for each fit along with the χ^2 value of the fit. In the example shown in Fig. 8.4, two fits are calculated away from the resonance, and are given in red and green. For these two fits, the observed ΔA_{LR} values are smaller, and the resultant reduced χ^2 was of larger values, as shown

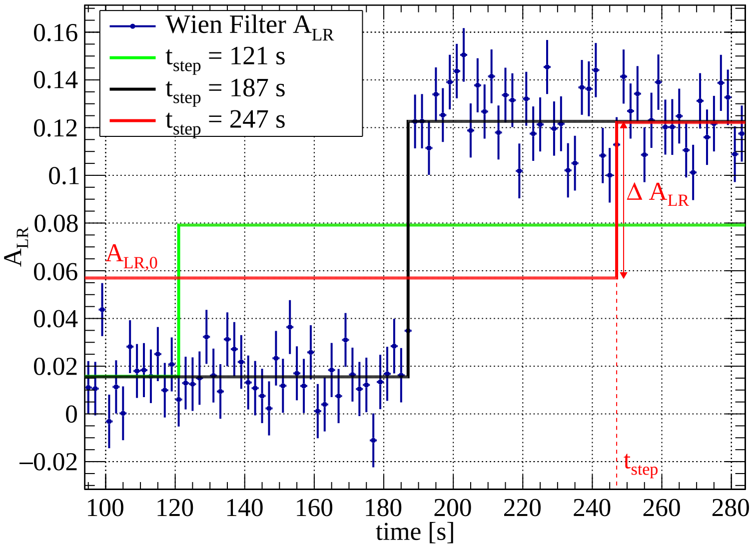

Figure 8.4: Examples of step function fits to the Wien filter scan data for a single bunch from one cycle. The black line represents the fit with the jump (t_{step}) at the resonance crossing. The red and green lines show the results for other choices of the jump time away from resonance.

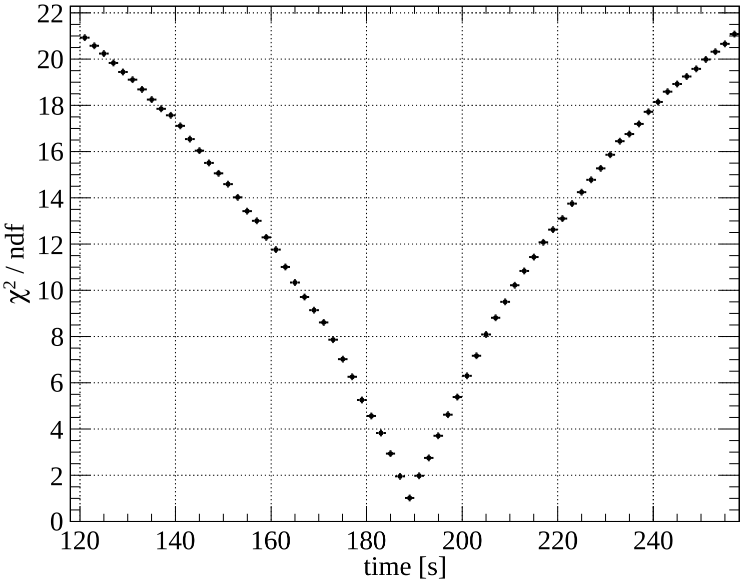

Figure 8.5: The plot shows the reduced chi-squared from fitting the step function to a Wien filter scan data from a single cycle, with the time assumed for the jump in the x axis, the same data set as in Fig. 8.4. The minimum corresponds to the time when the resonance occurs.

in Fig. 8.5. These features were searched for in each bunch and cycle from the ALP scans, and are explained in detail later in the section.

8.2.1 RF Wien filter scan analysis

The RF Wien filter scans, as explained in Section 6.3, encompassed 48 cycles with two different ramp rates, $\dot{f}_{\text{spin}}$= 0.05 Hz/s and 0.1 Hz/s. Due to the random nature of the phase between RF Wien filter and the polarisation direction at the start of each cycle, the jump value varied from cycle to cycle. However, within a cycle, all the bunches had the same jump size, with subsequent bunches displaying alternate signs of the jump. The statistical uncertainties of these jumps were estimated to be approximately 2%, based on the asymmetries used for jump calculation.

Figure Fig. 8.6 displays the distribution of the RF Wien filter jump sizes, calculated as above, for both the faster and slower scans. Each ΔA_{LR} calculated was normalised using $A_{\mathrm{IP}}(t)$ of the respective time bin. This normalisation enables the comparison between different cycles. Each plot includes a total of 192 jumps for the 4 bunches of the 48 cycles. The obtained jump values traced a sinusoidal pattern with an amplitude equivalent to the maximum possible jump for the case, as the random phase affected the measurements. The distributions of the jumps resembled the y-projection of a sinusoid. However, probing a sine function with a finite number of points resulted in a downward bias in the estimation of the maximum jump value, while the smearing of points had the opposite effect on the calculation of the maximum.

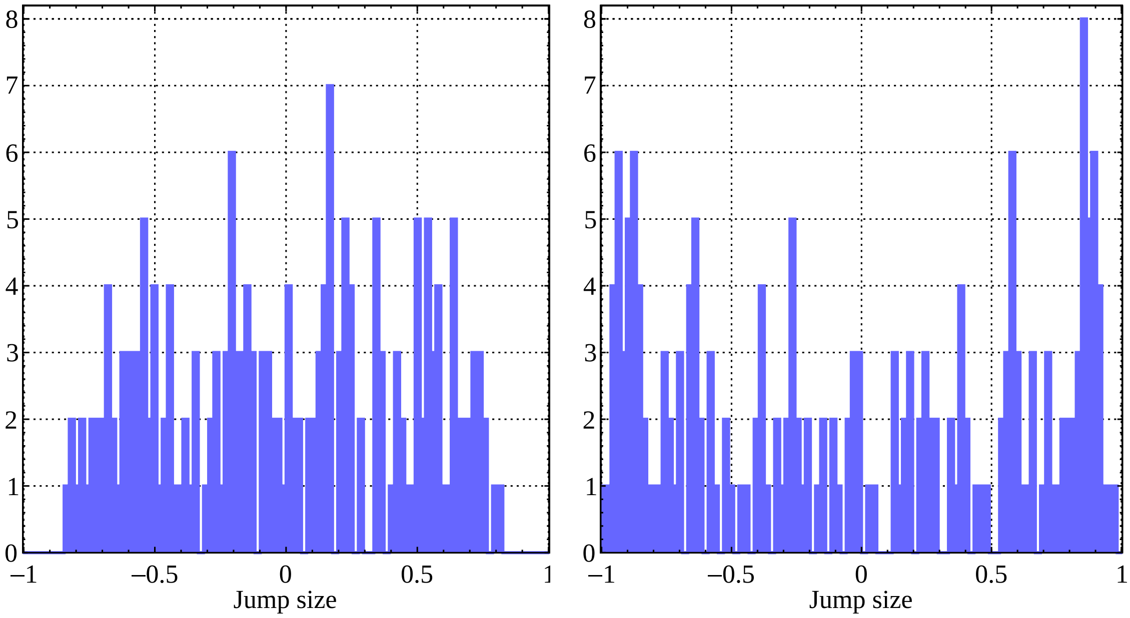

Figure 8.6: The distribution of jump sizes for the fast WF scan is shown in the left plot, while the slow scan is shown in the right plot. Each plot contains 192 jumps, corresponding to 4 bunches in 48 cycles. Note that the jump values have been renormalised using the $A_{\mathrm{IP}}(t)$.

To obtain a more accurate estimate of the jump value for a given ramp setting, a histogram of jump values from every cycle was created. The jump value for each cycle was calculated as the average of the absolute values of the jumps from the bunches. The maximum jump was determined as the half-way distance between the bin with the maximum content in the upper 20% of the distribution and the rightmost bin with non-zero content. This procedure was validated through Monte-Carlo simulations, wherein the process was repeated 200 times and found to be robust. This allowed for the downward bias resulting from probing the sine function with a limited number of points to be mitigated by the possible upward bias arising from the statistical uncertainty of the jump distribution. A standard deviation of 2% was calculated for the maximum jump obtained from the Monte-Carlo simulations, which is comparable to the experimental uncertainties. This procedure allows for the accurate determination of the maximum polarisation jump for the Wien filter scans.

The experimental values resulting from the aforementioned calculation are presented in Table 8.1, along with the simulation values obtained from the previous chapter. Although the numbers do not fall within the uncertainties, when considered collectively, the simulations provide proper modelling of sensitivity. Consequently, these results serve as a benchmark for our simulations and instil confidence in the calibration curve for the axion scans.

Table 8.1: Comparison of the maximum polarisation jump ΔP_y from simulation and experiment for the Wien filter test.

Δp [MeV/c]	Simulation	Experiment
0.112	0.75	0.796(15)
0.056	0.93	0.892(18)

8.2.2 ALP scan analysis

For the data from the axion scan runs, the calculation of the vertical polarisation jump follows the same steps as for the RF Wien filter data, using the step function fit for each and every bunch from all cycles. An example of such a fit with axion data is shown in Fig. 8.7, where we see that the jump is consistent with zero. Similarly, the accompanying reduced chi-squared plot Fig. 8.8 shows no evidence of a minimum, ruling out the possibility of resonance. The standard deviation of the individual χ^2 value from the fit, shown as uncertainties in Fig. 8.8, was calculated using the formula $\sqrt{2/\mathsf{ndf}}$, where ndf is the number of degrees of freedom in the fit. For our analysis, ndf was calculated as the sum of flat region points and scan region points subtracted by the number of fit variables, i.e., $2 \times 15 + 68 - 3 = 95$, resulting in a standard deviation of 0.145. Figures of step function fits for axion scan data (referring to Figs. 8.7 and 8.8) are analogous to the step function fits for Wien filter data shown in Figs. 8.4 and 8.5, besides the fact that they do not reveal the obvious step feature.

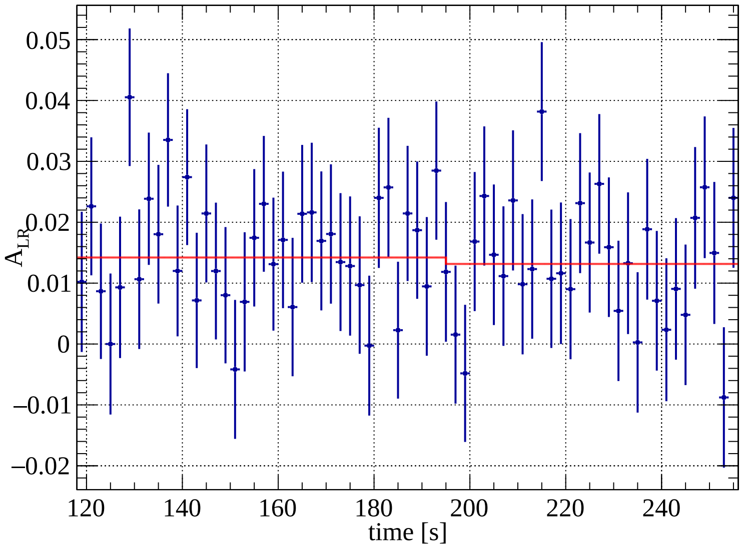

Figure 8.7: A sample step function fit for an axion scan of a single bunch from one cycle, where we see no jump in asymmetry. For the investigated time bin $\Delta A_{\mathrm{LR}} = -0.001(2)$ being consistent with zero.

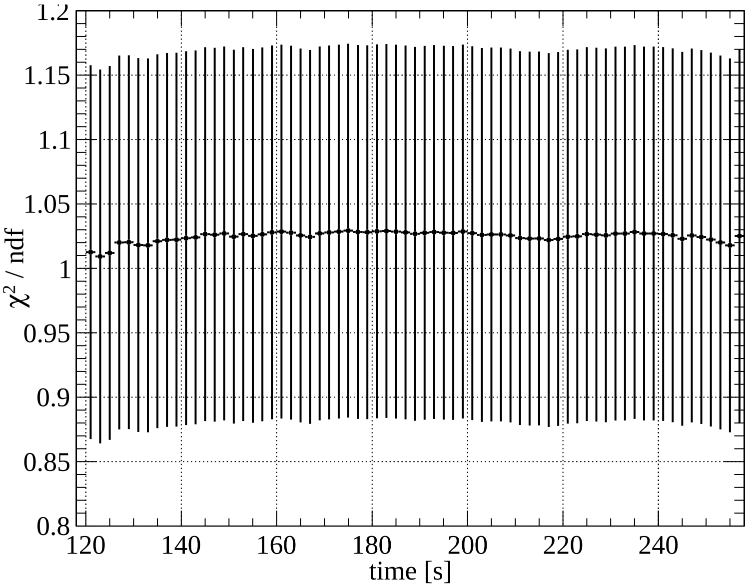

Figure 8.8: Reduced chi-squared values from the step function fits to the axion scan data from a single cycle Fig. 8.7. Vertical bars represent the standard deviation of the chi-squared values based on the number of degrees of freedom. The absence of a minimum suggests no resonance.

To incorporate data from all four bunches in the analysis, the ΔA_{LR} jumps from the step function fit to each time bin was normalised with the IPP asymmetry for the respective time bin. The normalised asymmetries $\Delta A_{\mathrm{LR}}/A_{\mathrm{IP}}(t_{\mathrm{step}})$ of all four bunches in each time bin of a cycle were combined to form a single sinusoidal curve and the amplitude of this curve can be calculated as:

$$f(\phi_m) = C_1 \sin\phi_m + C_2 \cos\phi_m, \tag{8.2.2}$$

$$\hat{A} = \sqrt{C_1^2 + C_2^2}, \tag{8.2.3}$$

Here, $\hat{A}$ is estimated polarisation amplitude, and ϕ_m is the angle between the polarisation of bunch m and their rest frame electric field $\vec{E}^*$, as explained in Section 7.2. An example of this sinusoidal fits to the normalised ΔA_{LR} is shown in Fig. 8.9. and the spacing of the angle ϕ_m in x axis is $\pi/2$ as shown in Fig. 7.1. However, as mentioned in Section 7.2, the spacing is not always the same, but oscillates as the bunches go through the straight and arced sections of the ring, which requires a correction to be applied at the end of the analysis. The data on the y axis in Fig. 8.9 are normalised to the in-plane asymmetry A_{IP}, and the amplitude calculated using Eq. (8.2.3) is the estimated jump amplitude $\hat{A}$ from the experiment. $\hat{A}$ is calculated for each time bin during the ramps, and an example of estimated amplitude for a single cycle using all four bunches is given in Fig. 8.10.

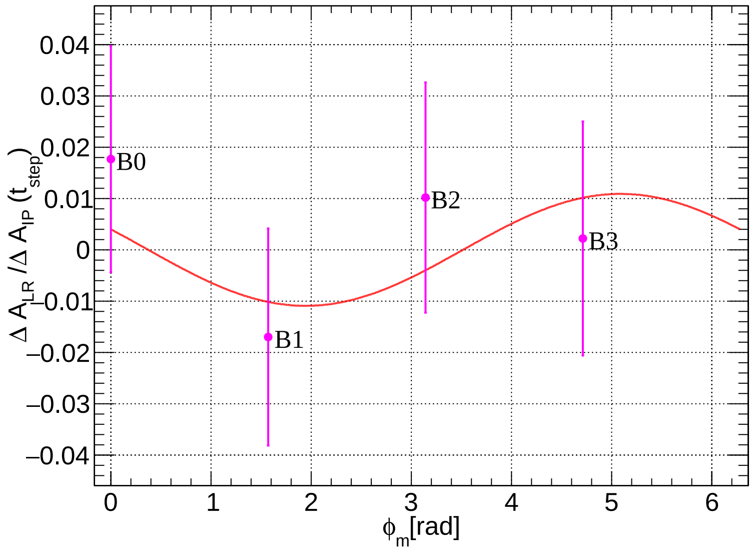

Figure 8.9: Normalised left-right asymmetry jump for all four bunches, for a single time bin in a cycle of axion data, plotted as a function of the angle ϕ_m between the bunch polarisation and $\vec{E}^*$. The red curve represents the sinusoidal fit used to calculate the jump amplitude $\hat{A}$.

For each run consisting of multiple cycles covering the same frequency range, given the absence of any visible resonance, we could calculate the weighted average of the amplitudes from individual cycles. This mean amplitude, along with its uncertainties, is used to calculate the confidence intervals for our data in the next section.

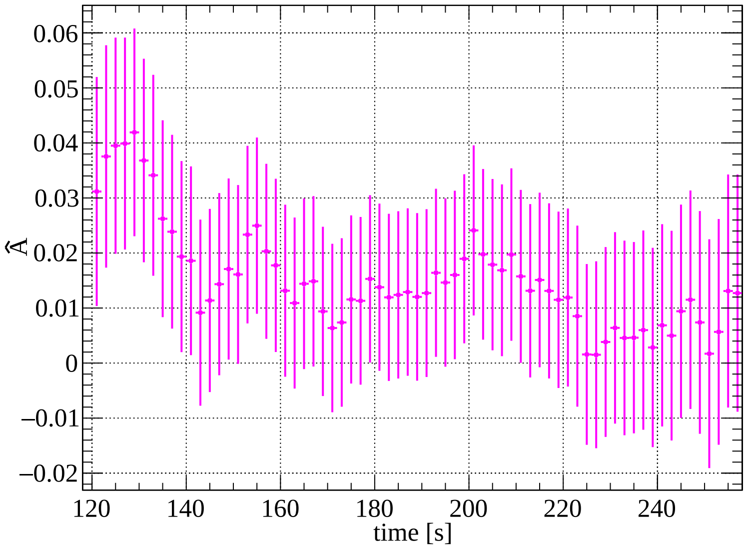

Figure 8.10: Estimated left-right asymmetry jump amplitude $\hat{A}$, obtained from a sinusoidal fit as shown in Fig. 8.9, for each .time bin during the ramps for a single cycle of axion data.

8.3 Feldman-Cousins algorithm to obtain the confidence interval

We employ Eqs. (8.2.2) and (8.2.3) to calculate the estimated amplitude $\hat{A}$ from the four bunches, regardless of the phase of the axion. This method introduces a positive bias when the values are close to zero, which vanishes when the estimated values are significantly larger than their uncertainties. However, since the estimated amplitudes in our case are often close to zero, we must account for this bias when calculating confidence intervals. To address this issue, we make use of the Feldman-Cousins method, which was first described in [100], to calculate the confidence intervals. This method allows us to calculate the true value of the amplitude A from the experimentally estimated amplitude value $\hat{A}$. The application of the FC to calculate confidence intervals can also be found in [103, 104].

Assuming that the C_1 and C_2 in Eq. (8.2.2) are uncorrelated and have a normal distribution, the Probability Distribution Function (PDF) for $\hat{A} = \sqrt{C_1^2 + C_2^2}$, as given in [103], can be written as follows

$$f\left(\hat{A}|A,\sigma_{\text{exp.}}\right) \mathrm{d}\hat{A} = \frac{1}{\sigma_{\text{exp.}}^2}\, e^{-\left(\dfrac{\hat{A}^2 + A^2}{2\sigma_{\text{exp.}}^2}\right)} \hat{A}\ I_0\left(\frac{\hat{A}A}{\sigma_{\text{exp.}}^2}\right) \mathrm{d}\hat{A}, \tag{8.3.1}$$

where $\sigma_{\text{exp.}}$ is the uncertainty in the estimation of $\hat{A}$, and I_0 is the modified Bessel function of the first order. The distribution is called a Rice distribution [105]. Since the calculations have to be repeated for every single time bin in the ramping stage of the cycle, across all the runs, the amplitudes are normalised to their uncertainties, which simplifies the calculations. This results in the normalised estimated amplitude $\hat{P}$ $(= \hat{A}/\sigma_{\text{exp.}})$ and normalised true amplitude P. The corresponding PDF can be rewritten as

$$f\left(\hat{P}|P\right) \mathrm{d}\hat{P} = e^{-\left(\dfrac{\hat{P}^2 + P^2}{2}\right)} \hat{P}\ I_0(\hat{P}P)\ \mathrm{d}\hat{P}. \tag{8.3.2}$$

Figure 8.11 shows the Rice distribution from Eq. (8.3.2) at four different values of P. We see that as P becomes larger, the Rice distribution converges to a Gaussian distribution. This is evident from the curve corresponding to $P = 5$, which denotes a physical effect that is five standard deviation away. The blue data points are the distribution of the experimental data that was analysed, and we see an agreement with the Rice distribution for $P = 0$ (red curve).

A 2-dimentional representation of the Rice distribution is shown in Fig. 8.12 for $0 \leqslant P \leqslant 6$. If we consider the y projection of the plot, it would resemble a Gaussian, centred at $P = \hat{P}$, when these projections are calculated farther from zero. The shape of the projection starts to distort from the Gaussian shape as P approaches zero. This becomes evident at $P \approx 2.5$. The red line on the Rice plot denotes the quantity P_{best}, which is the value of P for which the $f\left(\hat{P}|P\right)$ has the maximum, and is in the physically allowed region of P. In other words, P_{best} represents the most probable true value of the amplitude given a certain estimated value. From this curve, we can see that for an estimation of $\hat{P}$ up to ≈ 1.4 the most probable P is zero. This implies that even when there is no physical effect, we might still observe signals that are one standard deviation significant.

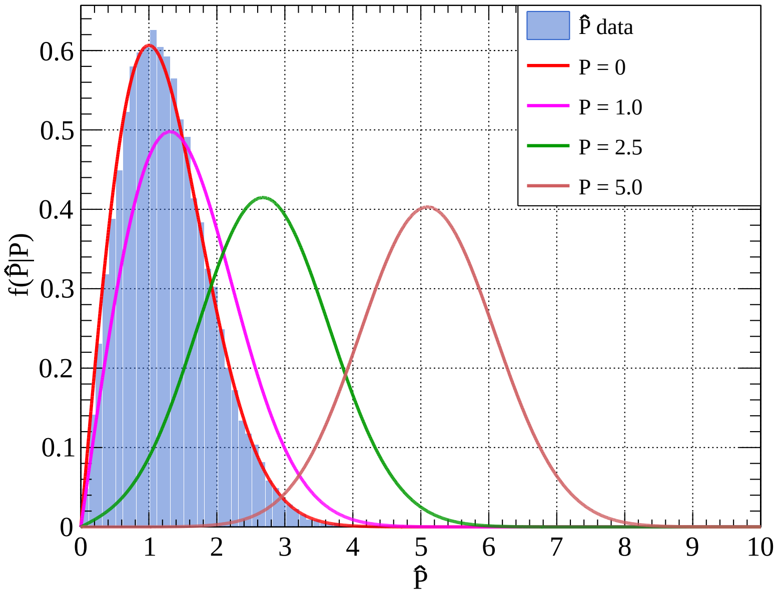

Figure 8.11: A histogram of experimental $\hat{P}$ data (blue bars). The coloured lines represent the $f(\hat{P}|P)$ distribution for different values of P. The red curve for $P = 0$ matches the experimental data.

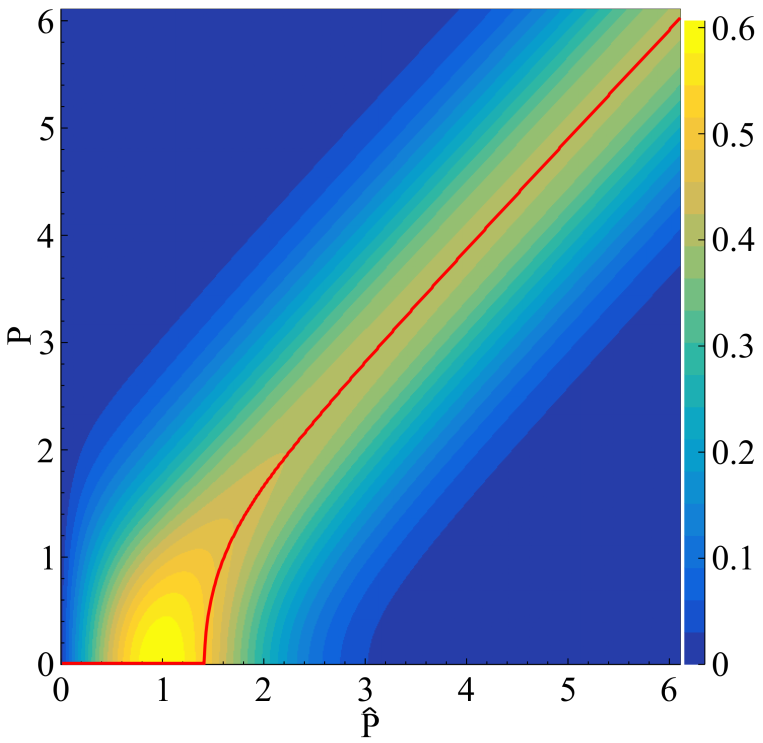

Figure 8.12: A Rice plot depicting two-dimensional data for a single cycle. The red line represents the value of P at which the probability density function (PDF) given by Eq. (8.3.2) is maximized, for a given value of $\hat{P}$.

8.3.1 Feldman-Cousins algorithm

To compute the confidence intervals using the Feldman-Cousins method, we use the maximum likelihood ratio R as defined in [100] using the formula,

$$R(\hat{P}|P) = \frac{f(\hat{P}|P)}{f(\hat{P}|P_{\text{best}})}. \tag{8.3.3}$$

The likelihood ratio for two different values of P is shown in the top row of Figure 8.13. The bottom row shows the corresponding Probability Distribution Function. The shaded grey region represents the 90% confidence interval for respective P values.

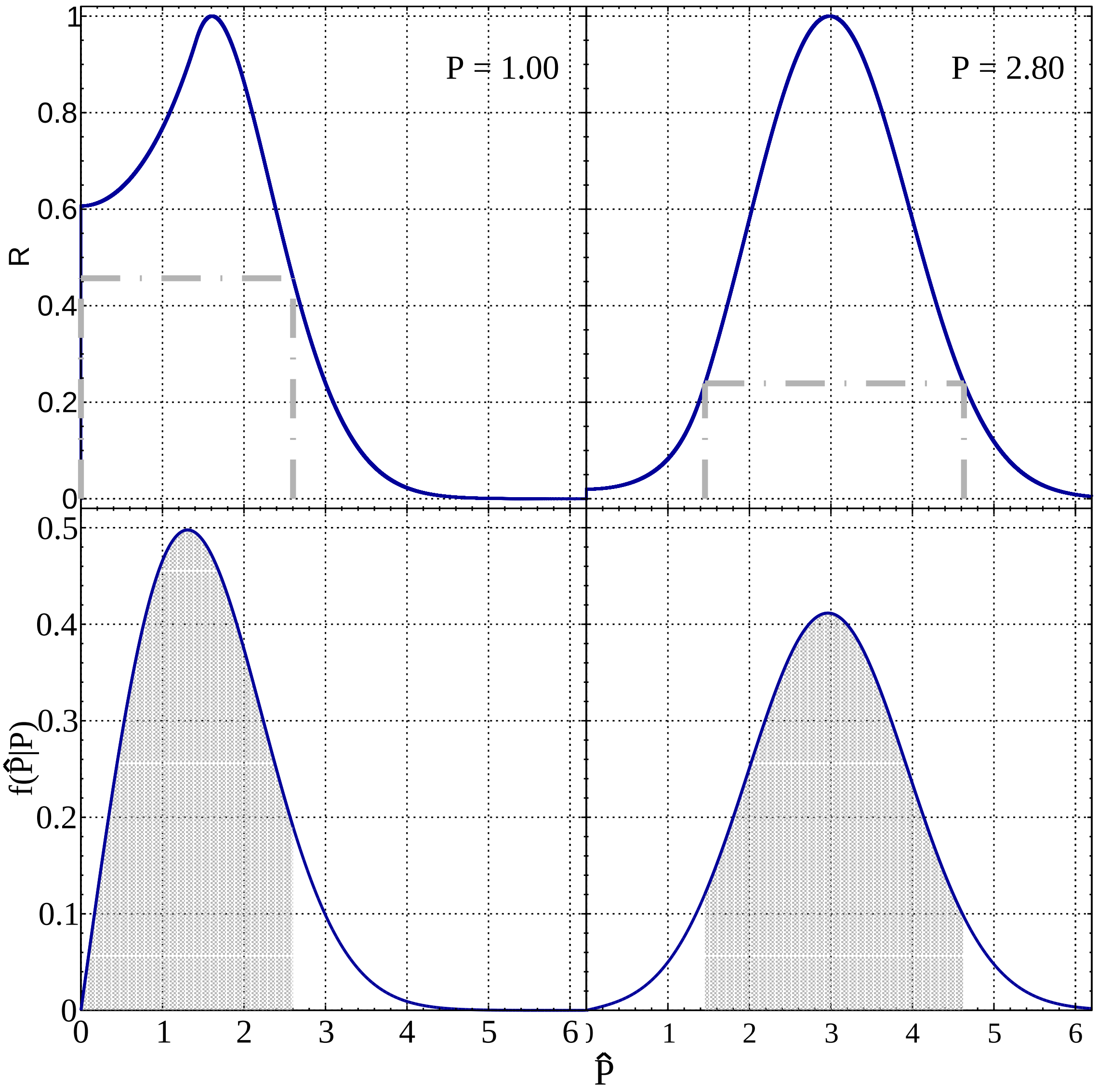

Figure 8.13: Examples of calculating 90% confidence limits using the likelihood ratio R drawn in the top row, and the Probability Distribution Function drawn in the bottom row for two values of P, $P = 1.0$ (left) and $P = 2.8$ (right). The grey horizontal dashed line in the likelihood ratio curves represents the R value for which the corresponding $\hat{P}$ values (grey vertical dashed lines) form the 90% integral in the PDF curves. The grey shaded region denotes the 90% integral region.

To construct the confidence interval at any given value of P, the FC algorithm finds an interval $[\hat{P}_1, \hat{P}_2]$ such that (see ref. [106])

$$R(\hat{P}_1) = R(\hat{P}_2). \tag{8.3.4}$$

This interval is calculated by integrating $f(\hat{P}|P)$ between $\hat{P}_1$ to $\hat{P}_2$ until the desired confidence limit is reached (90%). This can be expressed as,

$$\int_{\hat{P}_1}^{\hat{P}_2} f(\hat{P}|P)\,\mathrm{d}p = 0.9. \tag{8.3.5}$$

Thus, the confidence interval $[\hat{P}_1, \hat{P}_2]$ can be found as a solution of the set of two equations Eqs. (8.3.4) and (8.3.5). Eq. (8.3.5) is solved numerically by choosing $\hat{P}_1$ and $\hat{P}_2$ in decreasing order of likelihood ratio R. In the upper row of ??, the grey vertical lines represent the intervals $[\hat{P}_1, \hat{P}_2]$ as the solution of the two sets of equations.

This procedure is repeated for all values of P, and the resulting bounds are recorded in the plot shown in Fig. 8.14 as confidence intervals. The grey region in the plot corresponds to a 90% confidence limit, while the blue region corresponds to a 68% confidence limit. To calculate the limits on the true value for a given estimated value $\hat{P}$, we trace a line vertically from $\hat{P}$ (represented by the black vertical line) until it crosses the boundary of the confidence intervals. In the example depicted in the plot, only an upper limit exists (represented by the two horizontal black lines for 90% and 68% CL), and the lower limit is zero (a physical boundary on the value).

8.3.2 Confidence intervals for multiple cycle analysis

In order to account for the fact that most scans in the experiment consist of multiple cycles (usually 8, but sometimes 7, 9, or 16), it is necessary to construct the confidence interval accordingly. Since, it was observed during the experiment that the beam current was consistently reproduced from cycle to cycle for a particular scan, we can assume that the values of $\sigma_{\text{exp.}}$ (the uncertainty in estimation of $\hat{A}$) remain the same, and thus allowing us to average over these cycles by using the Central Limit Theorem (CLT).

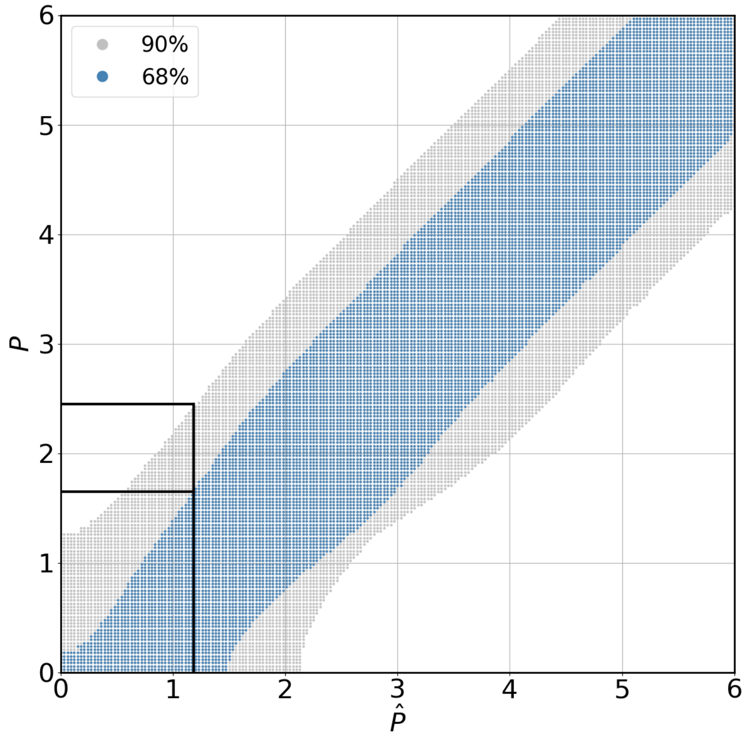

Figure 8.14: Plot depicting a 68% (blue) and 90% (grey) confidence interval for one cycle analysis. The horizontal axis represents the estimated value $\hat{P}$ and the vertical the true value P.

Central Limit Theorem

The CLT states that for a large number of independent samples, the distribution of sample means will approach a normal distribution, regardless of the shape of the sample distribution. Since we know the probability distribution function for a single cycle (Rice distribution), we can leverage the CLT to combine n cycles and create the confidence interval. First, let us consider the mean and variance of the Rice distribution:

$$\mu_{\text{Rice}} = \sigma_{\text{exp.}}\sqrt{\frac{\pi}{2}}\; L_{1/2}\left(-\frac{A^2}{2\sigma^2_{\text{exp.}}}\right), \tag{8.3.6}$$

$$\sigma^2_{\text{Rice}} = 2\sigma^2_{\text{exp.}} + A^2 - \frac{\pi\sigma^2_{\text{exp.}}}{2}\; L^2_{1/2}\left(-\frac{A}{2\sigma^2_{\text{exp.}}}\right), \tag{8.3.7}$$

where L denotes the generalised Laguerre function, and A is the true amplitude and $\sigma_{\text{exp.}}$the experimental uncertainty for, both a single cycle

From CLT, the mean of the Rice distribution would remain the same when considering n cycles, but the uncertainty would be $\sigma_{\text{exp.}}/\sqrt{n}$. Therefore, the normalised amplitude for n cycles can be expressed as:

$$P = \frac{A}{\left(\frac{\sigma_{\text{exp.}}}{\sqrt{n}}\right)}, \tag{8.3.8}$$

Thus, the corresponding mean and variance of n cycle Rice distribution, for normalised amplitude are:

$$\tilde{\mu}_{\text{Rice}} = \sqrt{n}\sqrt{\frac{\pi}{2}}\, L_{1/2}\left(-\frac{1}{2}\frac{P^2}{n}\right), \tag{8.3.9}$$

$$\tilde{\sigma}^2_{\text{Rice}} = 2 + \frac{P^2}{n} - \frac{\pi}{2}\, L^2_{1/2}\left(-\frac{1}{2}\frac{P^2}{n}\right). \tag{8.3.10}$$

Thus, according to CLT, the Probability Distribution Function for n cycles is given as the Gaussian distribution:

$$f(\hat{P}|P) = \frac{1}{\sqrt{2\pi\tilde{\sigma}^2_{\text{Rice}}}}\, e^{-\left(\frac{\left(\hat{P} - \tilde{\mu}_{\text{Rice}}\right)^2}{2\tilde{\sigma}^2_{\text{Rice}}}\right)}. \tag{8.3.11}$$

A 2-dimensional PDF for $n = 8$ is shown in Fig. 8.15, with the red line denoting the P_{best} values. The process of constructing confidence intervals follows the same approach as the 1-cycle case. The resulting confidence interval for $n = 8$ cycles is depicted in Fig. 8.16. The boundaries of the blue and grey bands in the plot represent the 68% and 90% confidence levels, respectively. Similar to the 1-cycle case, the two horizontal black lines show the upper limits at 68% and 90% for an estimated $\hat{P} = 3.3$.

When calculating the limits using Fig. 8.16, we must be cautious for $\hat{P}$ values that are less than the expected value $\tilde{\mu}_{\text{Rice}}$. While, on average, the expected value of the estimated amplitude is $\hat{P} = \tilde{\mu}_{\text{Rice}}$ for a true amplitude of zero $P = 0$, it is possible to measure smaller amplitudes $\hat{P} < \tilde{\mu}_{\text{Rice}}$ due to statistical fluctuations. This can result in a smaller confidence interval, as for $\hat{P} = 1.5$ in Fig. 8.16. This is similar to the case when measuring a cross-section signal (s) against background events $b = 4$ and obtaining an observed value of $(s + b)_{\text{obs}} = 3$ does not imply a negative cross-section $s = -1$, but should rather be attributed to statistical fluctuations. As explained in Ref. [100], in such cases, the confidence interval is calculated for the expected value.

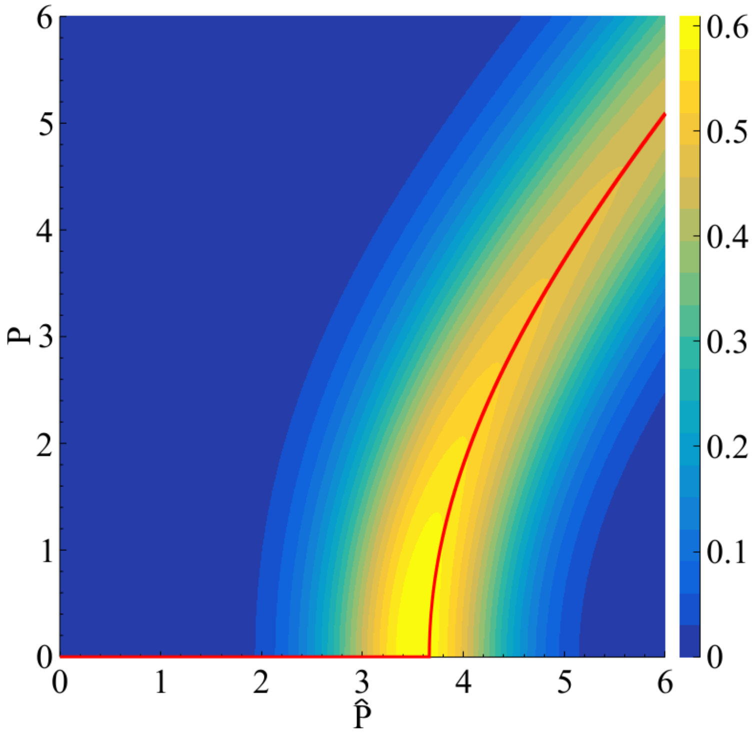

Figure 8.15: A Rice plot depicting 2-dimensional data for 8 cycles. The red line represents the value of P at which the PDF given by Eq. (8.3.11) is maximised, for a specific value of $\hat{P}$.

Therefore, for any observed values smaller than the expected value $\hat{P} < \tilde{\mu}_{\text{Rice}}$, the confidence intervals for P are calculated at $\tilde{\mu}_{\text{Rice}}$.

For each estimated value of the amplitude $\hat{P}$, the confidence interval boundaries of P are determined, and then multiplied by the experimental uncertainty (as shown in Eq. (8.3.8)) to obtain the true amplitude A. Notably, no signal was observed that could not be explained by a statistical fluctuation in the frequency (or axion mass) range covered by the experiment. As per the 90% confidence interval, it is expected that approximately 10% of the cases will have a lower limit greater than zero. This expectation is evident in our observation in Fig. 8.17, where the PDF for $P = 0$ is overlaid on the estimated $\hat{P}$ for $n = 8$ cycles from the experiment. We observe that 9.63% of the data points are to the right of the red dashed line $\hat{P} > 4.38$. $\hat{P} = 4.38$ is the value above which the lower limit of the 90% confidence interval in Fig. 8.16 is greater than zero. Based on this observation, we can infer that, at the level of precision achieved, there is no systematic effect that would result in a false signal.

The equation for converting the limits of the amplitude A into the limits of the oscillating EDM of deuteron, as provided in Eq. (7.3.10) in Chapter 8, can be simplified

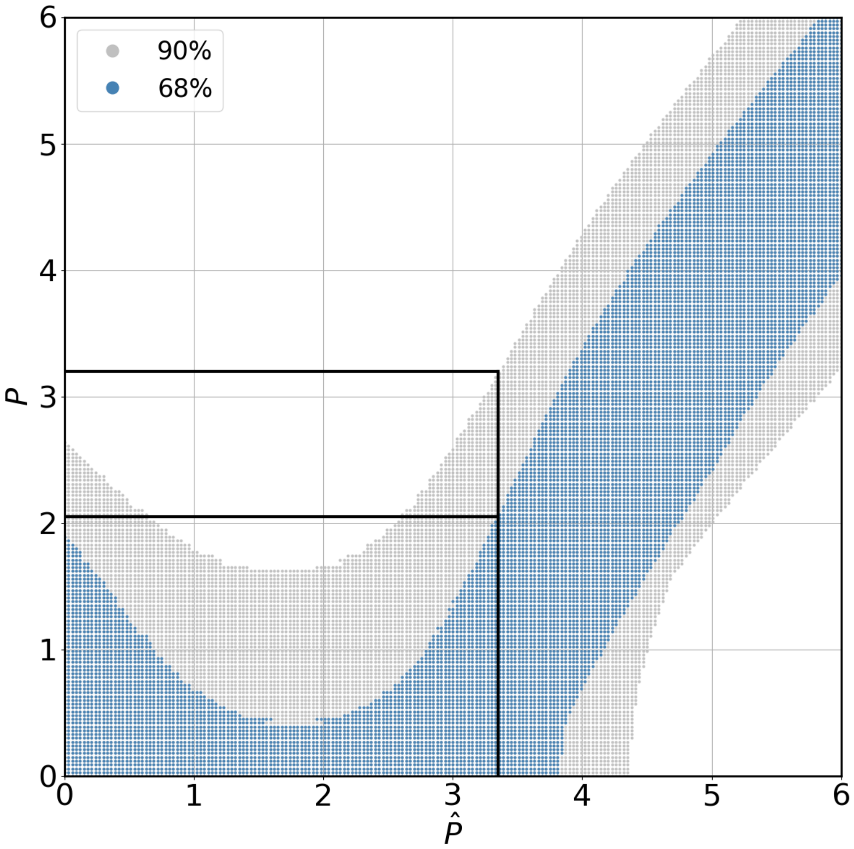

Figure 8.16: A confidence interval of 68% (blue) and 90% (gray) calculated for the multi-cycle analysis with a sample size of $n = 8$. The horizontal axis represents the estimated experimental value $\hat{P}$, while the vertical the true value P. When the experimental value is $\hat{P} = 3.3$, the true value P is estimated to fall within the range of 0 to 3.15 with a confidence level of 90%.

as follows:

$$| d_{\mathrm{AC}} | = \lambda A \times 1 \times 10^{-23} \, e \, \mathrm{cm}, \tag{8.3.12}$$

where the coefficient λ is 316 for fast ramps and 286 for slow ramps, as derived in Section 7.3. The results, which depict the limits on oscillating EDM, and several axion couplings, will be presented and discussed in the next chapter.

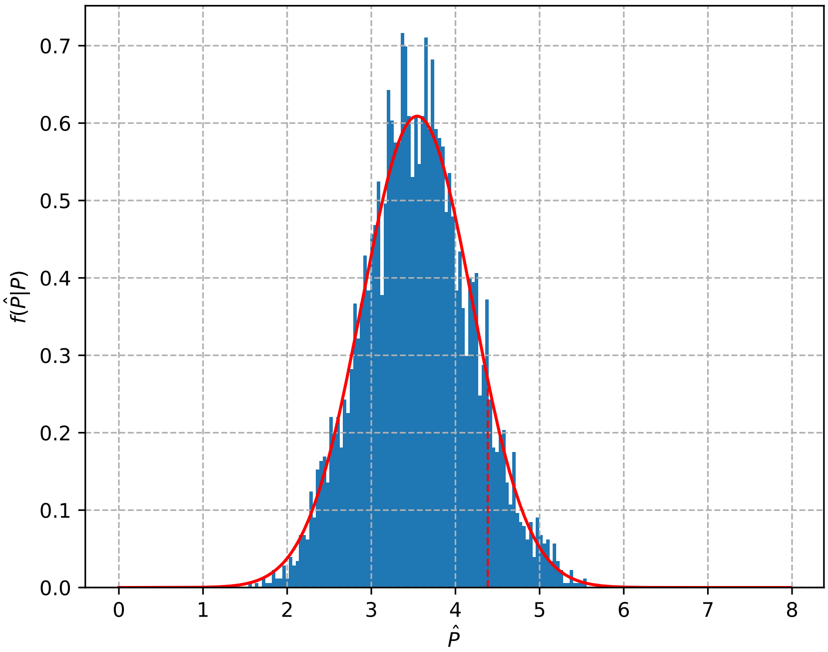

Figure 8.17: A histogram of the experimental $\hat{P}$ data for $n = 8$ cycles. The red curve represents the Probability Distribution Function calculated for $P = 0$ from Eq. (8.3.11), and it shows good agreement with the histogram.

9 Results and discussion

The findings and results discussed in this chapter have previously been published in ref. [83], and only the parts of the research that the author analysed are presented here[1].

We have discussed the procedure for obtaining the jump amplitude limits from the measured polarisation data in the experimentally scanned frequency (ALP mass) region. This procedure accounts for the systemic bias and shows that no significant effects have been observed compared to statistical fluctuations. The polarisation jump amplitudes are attributed to the rotation of the polarisation, in the extended-T-BMT equations Eqs. (3.3.7) and (3.3.10) explained Chapter 3. The angular velocities of the spin of particles moving in a storage ring, with mass m, charge q, spin S, Lorentz factor γ, and velocity $\vec{v} = c\vec{\beta}$ is given by Eqs. (3.3.10a) to (3.3.10c). According to [23, 76], the oscillating terms of the angular velocity are given by:

$$
\begin{aligned}
\vec{\Omega}_{\mathrm{a}(t)} &= -\frac{1}{S\hbar}\,\frac{d_{\mathrm{AC}}}{a_0}\;a(t)\;c\vec{\beta}\times\vec{B} - \frac{1}{S\hbar}\frac{C_N}{2f_a}\hbar\partial_0 a(t)\vec{\beta} \\
&= d_{\mathrm{AC}}\frac{c\gamma m}{q\hbar S}\cos\left[\omega_a(t-t_0)\;+\phi_a(t_0)\right]\,\vec{\beta}\times\vec{\Omega}_{\mathrm{rev}} \\
&\qquad + \frac{C_N}{2f_a S}\;\omega_a a_0\;\sin\left[\omega_a(t-t_0)+\phi_a(t_0)\right]\;\vec{\beta}.
\end{aligned}
\tag{9.0.1}
$$

Here, the laboratory frame magnetic field was expressed in terms of the angular revolution velocity $\vec{B} = (-m_a\gamma/q)\vec{\Omega}_{\mathrm{rev}}$ as shown in Eq. (3.3.9). These oscillations occur

---

[1] The author would like to extend her gratitude to Andreas Wirzba for his invaluable help in interpreting the results.

when a classical ALP field a given by Eq. (2.1.4) couples to the particles in the beam, as described by the Lagrangians Eqs. (2.2.3) and (2.2.5). Furthermore,

The rotation due to ALPs, described by Eq. (9.0.1), occurs about two axes: the $\vec{\beta} \times \vec{\Omega}_{\text{rev}}$ axis in the first, and the $\vec{\beta}$ axis in the second term. The first rotation is generated by the AC part of the Electric Dipole Moment of the particles induced by the ALP field Eq. (2.1.4), and is about the axis vertical to the ring plane. The second rotation, with respect to the longitudinal axis $\vec{\beta}$ (see Refs. [23, 76]), follows the pseudomagnetic axion-wind effect [18, 107] of strength C_N/f_a, which is expressed in terms of the axion decay constant f_a [1]. As these two rotations take place around the orthogonal axes, the change in vertical polarisation that occur on resonance are $\pi/2$ out of phase with each other. Consequently, the rotation amplitudes of the two oscillating terms in Eq. (9.0.1) add up coherently, making it impossible to distinguish between the two rotations. Therefore, we provide an upper limit on either d_{AC} or C_N/f_a, assuming that the other term vanishes and that the bound is saturated by one term only.

9.1 Limits on the oscillating Electric Dipole Moment

We start by assuming that only the oscillating EDM-term is present, meaning $C_N/f_a = 0$. Figure 9.1 shows the sensitivity at a 90% confidence level for excluding the ALPs-induced oscillating EDM of the deuteron d_{AC}, in frequency range of 120.0 kHz - 121.4 kHz (f_{osc} in the lower axis), corresponding to the axion mass range of 0.495 neV c^{-2} - 0.502 neV c^{-2} as represented on the upper axis. The darker lines represent the upper limit of the oscillating EDM, while the lighter filler region indicated the exclusion region. The colours green and blue differentiate between the two different ramp rates used in the experiment, as mentioned in Chapter 6. The green colour corresponds to a momentum change of $\Delta\ p = 0.112$ MeV/c and the blue colour corresponds to a momentum change of $\Delta\ p = 0.138$ MeV/c per cycle.

The fluctuations in the exclusion plot are primarily due to two beam properties; namely intensity and polarisation. Good beam properties mean better sensitivity.

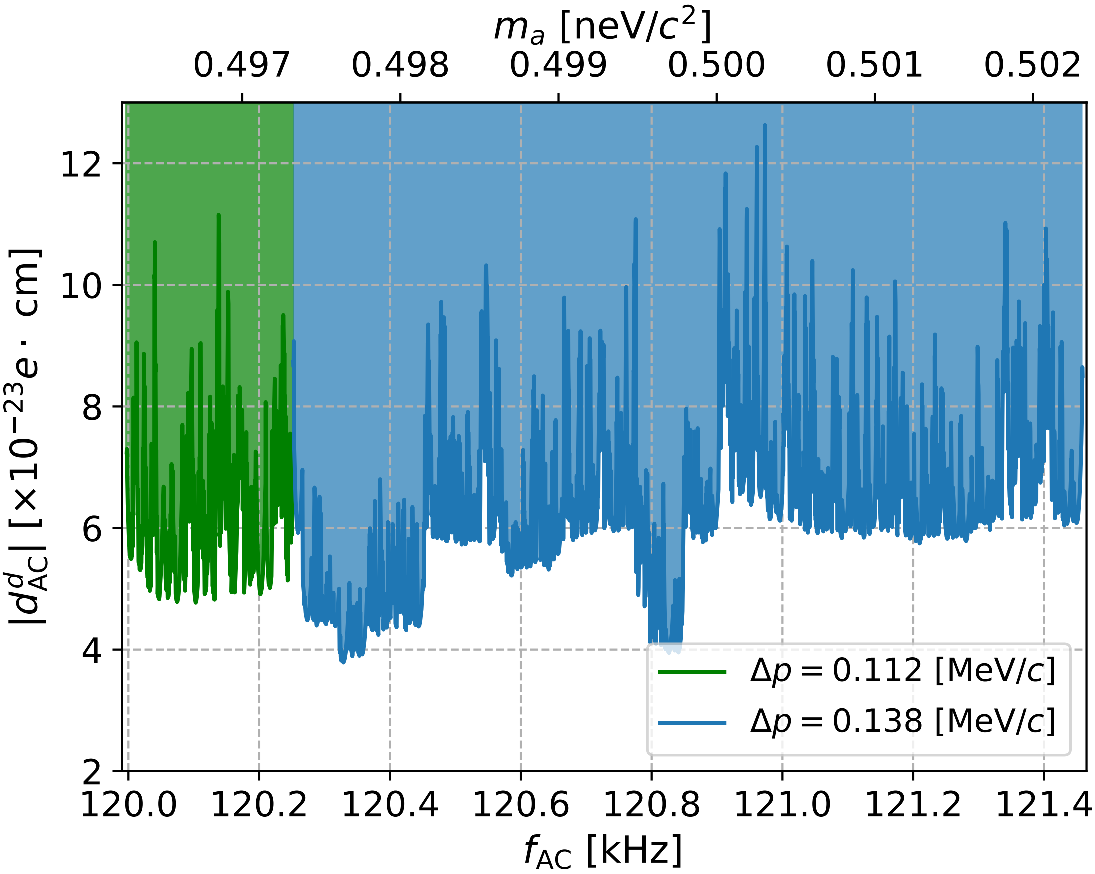

Figure 9.1: The sensitivity at a 90% confidence level to exclude the presence of ALP induced oscillating EDM in units of e cm in the frequency range 120.0 kHz - 121.4 kHz with the corresponding mass range of $m_a = 0.495\,\mathrm{neV}\,c^{-2} - 0.502\,\mathrm{neV}\,c^{-2}$. Further details in the accompanying text.

The dependency of intensity is evident on a larger scale over multiple scans. If a larger number of scans were performed for a specific frequency range, the calculated sensitivity is better, as seen in Fig. 9.1 around frequency 120.8 kHz, for example. The decline in sensitivity within a cycle is mainly due to beam depolarization.

A minor contribution to these fluctuations arises from the approach to the calculation of ΔA_{LR} in Eq. (8.2.1). As a consequence, the sensitivity becomes worse as one moves further from the middle of the scan because the imbalance in the number of points on both sides of the anticipated jump in the calculation of ΔA_{LR} leads to a larger uncertainty in the determined jump. An example of how this sensitivity appears for a single scan region comprising 8 cycles is shown in Fig. 9.2. However, the greatest influence is still beam intensity and the polarisation, and their combined effect leads to the larger oscillating EDM bounds ($|d^d_{\mathrm{AC}}| > 8{\times}10^{-23}\,e\,\mathrm{cm}$).

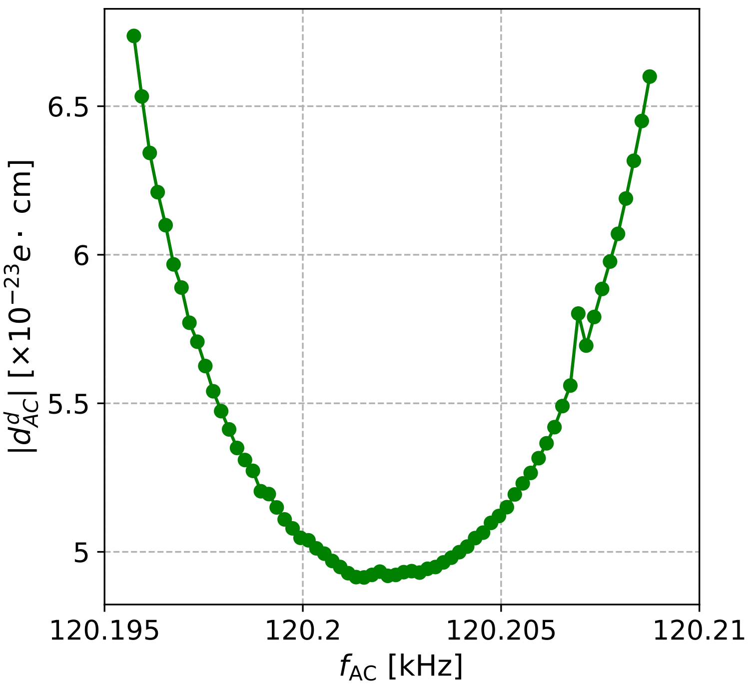

Figure 9.2: Illustration of the sensitivity of a single scan, which decreases as one moves away from the central frequency. This example contained 8 cycles from the slower scans.

The experiment conducted to search for ALPs in the storage ring yields a 90% confidence level upper bound of

$$\left|d^d_{\mathrm{AC}}\right| < 6.4{\times}10^{-23}\,e\,\mathrm{cm}. \tag{9.1.1}$$

This bound is obtained by averaging the individual limit points in Fig. 9.1, and it is used to calculate the various ALP coupling constants in the next section.

9.2 Limits of various ALP couplings

In Section 2.2 we discussed various ALP couplings. Here, we focus on coupling of ALPs with the deuteron either through oscillating EDM (d^d_{AC}) or through the axion-wind effect, which is proportional to C_d/f_a. These calculations assume that all the local dark-matter density, $\rho_{\mathrm{LDM}} = 0.55(17)\,\mathrm{GeV\,cm^{-3}}$, consists solely of ALPs (see

Chapter 27 ”Dark Matter” of Ref. [1]). The figures presented in this section were originally from Ref. [108] and have been modified to incorporate our findings.

ALP coupling to deuteron EDM

First, we will consider the direct coupling of axions to the deuteron EDM operator $g_{ad\gamma}$, which is analogous to the axion coupling to the nucleon EDM operator $g_{aN\gamma}$ explained in Section 2.2.3 and Eq. (2.2.3). Expressing Eq. (2.2.4) (with $N := d$ for deuterons) in terms of the electromagnetic fine-structure constant $\alpha = e^2/4\pi$, we get

$$\left|g_{ad\gamma}\right| = \frac{\left|d^d_{\mathrm{AC}}\right|\sqrt{4\pi\alpha}/e}{\hbar c\sqrt{2\rho_{\mathrm{LDM}}(\hbar c)^3/m_a c^2}} = \frac{\left|d^d_{\mathrm{AC}}\right|}{a_0}\,\frac{\sqrt{4\pi\alpha}}{e\hbar c}. \tag{9.2.1a}$$

By inserting $a_0 = \sqrt{2\rho_{\mathrm{LDM}}(\hbar c)^3}/m_a c^2 = 5.8\,\mathrm{MeV}$ and the bound on $\left|d^d_{\mathrm{AC}}\right|$, we obtain the bound on the ALP coupling to deuteron EDM operator as

$$\left|g_{ad\gamma}\right| < 1.7\times10^{-7}\,\mathrm{GeV}^{-2}. \tag{9.2.1}$$

Because a_0 is inversely proportional to m_a, the bounds obtained from the oscillating EDM measurements will linearly increase with the ALP mass m_a at comparable experimental sensitivity.

The upper limit on $\left|g_{ad\gamma}\right|$ obtained from our experiment in depicted in Fig. 9.3 in cyan (labelled as ’JEDI’). Also in the figure are the $\left|g_{aN\gamma}\right|$ bounds from nEDM[109], CASPERr-electric[110], and Beam EDM[111] experiments (the direct measurements), as well as the reformulated limits of electron-EDM HfF$^+$ experiment from [112, Fig. 3], as given in [108]. Additionally, the bound on $\left|g_{aN\gamma}\right|$ derived in Ref. [18] by assuming supernova SN1987A cooling $N + \gamma \rightarrow N + a$ is shown as a horizontal band (independent of m_a). It is worth noting that an alternative collapse mechanism for supernovae SN1987A is suggested in Ref. [113], which does not impose any limits on ALPs, that this exclusion region should be treated as model-dependent. Another exclusion region shown is from Ref. [114], based on the coupling of thermally-produced ALPs from combined data of CMB and baryon acoustic oscillations (BAO), which were derived for the mass range $1\times10^{-4}\,\mathrm{eV}/c^2 \lesssim m_a \lesssim 100\,\mathrm{eV}/c^2$, i.e., far away from the mass region probed in our experiment ($m_a \approx 0.5\,\mathrm{neV}/c^2$ for JEDI. However, the band is included following Ref. [108].

The directly measured upper bound from our experiment, 9.2.1 at $m_a = 0.5\,\mathrm{neV}/c^2$, falls within the model-dependent bounds obtained from SN1987A. However, it surpasses the limit obtained from CASPEr-electric experiment at $m_a \approx 100\,\mathrm{neV}/c^2$.

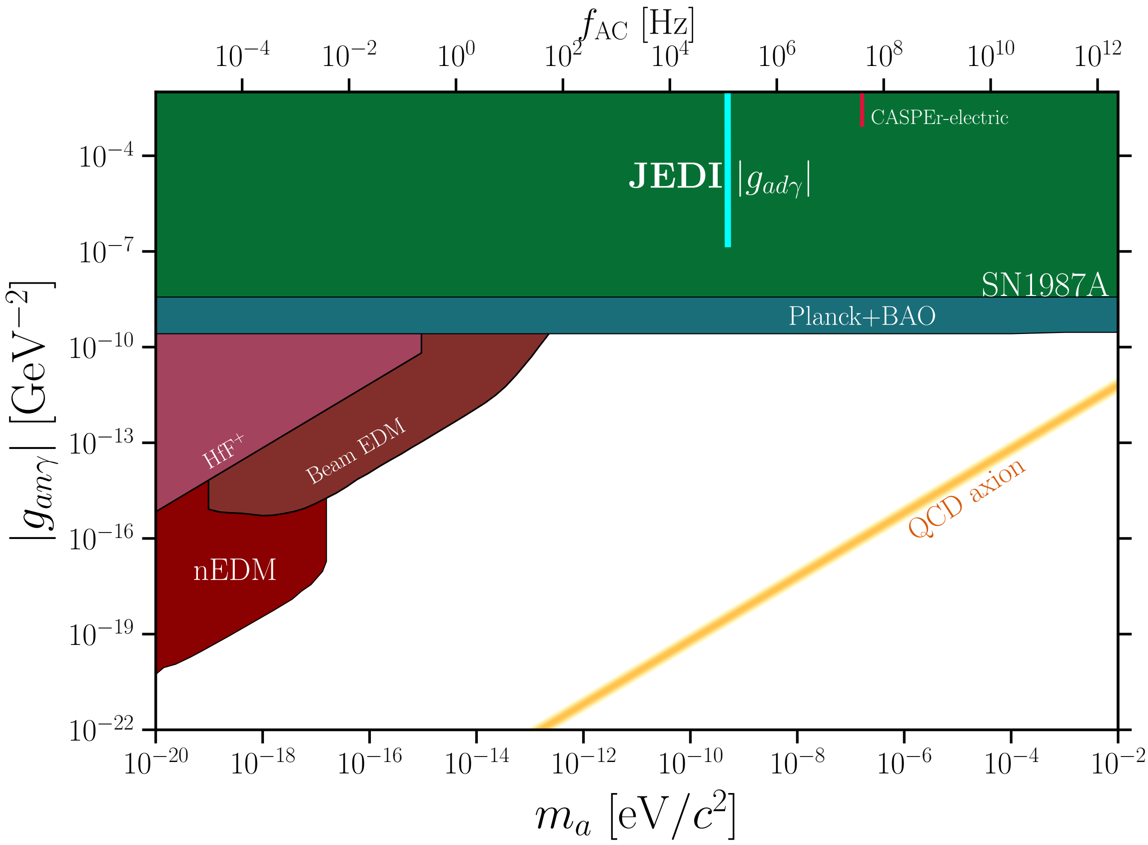

Figure 9.3: Plot depicting the 90% upper limit on $|g_{ad\gamma}|$ obtained from the current experiment (in cyan), along with the limits on $|g_{an\gamma}|$ from other experiments such as nEDM[109], CASPERr-electric[110], Beam EDM[111], and HfF$^+$[112] (as reported in Ref. [108]), in different shades of red. The green band shows the constraint from the SN1987A supernova cooling (derived in [18]), which could be model-dependent [113]. The blue band shows the limits obtained from the combination of Planck 2018 and BAO data [114] (as reported in Ref. [108]). Figure adapted from [108].

ALP coupling to gluons

The second coupling we considered is the ALP-gluon coupling C_G/f_a, explained in Section 2.2.2, which can be related to the ALP induced oscillating EDM of a nucleon as (see Eq. (2.2.4))

$$d^N_{\mathrm{AC}}(t) = S \cdot \kappa_a \frac{e\hbar c}{2mc^2} \frac{C_G}{f_a} a_0 \cos(\omega_a(t - t_0) + \phi_a(t_0))$$
$$\approx 2.4\times10^{-16}\, e\,\mathrm{cm}\, \frac{C_G}{f_a} a_0 \cos(\omega_a(t - t_0) + \phi_a(t_0)). \tag{9.2.2}$$

Here, S and m are the spin and mass of the nucleon, and κ_a is the chiral suppression factor of the θ_{Q}-term. It should be noted that the numerical factor is identical for the proton (neutron) and the deuteron because the ratio of spin to mass is approximately the same, given $S/m = (1/2)/m_p \approx 1/m_d$. However, when comparing the coupling constant of the deuteron to the direct determination of the C_G/f_a for a nucleon, corrections of order one are expected [83]. Therefore, the ALP-gluon coupling in the deuteron scenario is denoted with an additional superscript d as C^d_G. This is to indicate the expected difference of the coefficient C^d_G to the coupling C_G in the nucleon scenario.

Hence, the bound on the ALP gluon coupling constant in the case of deuteron can be written as

$$\left|\frac{C^d_G}{f_a}\right| = \left|\frac{d^d_{\mathrm{AC}}}{2.4\times10^{-16}\, e\,\mathrm{cm}} \times a_0\right| < 0.46\times10^{-4}\,\mathrm{GeV}^{-1}. \tag{9.2.3}$$

The upper limit of $\left|C^d_G/f_a\right|$ is presented in Fig. 9.4. This figure compares this limit with the values of $\left|C^d_G/f_a\right|$ obtained from various experiments such as the nEDM experiment [109], the Beam EDM [111], and HfF$^+$ electron EDM [112]. In addition, the figure also displays the limits obtained from astrophysical calculations such as Big Bang nucleosynthesis, solar core, and supernova SN1987A, where the latter is based on the supernova $N + \gamma \rightarrow N + a$ cooling mechanism. More information can be found in [1, 108]. The result from JEDI falls within the limits from supernova emissions.

Axion-wind effect

Finally, we will focus on the axion-wind scenario, i.e., the second term in Eq. (9.0.1). We assume a vanishing EDM-term and obtain an upper limit on the ALP pseudo-magnetic coupling to the deuteron spin $|C_d/f_a|$. This limit can be simplified in terms of the limit on the oscillating EDM using Eq. (9.0.1) on resonance and is given as

$$\left|\frac{C_d}{f_a}\right| = \left|\frac{2\gamma m_d c}{e\hbar\omega_a a_0}\right| \cdot \left|\vec{\Omega}_{\mathrm{rev}}\right| \cdot \left|d^d_{\mathrm{AC}}\right|. \tag{9.2.4a}$$

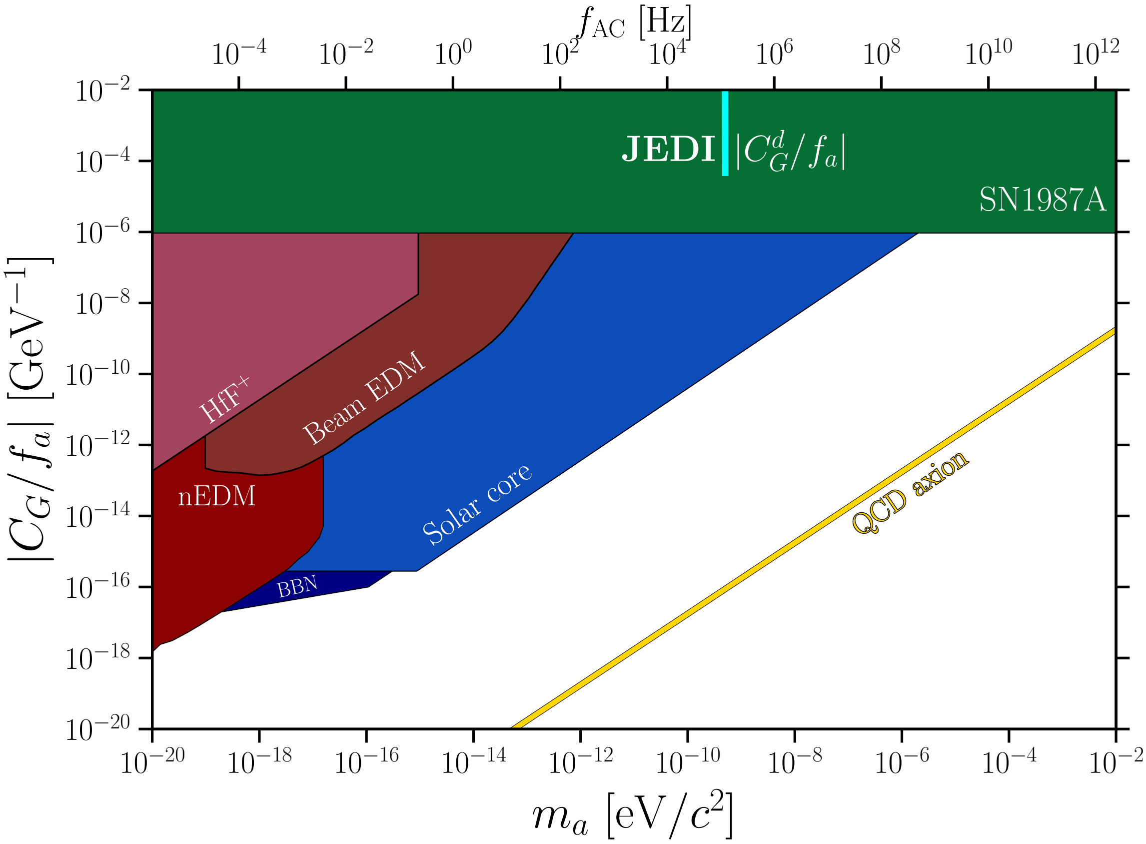

Figure 9.4: The plot depicts the 90% upper limit on the $\left|C_G^d/f_a\right|$ obtained from this experiment in cyan colour. This is compared with the bounds on $|C_G/f_a|$ (in various shades of red) from the nEDM [109], the Beam EDM [111], and HfF$^+$ electron EDM [112]. The limits obtained from astrophysical calculations such as supernova SN1987A [18], solar core [115, 116], and Big Bang nucleosynthesis [117] are also displayed in green, lighter blue, and darker blue, respectively. Figure adapted from [108].

After applying the ALP resonance condition $\omega_a = \gamma\left|G\vec{\Omega}_{\mathrm{rev}}\right|$ the equation above simplifies to

$$\left|\frac{C_d}{f_a}\right| = \left|\frac{2m_d c}{e\hbar G a_0}\right| \cdot \left|d^d_{\mathrm{AC}}\right|, \tag{9.2.4b}$$

where G is the magnetic anomaly of the deuteron. We get the bound as

$$\left|\frac{C_d}{f_a}\right| < 1.5\times10^{-5}\,\mathrm{GeV}^{-1}. \tag{9.2.4}$$

The resulting bound is linear dependence on the mass of the ALP m_a, indicating that the axion/ALP here is considered as dark matter candidates.

Figure 9.5 depicts the upper limit on the ALP-deuteron coupling $|C_d/f_a|$, along with the limits on the ALP-neutron coupling $|C_N/f_a|$ from other experiments and astrophysical calculations. The constraints on $|C_N/f_a|$ from supernova SN1987A, shown in green, are obtained with the assumption of bremsstrahlung as the underlying cooling mechanism, i.e., $NN \rightarrow NNa$. This was first calculated in [118], and modified in [119]. Our results fall within this limit, however, [113] mentions an alternate collapse mechanism which would not place limits on the emission of ALPs.

The axion wind effect is much more pronounced in storage ring experiments compared to other laboratory measurements because it is determined by the speed of the axions in relation to the particle being studied. For storage rings, the particles are relativistic $v \approx c$, but for particles at rest in the laboratory system (e.g., [109, 110]), the relative velocity is determined by the velocity of the Earth relative to the centre of our Galaxy, i.e., $v \approx 250\,\mathrm{km/s} \sim 10^{-3}\,c$. In relativistic storage rings, this contribution can be safely neglected. As a result, the pseudomagnetic field of the axion wind always points tangentially to the beam trajectory, and the direction of $\vec{v}$ is uniquely determined. On the other hand, in laboratory experiments, this determination is complicated.

It is worth noting that reference [109] used a value of $\rho_{\mathrm{LDM}} = 0.4\,\mathrm{GeV/cm^2}$, while the calculations in this thesis uses $\rho_{\mathrm{LDM}} = 0.55\,\mathrm{GeV/cm^2}$. Therefore, the coupling constants mentioned here are approximately 0.85 times smaller compared to the ones in [109].

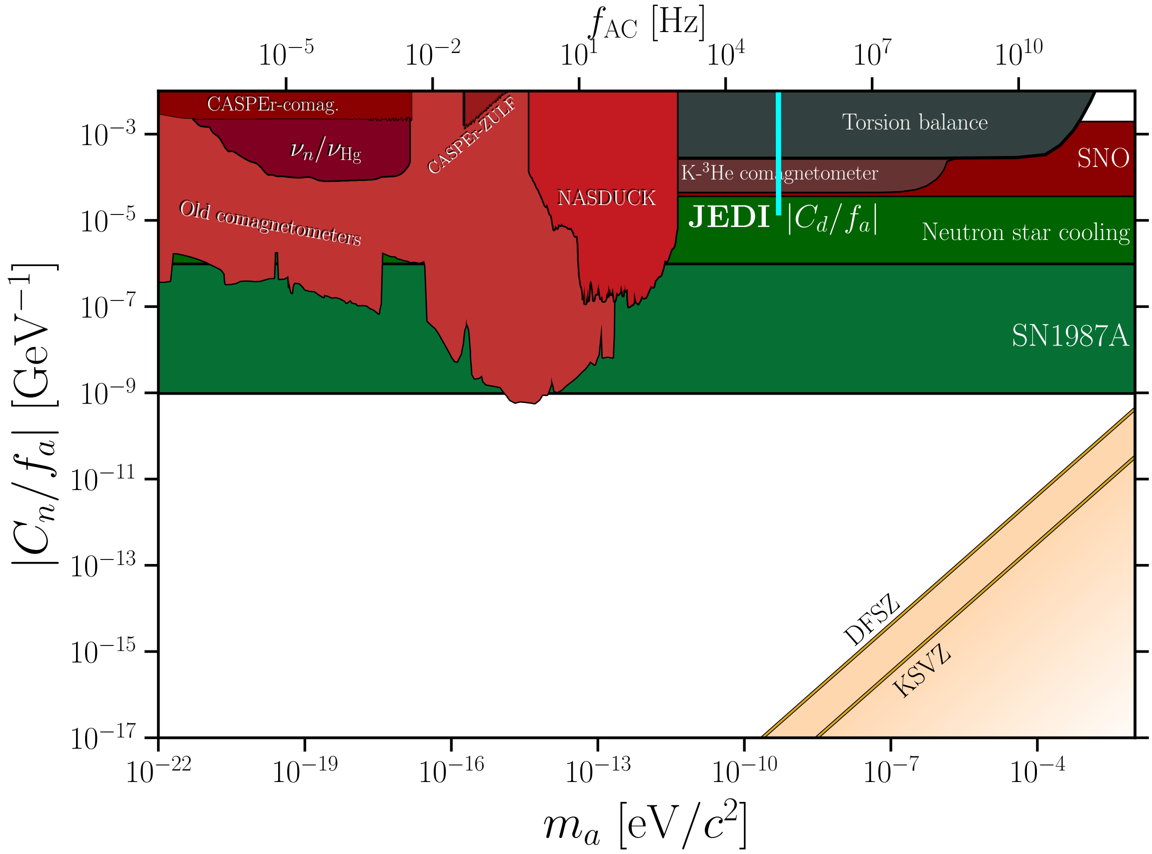

Figure 9.5: The figure shows the 90% upper limit on the ALP-deuteron coupling, $|C_d/f_a|$, obtained from the JEDI experiment in cyan. Also shown are the ALP-neutron coupling constant $|C_N/f_a|$ from several experiments: CASPEr-comag. [120], ν_n/ν_{Hg} [109], CASPEr-Zulf [121], Old comagnetometers [122], NASDUCK [123], Torsion balance [124], K^{3}He comagnetometer [125], SNO [126], Neutron star cooling [127], and SN1987A [119] (see also [34]). Figure adapted from [108].

10 Summary and outlook

The aim of this project was to demonstrate a novel method to detect ALPs using storage rings by utilising the IP polarised deuteron beam. ALPs can influence the spin of deuterons through inducing oscillating EDM, causing the spin to rotate about the radial axis, and through the axion-wind or pseudomagnetic effect, causing the spin rotation about the longitudinal axis. The method in this experiment, utilising relativistic particles, is particularly sensitive to the latter effect, which depends on the velocity of the particles with respect to the axion field.

The experiment took place in the Spring of 2019, with four days of effective data collection. A frequency range of 1.5 kHz, spanning from 119.997 kHz to 121.457 kHz, was scanned to find the resonance between the spin precession frequency of the deuteron f_{spin} and the axion-induced oscillation f_{osc}. Before the experiment, simulations were conducted to understand the experimental conditions, and post-experiment calibration was performed to obtain reliable results. The test for the resonance detection method was carried out using the RF Wien filter, which also served as a calibration tool for axion scans.

Although no ALP signals were detected within the experimental sensitivity, the significant achievement of this project was establishing the first-ever upper limit of the oscillating EDM of deuterons. By assuming only EDM coupling, the oscillating EDM value of the deuteron at the 90% confidence level above approximately $10^{-22}\,e\,\text{cm}$ was excluded. Additionally, constraints on different ALP couplings were derived in the mass range $m_a = 4.95\,\text{neV}\,c^{-2} \;-\; 5.02\,\text{neV}\,c^{-2}$. Comparisons of ALP coupling to the EDM operator of the deuteron $g_{ad\gamma}$, ALP to the gluons of the deuteron C_G^d/f_a, and

ALP to deuteron spin (pseudo-magnetic) C_d/f_a with the existing experimental results are also provided.

One of the notable advantages of this method is the mitigation of systematic effects due to the cancellation of first-order systematics through the use of four beam bunches. To enhance the sensitivity in future experiments, it is recommended to focus on extended beam times, higher beam intensities, and higher beam polarisation. Moreover, this experimental method allows the use of various hadrons (protons, deuterons, and heavier nuclei), enabling the exploration of the effect of spin and isospin on different couplings. Furthermore, conducting experiments at different values of magnetic anamoly G would expand the frequency range and further improve the search capabilities.

Storage ring searches for axions can be pursued at facilities with accessible polarised hadrons beams like RHIC, NICA or GSI/FAIR. Future storage rings, like the hybrid ring proposed for the search of permanent EDM of charged hadrons, featuring radial electric and vertical magnetic field [128], offers further avenues. Especially, the combination of the fields would enable the search for axions to be performed in the entire mass range depicted in Figs. 9.3 to 9.5 [129].

In summary, this project, which is the focus of my thesis, successfully demonstrated the feasibility of ALP searches using storage rings. The experiment provided constraints on various ALP couplings and established the first limit on oscillating EDM of deuterons. These results contribute to the ongoing efforts in the search for QCD axion and ALP, and towards expanding our understanding of physics beyond the SM.

A Appendix A

The run numbers for axion scans along with the frequency range of the scan for the axion scans are given in Table A.1. Runs shaded in gray have a momentum scan rate of 0.112 MeV/c and the rest were scanned at a rate of 0.138 MeV/c.

Table A.1: List of runs from axion scan in increasing order of frequency

frequency range [Hz]	run number
119997.06 - 120010.67	51078
120011.14 - 120024.72	51077
120025.49 - 120038.91	51076
120039.54 - 120053.09	51075
120053.61 - 120067.17	51074
120067.78 - 120081.40	51073
120082.06 - 120095.66	51072
120096.30 - 120109.96	51071
120110.41 - 120124.02	51070
120124.65 - 120138.24	51069
120138.87 - 120152.49	51068
120152.95 - 120166.56	51067
120167.18 - 120180.75	51066
120181.20 - 120194.81	51065
120195.44 - 120208.96	51064

Continued on the next page

Table A.1 – Continued from the previous page

frequency range [Hz]	run number
120209.58 - 120223.15	51063
120223.77 - 120237.36	51062
120237.85 - 120251.52	51061
120251.99 - 120268.84	51050
120266.14 - 120282.96	51129
120280.22 - 120297.08	51128
120294.45 - 120311.10	51127
120308.64 - 120325.36	51126
120322.08 - 120338.98	51125
	51133
120336.23 - 120353.04	51124
	51132
120350.31 - 120367.17	51123
	51131
120365.27 - 120382.15	51122
120379.40 - 120396.24	51121
120393.49 - 120410.37	51120
120407.89 - 120424.62	51119
120421.94 - 120438.79	51091
120436.01 - 120452.84	51090
120450.34 - 120467.19	51049
120464.59 - 120481.33	51048
120478.70 - 120495.41	51042
120492.83 - 120509.60	51041
120507.07 - 120523.81	51040
120521.17 - 120538.00	51039
120535.25 - 120552.18	51034
120549.66 - 120566.41	51033

Continued on the next page

Table A.1 – Continued from the previous page

frequency range [Hz]	run number
120563.80 - 120580.48	51032
120577.84 - 120594.59	51029
120592.13 - 120609.00	51028
120606.23 - 120623.09	51026
120620.28 - 120637.03	51024
120634.38 - 120651.32	51022
120648.68 - 120665.55	51021
120662.97 - 120679.74	51020
120677.07 - 120693.85	51019
120691.36 - 120708.05	51018
120705.40 - 120722.15	51017
120719.49 - 120736.40	51016
120733.74 - 120750.69	51015
120747.94 - 120764.70	51014
120762.04 - 120779.00	51013
120776.01 - 120792.77	51138 51012
120790.12 - 120807.07	51137 51011
120804.42 - 120821.21	51136 51009
120818.61 - 120835.31	51135 51008
120832.99 - 120849.67	51134 51007
120847.18 - 120863.89	50953
120861.34 - 120878.18	50955

Continued on the next page

Table A.1 – Continued from the previous page

frequency range [Hz]	run number
120875.78 - 120892.44	50957
120889.85 - 120906.76	50959
120904.16 - 120920.82	50960
120918.36 - 120935.14	50961
120932.60 - 120949.27	50962
120946.67 - 120963.51	50965
120960.91 - 120977.49	50966
120975.04 - 120991.73	50967
120989.09 - 121005.91	50968
121003.14 - 121019.84	50973
121017.34 - 121034.02	50974
121031.54 - 121048.26	50975
121045.67 - 121062.35	50976
121059.84 - 121076.73	50977
121074.06 - 121090.75	50978
121088.09 - 121104.78	50979
121102.31 - 121118.92	50980
121116.59 - 121133.29	50981
121130.49 - 121147.20	50982
121144.72 - 121161.57	50983
121158.89 - 121175.72	50984
121173.04 - 121189.96	50985
121187.30 - 121204.00	50986
121201.50 - 121218.24	50987
121215.54 - 121232.46	50988
121229.77 - 121246.39	50991
121243.91 - 121260.54	50992
121258.04 - 121274.88	50993
121272.24 - 121289.12	50994

Continued on the next page

Table A.1 – Continued from the previous page

frequency range [Hz]	run number
121286.27 - 121303.19	50995
121300.64 - 121317.41	50996
121314.79 - 121331.56	50997
121328.91 - 121345.62	50998
121343.26 - 121359.98	50999
121357.28 - 121374.02	51000
121371.36 - 121388.16	51001
121385.53 - 121402.17	51002
121399.78 - 121416.53	51003
121413.82 - 121430.74	51004
121428.03 - 121444.78	51005
121442.23 - 121459.10	51006

The RF Wien filter have 12 runs in total given in Table ??. Scans were done with the scan rates $\pm\ 0.112\,\mathrm{MeV}/c$ and $\pm\ 0.056\,\mathrm{MeV}/c$.

Table A.2: Details of RF Wien filter scans.

frequency range [Hz]	scan rate [MeV/c]	run number
120840.27 - 120853.91	0.112	51101
120840.28 - 120853.91		51102
120840.28 - 120853.90		51103
120843.73 - 120850.44	0.056	51104
120843.76 - 120850.45		51105
120843.83 - 120849.96		51106
120853.87 - 120840.21	-0.112	51107
120853.89 - 120840.24		51108
120853.88 - 120840.22		51109
120850.62 - 120843.63	-0.056	51110
120850.67 - 120843.90		51111
120850.69 - 120843.31		51112

Bibliography

[1] R. L. Workman et al., ‘Review of particle physics’, Progress of Theoretical and Experimental Physics 2022, 10.1093/ptep/ptac097 (2022) (cit. on pp. 1, 6–12, 100, 103, 105).

[2] R. D. Peccei and H. R. Quinn, ‘CP Conservation in the presence of pseudoparticles’, Physical Review Letters 38, 1440–1443 (1977) (cit. on pp. 1, 7).

[3] R. D. Peccei and H. R. Quinn, ‘Constraints imposed by cp conservation in the presence of pseudoparticles’, Physical Review D 16, 1791–1797 (1977) (cit. on pp. 1, 7).

[4] S. Weinberg, ‘A new light boson?’, Phys. Rev. Lett. 40, 223–226 (1978) (cit. on pp. 1, 7, 11).

[5] F. Wilczek, ‘Problem of strong P and T invariance in the presence of instantons’, Physical Review Letters 40, 279–282 (1978) (cit. on pp. 1, 7).

[6] P. Sikivie, ‘Invisible axion search methods’, Reviews of Modern Physics 93, 015004 (2021) (cit. on pp. 1, 8).

[7] S. P. Chang et al., ‘Axionlike dark matter search using the storage ring EDM method’, Phys. Rev. D 99, 083002 (2019) (cit. on p. 2).

[8] A. D. Sakharov, ‘Violation of CP in variance, c asymmetry, and baryon asymmetry of the universe’, Soviet Physics Uspekhi 34, 392–393 (1991) (cit. on p. 6).

[9] C. A. Baker et al., ‘Improved experimental limit on the electric dipole moment of the neutron’, Physical Review Letters 97, 131801 (2006) (cit. on p. 7).

[10] C. Abel et al., ‘Measurement of the permanent electric dipole moment of the neutron’, Phys. Rev. Lett. 124, 081803 (2020) (cit. on p. 7).

[11] A. Bosma, ‘The distribution and kinematics of neutral hydrogen in spiral galaxies of various morphological types’, PhD thesis (Groningen University, 1978) (cit. on p. 8).

[12] E. Corbelli and P. Salucci, ‘The extended rotation curve and the dark matter halo of m33’, Monthly Notices of the Royal Astronomical Society 311, 441–447 (2000) (cit. on p. 8).

[13] V. Trimble, ‘Existence and nature of dark matter in the universe’, Annual Review of Astronomy and Astrophysics 25, 425–472 (1987) (cit. on p. 8).

[14] L. Abbott and P. Sikivie, ‘A cosmological bound on the invisible axion’, Physics Letters B 120, 133–136 (1983) (cit. on p. 8).

[15] J. Preskill, M. B. Wise, and F. Wilczek, ‘Cosmology of the invisible axion’, Physics Letters B 120, 127–132 (1983) (cit. on p. 8).

[16] M. Dine and W. Fischler, ‘The not-so-harmless axion’, Physics Letters B 120, 137–141 (1983) (cit. on p. 8).

[17] P. W. Graham and S. Rajendran, ‘Axion dark matter detection with cold molecules’, Phys. Rev. D 84, 055013 (2011) (cit. on pp. 9–10).

[18] P. W. Graham and S. Rajendran, ‘New observables for direct detection of axion dark matter’, Phys. Rev. D 88, 035023 (2013) (cit. on pp. 9, 11, 100, 103–104, 106).

[19] D. Budker et al., ‘Proposal for a cosmic axion spin precession experiment (casper)’, Phys. Rev. X 4, 021030 (2014) (cit. on pp. 9, 18).

[20] R. D. Peccei, ‘The Strong CP problem and axions’, Lect. Notes Phys. 741, edited by M. Kuster, G. Raffelt, and B. Beltran, 3–17 (2008) (cit. on p. 9).

[21] I. G. Irastorza, ‘An introduction to axions and their detection’, SciPost Phys. Lect. Notes, 45 (2022) (cit. on pp. 10, 12).

[22] M. Pospelov and A. Ritz, ‘Theta induced electric dipole moment of the neutron via QCD sum rules’, Phys. Rev. Lett. 83, 2526–2529 (1999) (cit. on pp. 10–11).

[23] N. N. Nikolaev, ‘Spin of protons in NICA and PTR storage rings as an axion antenna’, Pisma Zh. Eksp. Teor. Fiz. 115, 683–684 (2022) (cit. on pp. 11, 27, 99–100).

[24] I. G. Irastorza and J. Redondo, ‘New experimental approaches in the search for axion-like particles’, Progress in Particle and Nuclear Physics 102, 89–159 (2018) (cit. on pp. 12, 16).

[25] Y. Fukuda et al., ‘Production and detection of axions by using optical resonators’, Progress in Crystal Growth and Characterization of Materials 33, 363–366 (1996) (cit. on p. 12).

[26] G. Mueller et al., ‘Detailed design of a resonantly enhanced axion-photon regeneration experiment’, Physical Review D 80, 072004 (2009) (cit. on pp. 12–13).

[27] F. Hoogeveen and T. Ziegenhagen, ‘Production and detection of light bosons using optical resonators’, Nuclear Physics B 358, 3–26 (1991) (cit. on p. 13).

[28] K. Ehret et al., ‘New ALPS results on hidden-sector lightweights’, Physics Letters B 689, 149–155 (2010) (cit. on p. 13).

[29] M. Betz et al., ‘First results of the CERN resonant weakly interacting sub-eV particle search (CROWS)’, Physical Review D 88, 075014 (2013) (cit. on p. 13).

[30] R. Ballou et al., ‘New exclusion limits on scalar and pseudoscalar axionlike particles from light shining through a wall’, Physical Review D 92, 092002 (2015) (cit. on p. 13).

[31] R. Bähre et al., ‘Any light particle search II — technical design report’, Journal of Instrumentation 8, T09001–T09001 (2013) (cit. on p. 13).

[32] L. Capparelli et al., ‘Axion-like particle searches with sub-THz photons’, Physics of the Dark Universe 12, 37–44 (2016) (cit. on p. 13).

[33] L. Maiani, R. Petronzio, and E. Zavattini, ‘Effects of nearly massless, spin-zero particles on light propagation in a magnetic field’, Physics Letters B 175, 359–363 (1986) (cit. on p. 13).

[34] G. Raffelt and L. Stodolsky, ‘Mixing of the photon with low-mass particles’, Phys. Rev. D 37, 1237–1249 (1988) (cit. on pp. 13, 108).

[35] F. D. Valle et al., ‘The PVLAS experiment: measuring vacuum magnetic birefringence and dichroism with a birefringent fabry–perot cavity’, The European Physical Journal C 76, 10.1140/epjc/s10052-015-3869-8 (2016) (cit. on p. 13).

[36] M. T. Hartman et al., ‘Noise characterization for resonantly enhanced polarimetric vacuum magnetic-birefringence experiments’, Review of Scientific Instruments 88, 123114 (2017) (cit. on p. 13).

[37] A. Arvanitaki and A. A. Geraci, ‘Resonantly detecting axion-mediated forces with nuclear magnetic resonance’, Physical Review Letters 113, 161801 (2014) (cit. on p. 13).

[38] H. Fosbinder-Elkins et al., A method for controlling the magnetic field near a superconducting boundary in the ariadne axion experiment, 2017 (cit. on p. 13).

[39] P. Sikivie, ‘Experimental Tests of the Invisible Axion’, Phys. Rev. Lett. 51, edited by M. A. Srednicki, [Erratum: Phys.Rev.Lett. 52, 695 (1984)], 1415–1417 (1983) (cit. on pp. 14–15).

[40] K. van Bibber et al., ‘Design for a practical laboratory detector for solar axions’, Physical Review D 39, 2089–2099 (1989) (cit. on p. 14).

[41] K. Zioutas et al., ‘First results from the CERN axion solar telescope’, Physical Review Letters 94, 121301 (2005) (cit. on p. 14).

[42] E. Armengaud et al., ‘Conceptual design of the international axion observatory (IAXO)’, Journal of Instrumentation 9, T05002–T05002 (2014) (cit. on p. 14).

[43] W. Liao, ‘Generation and search of axion-like light particle using intense crystalline field’, Physics Letters B 702, 55–58 (2011) (cit. on p. 14).

[44] T. Yamaji et al., ‘Theoretical calculation of coherent laue-case conversion between x-rays and ALPs for an x-ray light-shining-through-a-wall experiment’, Physical Review D 96, 115001 (2017) (cit. on p. 14).

[45] E. Paschos and K. Zioutas, ‘A proposal for solar axion detection via bragg scattering’, Physics Letters B 323, 367–372 (1994) (cit. on p. 14).

[46] R. Creswick et al., ‘Theory for the direct detection of solar axions by coherent primakoff conversion in germanium detectors’, Physics Letters B 427, 235–240 (1998) (cit. on p. 14).

[47] F. T. Avignone et al., ‘Experimental search for solar axions via coherent primakoff conversion in a germanium spectrometer’, Physical Review Letters 81, 5068–5071 (1998) (cit. on p. 14).

[48] A. Morales, ‘Particle dark matter and solar axion searches with a small germanium detector at the canfranc underground laboratory’, Astroparticle Physics 16, 325–332 (2002) (cit. on p. 14).

[49] K. Abe et al., ‘Search for solar axions in XMASS, a large liquid-xenon detector’, Physics Letters B 724, [Erratum: Phys. Rev.D95,no.2,029904(2017)]., 46–50 (2013) (cit. on p. 15).

[50] C. Fu et al., ‘Limits on axion couplings from the first 80 days of data of the PandaX-II experiment’, Physical Review Letters 119, 181806 (2017) (cit. on p. 15).

[51] D. Akerib et al., ‘First searches for axions and axionlike particles with the LUX experiment’, Physical Review Letters 118, 261301 (2017) (cit. on p. 15).

[52] S. J. Asztalos et al., ‘Improved rf cavity search for halo axions’, Physical Review D 69, 011101 (2004) (cit. on p. 16).

[53] J. E. Kim, ‘Weak-interaction singlet and strong CP invariance’, Phys. Rev. Lett. 43, 103–107 (1979) (cit. on p. 16).

[54] M. Shifman, A. Vainshtein, and V. Zakharov, ‘Can confinement ensure natural CP invariance of strong interactions?’, Nuclear Physics B 166, 493–506 (1980) (cit. on p. 16).

[55] M. Dine, W. Fischler, and M. Srednicki, ‘A simple solution to the strong CP problem with a harmless axion’, Physics Letters B 104, 199–202 (1981) (cit. on p. 16).

[56] A. P. Zhitnitskii, ‘Possible suppression of axion-hadron interactions’, Sov. J. Nucl. Phys. (Engl. Transl.); (United States) (1980) (cit. on p. 16).

[57] B. M. Brubaker et al., ‘First results from a microwave cavity axion search at $24\ \mu\mathrm{eV}$’, Phys. Rev. Lett. 118, 061302 (2017) (cit. on p. 16).

[58] K. M. Backes et al., ‘A quantum enhanced search for dark matter axions’, Nature 590, 238–242 (2021) (cit. on p. 16).

[59] B. T. McAllister et al., ‘The ORGAN experiment: an axion haloscope above 15 GHz’, Physics of the Dark Universe 18, 67–72 (2017) (cit. on p. 16).

[60] D. Alesini et al., ‘Search for invisible axion dark matter of mass $\mathrm{m}_a = 43\ \mu\mathrm{eV}$ with the quax–$a\gamma$ experiment’, Phys. Rev. D 103, 102004 (2021) (cit. on p. 16).

[61] D. Horns et al., ‘Searching for WISPy cold dark matter with a dish antenna’, Journal of Cosmology and Astroparticle Physics 2013, 016–016 (2013) (cit. on p. 17).

[62] A. Caldwell et al. (MADMAX Working Group), ‘Dielectric haloscopes: a new way to detect axion dark matter’, Phys. Rev. Lett. 118, 091801 (2017) (cit. on p. 17).

[63] P. Sikivie, N. Sullivan, and D. B. Tanner, ‘Proposal for axion dark matter detection using an LC circuit’, Phys. Rev. Lett. 112, 131301 (2014) (cit. on p. 17).

[64] J. L. Ouellet et al., ‘First results from abracadabra-10 cm: a search for sub-μeV axion dark matter’, Phys. Rev. Lett. 122, 121802 (2019) (cit. on p. 17).

[65] A. V. Gramolin et al., ‘Search for axion-like dark matter with ferromagnets’, Nature Physics 17, 79–84 (2020) (cit. on p. 17).

[66] N. Crisosto et al., ‘ADMX SLIC: results from a superconducting LC circuit investigating cold axions’, Physical Review Letters 124, 241101 (2020) (cit. on p. 17).

[67] J. A. Devlin et al., ‘Constraints on the coupling between axionlike dark matter and photons using an antiproton superconducting tuned detection circuit in a cryogenic penning trap’, Physical Review Letters 126, 041301 (2021) (cit. on p. 17).

[68] M. Lawson et al., ‘Tunable axion plasma haloscopes’, Phys. Rev. Lett. 123, 141802 (2019) (cit. on p. 17).

[69] G. Rybka et al., ‘Search for dark matter axions with the orpheus experiment’, Physical Review D 91, 011701 (2015) (cit. on p. 17).

[70] H. H. Barschall and W. Haeberli, eds., The madison convention, polarization phenomena in nuclear reactions, https://www.osti.gov/biblio/4726823 (University of Wisconsin Press, Madison, WI, 1971) (cit. on p. 22).

[71] K. S. Krane, ‘The force between nucleons’, in Introductory nuclear physics (Wiley, 1987) Chap. 2, p. 845 (cit. on pp. 22, 24).

[72] G. G. Ohlsen and P. Keaton, ‘Techniques for measurement of and spin-1 polarization analyzing tensors’, Nuclear Instruments and Methods 109, 41–59 (1973) (cit. on p. 23).

[73] V. Bargmann, L. Michel, and V. L. Telegdi, ‘Precession of the polarization of particles moving in a homogeneous electromagnetic field’, Phys. Rev. Lett. 2, 435–436 (1959) (cit. on p. 26).

[74] T. Fukuyama and A. J. Silenko, ‘Derivation of Generalized Thomas-Bargmann-Michel-Telegdi Equation for a Particle with Electric Dipole Moment’, Int. J. Mod. Phys. A28, 1350147 (2013) (cit. on p. 26).

[75] B. W. Montague, ‘Polarized beams in high energy storage rings’, Physics Reports 113, 1–96 (1984) (cit. on p. 27).

[76] A. J. Silenko, Relativistic spin dynamics conditioned by dark matter axions, 2022 (cit. on pp. 27, 99–100).

[77] G. Guidoboni, ‘Spin Coherence Time studies for the storage ring EDM search’, PhD thesis (Ferrara U., 2013) (cit. on p. 34).

[78] J. Pretz and on behalf of the JEDI collaboration, ‘Measurement of permanent electric dipole moments of charged hadrons in storage rings’, Hyperfine Interactions 214, 111–117 (2013) (cit. on p. 35).

[79] D. A. Edwards and M. J. Syphers, ‘Acceleration and phase stability’, in An introduction to the physics of high energy accelerators (John Wiley Sons, Ltd, 1993) Chap. 2, pp. 18–56 (cit. on p. 35).

[80] K. Wille, The physics of particle accelerators, An introduction (Oxford University Press, USA, 2001), p. 328 (cit. on p. 35).

[81] G. Guidoboni et al. (JEDI Collaboration), ‘How to reach a thousand-second in-plane polarization lifetime with $0.97-\mathrm{GeV}/c$ deuterons in a storage ring’, Phys. Rev. Lett. 117, 054801 (2016) (cit. on p. 36).

[82] G. Guidoboni et al. (JEDI Collaboration), ‘Connection between zero chromaticity and long in-plane polarization lifetime in a magnetic storage ring’, Phys. Rev. Accel. Beams 21, 024201 (2018) (cit. on pp. 36, 50).

[83] S. Karanth et al., ‘First search for axion-like particles in a storage ring using a polarized deuteron beam’, inpress (2022) (cit. on pp. 36, 99, 105).

[84] G. I. Budker, ‘An effective method of damping particle oscillations in proton and antiproton storage rings’, Soviet Atomic Energy 22, 438–440 (1967) (cit. on p. 36).

[85] S. Karanth et al., ‘Influence of electron cooling on the polarization lifetime of a horizontally polarized storage ring beam’, Nuclear Instruments and Methods in Physics Research Section A: Accelerators, Spectrometers, Detectors and Associated Equipment 987, 164797 (2021) (cit. on pp. 36–37, 79).

[86] Jedi collaboration, https://collaborations.fz-juelich.de/ikp/jedi/internal/internal.shtml (cit. on p. 39).

[87] R. Maier, ‘Cooler synchrotron COSY: Performance and perspectives’, Nucl. Instrum. Meth. A 390, 1–8 (1997) (cit. on p. 39).

[88] R. Weidmann et al., ‘The polarized ion source for COSY’, Review of Scientific Instruments 67, 1357–1358 (1996) (cit. on p. 40).

[89] D. Chiladze et al., ‘Determination of deuteron beam polarizations at cosy’, Phys. Rev. ST Accel. Beams 9, 050101 (2006) (cit. on p. 40).

[90] V. S. Morozov et al., ‘Experimental verification of predicted beam-polarization oscillations near a spin resonance’, Physical Review Letters 100, 054801 (2008) (cit. on p. 41).

[91] P. Benati et al., ‘Synchrotron oscillation effects on an rf-solenoid spin resonance’, Phys. Rev. ST Accel. Beams 15, 124202 (2012) (cit. on pp. 42, 63).

[92] J. Slim et al., ‘Electromagnetic simulation and design of a novel waveguide rf wien filter for electric dipole moment measurements of protons and deuterons’, Nucl. Instrum. Meth. A 828, 116–124 (2016) (cit. on pp. 42–43).

[93] F. Müller et al., ‘Measurement of deuteron carbon vector analyzing powers in the kinetic energy range 170–380 mev’, Eur. Phys. J. A 56, 1–8 (2020) (cit. on p. 44).

[94] S. Karanth et al., ‘Influence of electron cooling on the polarization lifetime of a horizontally polarized storage ring beam’, Nuclear Instruments and Methods in Physics Research Section A: Accelerators, Spectrometers, Detectors and Associated Equipment 987, 164797 (2021) (cit. on p. 47).

[95] E. Stephenson (JEDI), ‘A Search for Axion-like Particles with a Horizontally Polarized Beam In a Storage Ring’, PoS PSTP2019, edited by J. Pierce et al., 018 (2020) (cit. on p. 47).

[96] M. Froissart and R. Stora, ‘Depolarisation d’un faisceau de protons polarises dans un synchrotron’, Nuclear Instruments and Methods 7, 297–305 (1960) (cit. on p. 49).

[97] P. Benati et al., ‘Erratum: Synchrotron oscillation effects on an rf-solenoid spin resonance [Phys. Rev. ST Accel. Beams 15, 124202 (2012)]’, Phys. Rev. ST Accel. Beams 16, 049901 (2013) (cit. on p. 63).

[98] R. Brun and F. Rademakers, ROOT — an object oriented data analysis framework, Apr. 1997 (cit. on p. 79).

[99] JEDI Collaboration, Dataset from the ALP search by JEDI Collaboration, experiment April 2019, version v1.0, (DOI not yet publically accessible, private url: https://data.fz-juelich.de/privateurl.xhtml?token=b84e3bd8-2bdc-4b68-9a3a-ceed6c03fe04 - do not publish.), June 2022 (cit. on p. 79).

[100] G. J. Feldman and R. D. Cousins, ‘Unified approach to the classical statistical analysis of small signals’, Phys. Rev. D 57, 3873–3889 (1998) (cit. on pp. 79, 89, 91, 95).

[101] Z. Bagdasarian et al., ‘Measuring the polarization of a rapidly precessing deuteron beam’, Phys. Rev. ST Accel. Beams 17, 052803 (2014) (cit. on p. 79).

[102] D. Eversmann et al. (JEDI collaboration), ‘New method for a continuous determination of the spin tune in storage rings and implications for precision experiments’, Phys. Rev. Lett. 115, 094801 (2015) (cit. on p. 79).

[103] D. Eversmann, J. Pretz, and M. Rosenthal, ‘Amplitude estimation of a sine function based on confidence intervals and bayes’ theorem’, Journal of Instrumentation 11, P05003–P05003 (2016) (cit. on pp. 89–90).

[104] S. Plaszczynski et al., ‘A novel estimator of the polarization amplitude from normally distributed Stokes parameters’, Monthly Notices of the Royal Astronomical Society 439, 4048–4056 (2014) (cit. on p. 89).

[105] S. Rice, ‘Mathematical analysis of random noise’, Bell System Technical Journal 24, 46–156 (1945) (cit. on p. 90).

[106] T. M. Karbach, ‘Feldman-cousins confidence levels - toy mc method’, (2011) (cit. on p. 93).

[107] P. V. Vorob'ev, I. V. Kolokolov, and V. F. Fogel, ‘Ferromagnetic detector of (pseudo)Goldstone bosons’, JETP Lett. 50, 65–67 (1989) (cit. on p. 100).

[108] C. O'Hare, Cajohare/axionlimits: axionlimits, https://cajohare.github.io/AxionLimits/, version v1.0, July 2020 (cit. on pp. 103–106, 108).

[109] C. Abel et al., ‘Search for axionlike dark matter through nuclear spin precession in electric and magnetic fields’, Physical Review X 7, 041034 (2017) (cit. on pp. 103–108).

[110] D. Aybas et al., ‘Search for axionlike dark matter using solid-state nuclear magnetic resonance’, Phys. Rev. Lett. 126, 141802 (2021) (cit. on pp. 103–104, 107).

[111] I. Schulthess et al., ‘New limit on axionlike dark matter using cold neutrons’, Physical Review Letters 129, 191801 (2022) (cit. on pp. 103–106).

[112] T. S. Roussy et al., ‘Experimental constraint on axionlike particles over seven orders of magnitude in mass’, Physical Review Letters 126, 171301 (2021) (cit. on pp. 103–106).

[113] N. Bar, K. Blum, and G. D'Amico, ‘Is there a supernova bound on axions?’, Physical Review D 101, 123025 (2020) (cit. on pp. 103–104, 107).

[114] L. Caloni et al., ‘Novel cosmological bounds on thermally-produced axion-like particles’, Journal of Cosmology and Astroparticle Physics 2022, 021 (2022) (cit. on pp. 103–104).

[115] A. Hook and J. Huang, ‘Probing axions with neutron star inspirals and other stellar processes’, Journal of High Energy Physics 2018, 10.1007/jhep06(2018)036 (2018) (cit. on p. 106).

[116] L. D. Luzio et al., ‘An even lighter QCD axion’, Journal of High Energy Physics 2021, 10.1007/jhep05(2021)184 (2021) (cit. on p. 106).

[117] K. Blum et al., ‘Constraining axion dark matter with big bang nucleosynthesis’, Physics Letters B 737, 30–33 (2014) (cit. on p. 106).

[118] G. G. Raffelt, ‘Astrophysical axion bounds’, in Lecture notes in physics (Springer Berlin Heidelberg, 2008), pp. 51–71 (cit. on p. 107).

[119] P. Carenza et al., ‘Improved axion emissivity from a supernova via nucleon-nucleon bremsstrahlung’, Journal of Cosmology and Astroparticle Physics 2019, 016–016 (2019) (cit. on pp. 107–108).

[120] D. F. J. Kimball et al., ‘Overview of the cosmic axion spin precession experiment (CASPEr)’, in Microwave cavities and detectors for axion research (Springer International Publishing, 2020), pp. 105–121 (cit. on p. 108).

[121] A. Garcon et al., ‘Constraints on bosonic dark matter from ultralow-field nuclear magnetic resonance’, Science Advances 5, 10.1126/sciadv.aax4539 (2019) (cit. on p. 108).

[122] I. M. Bloch et al., ‘Axion-like relics: new constraints from old comagnetometer data’, Journal of High Energy Physics 2020, 10.1007/jhep01(2020)167 (2020) (cit. on p. 108).

[123] I. M. Bloch et al., ‘New constraints on axion-like dark matter using a floquet quantum detector’, Science Advances 8, 10.1126/sciadv.abl8919 (2022) (cit. on p. 108).

[124] E. G. Adelberger et al., ‘Particle-physics implications of a recent test of the gravitational inverse-square law’, Physical Review Letters 98, 131104 (2007) (cit. on p. 108).

[125] G. Vasilakis et al., ‘Limits on new long range nuclear spin-dependent forces set with a k-he3 comagnetometer’, Physical Review Letters 103, 261801 (2009) (cit. on p. 108).

[126] A. Bhusal, N. Houston, and T. Li, ‘Searching for solar axions using data from the sudbury neutrino observatory’, Physical Review Letters 126, 091601 (2021) (cit. on p. 108).

[127] M. Buschmann et al., ‘Upper limit on the QCD axion mass from isolated neutron star cooling’, Physical Review Letters 128, 091102 (2022) (cit. on p. 108).

[128] F. Abusaif et al., Storage ring to search for electric dipole moments of charged particles : feasibility study, CERN Yellow Reports. Monographs (CERN, Geneva, 2021), IX, [2], 246 (cit. on p. 110).

[129] J. Pretz et al., ‘Statistical sensitivity estimates for oscillating electric dipole moment measurements in storage rings’, The European Physical Journal C 80, 10.1140/epjc/s10052-020-7664-9 (2020) (cit. on p. 110).